Imperial College London

# Brillouin Scattering Microscopy for Mechanical Imaging

Giuseppe Antonacci

Imperial College London
Department of Physics

*Thesis submitted in partial fulfilment of the requirements*
*for the degree of Doctor of Philosophy*
*and the Diploma of Imperial College*

April 14, 2015

**The copyright of this thesis rests with the author and is made available under a Creative Commons Attribution Non-Commercial No Derivatives licence. Researchers are free to copy, distribute or transmit the thesis on the condition that they attribute it, that they do not use it for commercial purposes and that they do not alter, transform or build upon it. For any reuse or redistribution, researchers must make clear to others the licence terms of this work.**

I declare that this thesis and the research that is here presented, are product of my own work, and that ideas or quotations from the work of other people are fully acknowledged and appropriately referenced.

Giuseppe Antonacci

# Abstract

In a world where science is constantly challenged to solve problems of increasing complexity, light is paving new ways to gather information about the physical properties of matter. Among these properties, elasticity is becoming fundamental in the understanding and the diagnosis of several diseases. Current solutions to gather mechanical information, however, measure the response of a material to an applied excitation, which makes them invasive and limited by a low spatial resolution. In contrast with these techniques, Brillouin spectroscopy offers the unique solution to retrieve stiffness information from the spectrum of the light scattered by inherent thermal acoustic waves.

The combination of Brillouin spectroscopy with confocal microscopy has yielded a confocal Brillouin microscope able to perform mechanical imaging in a non-invasive manner. This was used to investigate two different biological problems: on the one hand the stiffness variations in specific endothelium cells of the eye, aiming at a better understanding of the mechanisms responsible for glaucoma, and on the other the characterisation of the mechanical structures of blood vessels, which could provide fundamental information regarding the formation of atherosclerotic plaques.

Following an investigation on the optimal geometry that minimises the spectral broadening caused by the collection of photons over a range of scattering angles, high resolution Brillouin imaging was obtained in a confocal backscattering arrangement. To the best of our knowledge this thesis presents, for the first time, sub-cellular Brillouin images. In particular, *in vitro* Brillouin images of single HUVEC cells were acquired to investigate the cell's mechanical response to the application of the *Latrunculin-A* drug. This analysis, together with the finding of a linear correlation between the Brillouin modulus and the standard Young's modulus, validates the technique as a feasible means of measuring stiffness. Following this assessment, Brillouin images of normal and diseased vessels were acquired showing that the atherosclerotic plaques had a lower stiffness compared to both diseased and healthy vessel walls. These results might encourage the application of confocal Brillouin microscopy as the tool of choice for the investigation of the arterial biomechanics.

*To my father.*

# Acknowledgments

During the period of my Ph.D. research at Imperial College, I grew up not only as a scientist, but also and most importantly as a person. I felt frustrated many times struggling to understand the Physics and fighting to obtain results. Nevertheless, this feeling was suppressed by the enormous accomplishment that I felt when I met the goals that I had originally set. I approached to the scientific world with the eyes of a child. I made mistakes from which I have learnt. However, I am very honest when I say that I committed myself in this research wholeheartedly.

Many people have contributed to the success of this challenging project. First of all, I thank my supervisor Peter Török who has always believed in me. I remember how keen I was four years ago to work with Peter, struggling to find a scholarship that subsidised my studies. I believe that together we achieved a lot in many aspects. We obtained important results in what we might considered a new field of microscopy, we have been successful in getting fundings and established connections with several research groups. Since I was the only Ph.D. student when I started, I am now happy to see that Peter's group is growing and counts of many new Ph.D. students and two postdocs (including me). Peter not only has contributed enormously on my scientific knowledge, but he has also been an important life teacher. I believe that we both have gained knowledge of ourself during these years and I honestly think that I am a stronger person now.

Many other people have given a great contribution to the accomplishment of the present research. Just to mention a few, I would like to thank my co-supervisor Carl Paterson for his precious teachings; Carlos Macias Romero who has introduced me in a real laboratory environment. I thank Matthew R. Foreman for sharing with me

his great knowledge in Optics which led us to a better understanding of the spectral broadening of the Brillouin spectrum. I would also like to thank Pavel Ramirez and David Mack for their friendship and constant support; Guillaume Lepert for the productive conversations; Marta Suarez and Thorin Duffin for the grammar corrections.

During these years, we have established new collaborations with two different research groups. I thank both for their great support to the project. In particular, I would like to thank Rob Krams and Ryan Pedrigi, who have conducted the biological work related to the investigation of the mechanical properties of the blood vessels responsible for atherosclerosis; Darryl R. Overby and Sietse Braakman who have conducted the biological work related to the investigation of the mechanisms that lead to glaucoma. I sincerely hope that our strong efforts will contribute to the scientific progress for a better understanding of both atherosclerosis and glaucoma diseases affecting millions of people worldwide.

I am also very thankful to all the people external to Imperial College who have contributed to the design of the Brillouin microscope. First of all, I would like to express all my gratitude to Shin-ichi Itoh from Tokyo who was fundamental in the development of the very first experimental setup that enabled the first acquisition of a Brillouin signal. Although I have never met him, I will never forget his noble will to help me. A special mention is deserved to Giuliano Scarcelli and Seok-Hyun Yun for having invited me in their laboratory at Harvard Medical School and for all what I have learnt from them about VIPA spectrometers. I also thank Kristie Koski and Tom O'Haver for their contribution to the development of computational codes that we used for data processing.

Finally, yet by no means least, I deeply thank all the members of my family. My mother, my father and my sister who have always supported me in the difficulties that I faced during my Ph.D. They gave me the strength to go forward and never give up. I thank all my friends for their support and the powerful exchange of ideas. In particular, my SCR mates Benjamin Franchetti, Fabrizio Cavallo Marincola, Duccio Piovani and Niccolo Corsini. I do acknowledge EPRSC which have founded my DTA scholarship.

I can see more clearly now how life must be a team game and not a lonely journey.

# Contents

**Abstract** **7**

**Acknowledgments** **11**

**Contents** **13**

**List of Figures** **17**

**List of Tables** **27**

**Abbreviations** **29**

**1 Introduction** **31**

1.1 Elastography . . . . . 32

1.2 Historical Overview on Brillouin Spectroscopy . . . . . 34

**2 Light Scattering** **37**

2.1 Overview . . . . . 37

2.1.1 Spontaneous and Stimulated Light Scattering . . . . . 38

2.2 Scattering from a Single Particle . . . . . 39

2.3 Raman Scattering . . . . . 42

2.4 Spontaneous Brillouin Scattering . . . . . 43

2.4.1 Spectral Shift and Linewidth . . . . . 43

2.4.2 Landau-Placzek Ratio . . . . . 47

2.5 Mechanical Properties . . . . . 48

2.5.1 Elastic Moduli . . . . . 49

**3 Multiple Beam Interference** **53**

3.1 Fabry-Pérot Interferometer . . . . . 54
3.2 Virtually Imaged Phased Array (VIPA) . . . . . 57
3.2.1 Optical Arrangement . . . . . 58
3.2.2 VIPA Illumination . . . . . 59
3.2.3 Finesse Optimisation . . . . . 60
3.2.4 Laser Longitudinal Modes . . . . . 64
3.2.5 VIPA Calibration . . . . . 66
3.3 Multistage VIPA etalons . . . . . 68
3.3.1 Cross-axis Cascading of Spectral Dispersion . . . . . 69
3.3.2 Two-Stage VIPA Spectrometer . . . . . 70
3.3.3 Apodization Beam Shaping . . . . . 76
3.3.4 Throughput and Extinction Measurement . . . . . 79
3.4 Spectral Contrast Enhancement . . . . . 81
3.4.1 Molecular Absorption Filter . . . . . 82
3.4.2 Heterodyne Interferometry . . . . . 83
3.4.3 VIPAs of different dispersion power . . . . . 86

**4 Experimental Methods** **89**

4.1 90° Scattering Geometry . . . . . 90
4.1.1 Data Fitting . . . . . 93
4.1.2 Spectral Axis Linearisation . . . . . 94
4.1.3 Brillouin Spectra of Liquids . . . . . 96
4.2 Spectral Broadening in Brillouin Imaging . . . . . 98
4.2.1 Numerical Aperture and Spatial Resolution . . . . . 99
4.2.2 Spectral Distribution for High NAs . . . . . 102
4.2.3 Computational and Experimental Results . . . . . 106
4.3 Dark-Field Brillouin Microscopy . . . . . 110
4.3.1 Dark-Field Arrangement . . . . . 112
4.3.2 Annular Beam Illumination Optimisation . . . . . 114
4.3.3 Data Acquisition and Image Processing . . . . . 120
4.4 Dark-Field Imaging . . . . . 121
4.4.1 Preliminary Brillouin Imaging . . . . . 123

4.5 Confocal Brillouin Microscopy . . . 125
4.5.1 Principles of Confocal Imaging . . . 125
4.5.2 Confocal Optical Setup . . . 127

**5 High Resolution Brillouin Imaging** **131**
5.1 Young's Modulus Correlation . . . 132
5.2 Cell Mechanics in Glaucoma . . . 133
5.2.1 Cell Culture . . . 134
5.2.2 *In vitro* Single Cell Mechanical Imaging . . . 135
5.2.3 *Latrunculin-A* for Stiffness Assessment . . . 137
5.3 Arteries Mechanics in Atherosclerosis . . . 139
5.3.1 Sample Preparation . . . 141
5.3.2 Artery Mechanical Imaging . . . 142
5.3.3 Mechanical Imaging of Atherosclerotic Plaques . . . 145

**6 Conclusions** **149**

**A Beam Convergence** **153**

**B Brillouin Spectra of Liquids** **155**

**Bibliography** **161**

# List of Figures


2.1 Typical spectrum of the scattered light composed of a central Rayleigh peak followed by a Brillouin and a Raman peak on each side. The two inelastic side bands are referred to as the Stokes and the Anti-Stokes peaks associated with a lower and higher frequency shift respectively. 38

2.2 Scattering geometry for an incident field $\mathbf{E_i}$ linearly polarised along the $\hat{y}$ axis. $\mathbf{r}$ is the position vector at an observation point $Q$ in space relative to the radiating dipole whilst $\vartheta$ is the angle between the dipole moment $\mathbf{p}$ and $\mathbf{r}$. . . . . 40

2.3 Intensity distribution of the scattered light by an electric dipole of momentum vector $\mathbf{p}$. The scattered field shows an axial symmetry with respect to the dipole orientation. Intensity decreases from red to blue. . . . . 41

2.4 Polar diagram of the scattering distribution generated by linearly polarised light of $\lambda = 550$ nm. As the radius of the particle $a$ approaches to the wavelength, the scattering field increases in the forward direction of the incident beam. . . . . 42

2.5 Stoke and Anti-Stoke frequency shifts diagram. The direction of the phonon wavevectors $\mathbf{q}$ is responsible for the frequency shift due to the Doppler effect. . . . . 44

2.6 Energy (left) and momentum (right) conservation diagram. In the Stokes process the incident photon energy is conserved with the creation of a scattered photon and an acoustic phonon. The angle $\psi$ between incident and scattering wavevectors defines both the frequency shift and the spectral linewidth. . . . . 45

2.7 Typical stress-strain curve formed by an elastic and an inelastic region. The slope of the curve in the linear regime gives the stiffness of a material. . . . . 49

2.8 Diagram of the longitudinal tensile stress a) and the shear stress b). The ratio of the stress and the strain gives the Young's and shear moduli. . . . . 49

2.9 Diagram of the compressive stress and the resulting orthogonal strain. The Poisson's ratio measures the material expansion to an applied compression. . . . . 52

3.1 Transmission and reflection fields of a Fabry-Pérot interferometer. . . 54

3.2 Normalised Airy functions of a Fabry-Pérot for different finesse $\mathcal{F}$ values. The peak separation $\Delta\nu$ and the linewidth $\delta\nu$ define the FP free spectral range and the spectral resolution, respectively. . . . . 56

3.3 Basic diagram of a VIPA etalon. The input beam enters at a certain angle through the AR coated window and undergoes multiple reflections inside the cavity as in a normal FP etalon. . . . . 58

3.4 Diagram of the optical arrangement of a VIPA spectrometer. The scattered radiation delivered by a single-mode fibre is first collimated and then focused by a cylindrical lens to the VIPA entrance window. A spherical lens translates the spectral content into a spatial domain. The spectrum is recorded by a CCD camera allowing fast data acquisition. . . . . 59

3.5 Angular intensity distribution at the VIPA Fourier plane. The straight fringes (blue) are confined in a Gaussian envelope (red) defined by the convergence angle of the focused beam. The strength of the Brillouin signal is maximised when the Gaussian encloses only two subsequent orders. . . . . 60

3.6 Gaussian beam convergence along the focal region (left) and at the VIPA entrance window (right). Refraction was neglected for a small angle $\theta_0$. The beam waist $w_0$ is defined at $z = 0$. Adjacent radii ($w_1$ and $w_2$) are located at a distance $d$ with each other. In order to minimise $\theta_0$, the sum of the beam radii at the first VIPA surface needs to be minimum. . . . . 61

3.7 Ray tracing diagram of a beam incident at an angle $\theta_0$ with convergence $\alpha$. The beam waist is located at the second surface of the VIPA. The beam radius at the first surface after one reflection is given by $w_1 = w(d)$. . . . . 63

3.8 Multiple simultaneously oscillating longitudinal modes in a HeNe laser cavity. . . . . 65

3.9 Normalised intensity profile as a function of the pixels number (top) obtained from a linescan (white dotted line) across the interference fringes shown in the bottom false coloured image. Blue dots are the experimental data. . . . . 67

3.10 Dispersion axis in the case of a single (left) and a double stage (right) VIPA. In the first case, dispersion occurs along the same axis where the crosstalk (green line) arises. Conversely, the dispersion axis lies on a diagonal direction when two VIPA etalons of equal dispersion power are crossed. This enables the Brillouin doublet to be spatially separated from the crosstalk. . . . . 70

3.11 Diagram of a two-stage VIPA spectrometer. The two etalons are crossed with respect to each other. A spatial mask is placed between the two VIPAs in order to suppress part of the elastic light distributed along the vertical direction. . . . . 71

3.12 Transmission profile measured for the front (red) and rear (black) HR coated surfaces of the VIPA in the spectral range of $450 - 570$ nm. . 72

3.13 a) Spectral pattern at the detector plane without masks along the spectrometer. b) The application of a spatial mask in the first relay system allows the crosstalk along the horizontal direction to be cut off. A greater spectral extinction facilitates the localisation of the Brillouin doublet lying along the diagonal dispersion axis. . . . . 74

3.14 a) Relay telescope diagram in a $4f$ arrangement, and b) with a distance between first VIPA and doublet shorter than the lens focal length. The Seidel diagrams c) and d) show an increase in the off-axis optical aberrations when the $4f$ symmetry is broken. Grid lines are spaced by 10 $\mu$m. . . . . 75

3.15 Circular, continuously variable neutral density filter (left). The filter was translated along the $\hat{x}$ direction so that the transmitted beam intensity was measured within the region of transition (red line) passing from an OD = 0 to OD = 4. The resulting transmission profile (right) in this region is shown to be smoother than a theoretical step function. . . . . 77

3.16 Product of an exponential function (red) characterising the intensity output of the VIPA and the transmission profile obtained with the neutral density filter. . . . . 78

3.17 Interference pattern of a two-stage VIPA spectrometer. The intensity of the spectral peaks due to the laser radiation was set to be equal. The highest OD filter was first used to keep the interference peaks below the saturation level of the CCD camera. A linescan (red line) along two subsequent interference orders was performed to retrieve the intensity profile. . . . . 80

3.18 Normalised spectral response of both single (red) and double (blue) stage VIPA spectrometer to a single longitudinal mode laser radiation. The extinction ratio increases by 30 dB from a single to a double stage spectrometer. . . . . 81

3.19 Diagram of the vapour cell arrangement. The output beam of the fibre passes through the vapour cell where absorption of the Rayleigh scattered light takes place. The cell is heated up to a temperature of 100 °C. . . . . 82

3.20 Optical arrangement for a Michelson interferometric system. The Rayleigh scattered light is suppressed by destructive interference with a reference signal coupled into a single mode fibre. . . . . 85

3.21 Logarithmic intensity of a two-stage VIPA of free spectral ranges $\Delta\nu_1 = 33$ GHz and $\Delta\nu_2 = 20$ GHz. The Anti-Stokes dispersion axis (white arrow) is formed at 45° with respect to the first VIPA dispersion axis along the $\hat{x}$ direction. . . . . 87

4.1 Optical setup for a 90° scattering geometry. . . . . 91

4.2 Least-squares fit of the Brillouin spectrum of Benzene (top) and raw fringe pattern acquired by the CCD camera. Blue dots represent experimental data. Bespoke algorithms decompose the signal into the three components (green lines) whose sum makes up the resulting profile (red line). A Lorentzian function is used to fit the spectral peaks. 94

4.3 Measured spectral intensity of liquid benzene for seven subsequent interference orders. The separation between the Rayleigh peaks observed in the graph decreases as the square root of the $\hat{x}$ axis, which is here expressed in terms of the camera pixel numbers. . . . . 95

4.4 Measured Rayleigh peaks separation in pixel units on a linear scale (left). In order to perform an accurate fit (red line), seven successive interference orders were taken into account. Linearised spectrum for liquid benzene (right). The separation between successive orders is associated with the FSR in the spectral domain. . . . . 96

4.5 Fitted Brillouin spectra (solid lines) for different liquids obtained in 90° scattering geometry with NA = NA′ = 0.03. Individual spectra have been normalised to the central Rayleigh peak. Experimental data points for methanol (dots) are also shown for comparison. Each spectrum was acquired using a 2 second exposure time and a HeNe laser providing 10 mW at the sample plane. . . . . 97

4.6 Collimated beam focused by a circular lens of radius $a$ and focal length $f$. The NA of the lens in air ($n = 1$) is defined by the angle $\alpha = \tan^{-1}(a/f)$. . . . . 100

4.7 Longitudinal (left) and transverse (right) intensity distribution at the focal region of a perfect thin lens. . . . . 102

4.8 Schematic of scattering geometry showing the Gaussian reference spheres for illumination and collection lenses. The direction of incident and scattered photons are defined by the wave-vectors $\mathbf{k}(\theta, \phi)$ and $\mathbf{k}'(\theta', \phi')$ respectively. . . . . 103

4.9 Logarithmic spectral intensity as a function of NA for scattering from liquid benzene in a 90° (left) and 180° (right) geometry. The spectrum is normalised to the peak Rayleigh intensity at each NA. White dashed lines show the theoretical position of the Brillouin peak for NA = 0. (Inset) Total integrated intensity as a function of NA. . . . . 107

4.10 Relative shift of Brillouin peak from $\nu_B^{90,180}$ (left) and FWHM (right) as a function of the NA (left). . . . . 108

4.11 Brillouin peak linewidth measurements (blue circles, with accompanying error bars) as a function of the NA for $\Psi = 90°$ (left) and $\Psi = 180°$ (right). Black solid curves depict theoretical predictions. . 109

4.12 Dark-field microscope diagram. An annular beam was generated by means of a customised prism. Illumination and collection occurred with the same microscope objective. A SM fibre ensured strict confocality and flexible beam delivery to a single-stage VIPA spectrometer. 112

4.13 Three dimensional (left) and 2D top-down (right) representation of the 45° angled prism designed with the engineering software *SolidWorks*. The front surface was polished and coated with silver to maximise reflectivity. . . . . 113

4.14 Annular illumination diagram. The outer radius $b$ coincides with aperture radius of the microscope objective. Collection occurs through the central region of the same lens defined by the radius $a$. . . . . 115

4.15 Normalised intensity distributions along the transverse (left) and longitudinal (right) directions for a lens of NA=0.5. The total intensity is compared with the illumination and collection distributions. First minimum of the longitudinal distribution appears an order of magnitude larger than in the transverse case. . . . . 116

4.16 Total power collected by the dark-field system for different ratios of the inner and the outer radius of the annular illumination beam. The curve shows that the optimal performance is given by $a/b \simeq 0.66$. . . 118

4.17 Percentage of power delivered to the sample as a function of the ratio $w/b$. The power is shown to be maximised for a laser radius of $w \simeq 1.6b$. 119

4.18 Dark-field image of an object taken with stage steps of 5 $\mu$m (a). USAF test resolution target used as a sample across the number 6 (b). Image of a small region of the same object taken with stage steps of 2 $\mu$m (c). Only the edges of the images (a) and (c) are bright because of the absence of surface reflections at detection. . . . . 122

4.19 Brillouin image of two-liquid interface (left) and associated dark-field image (right). The water drop (red spot) can be distinguished from the oil in the Brillouin image only. . . . . 123

4.20 1D spatial distribution of the frequency shift (left) and the linewidth (right) of the Brillouin peaks along the two-liquid interface. . . . . 124

4.21 Diagram of a confocal system. A point source emits light which passes through a spatial filter placed at an intermediate conjugate plane so to remove the out-of-focus radiation. This allows a greater axial resolution to be achieved compared to that given by conventional bright field microscopes. . . . . 126

4.22 Transverse (left) and longitudinal (right) intensity distributions of a confocal imaging system characterised by a plane wave (red) and an annular dark-field (blue) illumination. . . . . 127

4.23 Final confocal arrangement for fast high resolution Brillouin imaging. A two-stage VIPA spectrometer was employed to ensure high spectral contrast. A reference signal from water is taken to measure the frequency shift of the Brillouin spectra during the processing. . . . . 128

5.1 Measured Brillouin modulus as a function of the Young's modulus for PDMS gels (left) and silicon rubber sheets (right). The fits suggest that the two moduli are linearly correlated. However, the results show that the linear relationship varies depending on the material. . . . . 132

5.2 Sample dish diagram. Cells were cultured in a PBS buffer solution. A gelatin film of $< 50\,\mu$m thickness was spin coated on top of the coverslip so as to reduce the refractive index mismatch at the sample interface. . . . . 135

5.3 Brillouin image of a single HUVEC cell. Both the nucleus membrane and the four nucleoli can be identified and appear to have a higher stiffness than the surrounding cytoplasm. . . . . 136

5.4 Phase contrast image of the HUVEC cell. The sample was entirely illuminated by the microscope phase contrast mode and acquired by a Pulnix CCD camera. . . . . 137

5.5 Brillouin images of a HUVEC cell before (left) and after (right) the addition of Latrunculin-A. The stiffness images were normalised to the modulus of PBS solution. A 4% decrease in stiffness was found after the drug addition. . . . . 138

5.6 Diagram of a normal (left) and a diseased (right) coronary artery. The artery becomes narrower and stiffer due to the formation of atherosclerotic plaques. . . . . 139

5.7 Brillouin image of a cross section of a normal mouse blood vessel. The adventia appears to be stiffer compared to the inner substrate, as suggested by morphological studies. . . . . 142

5.8 Associated phase contrast image of the artery cross section. . . . . 143

5.9 High resolution Brillouin image of a small region of a normal artery cross section. The image confirms a higher stiffness for the adventia. Interestingly, layers of different elasticities can be identified within the tunica wall. . . . . 144

5.10 Cross sectional Brillouin image of a mouse blood vessel affected by atherosclerosis. The outer tissue appear to be stiffer with respect to the plaque. The image suggests that the plaque is formed of a variety of organic materials of different stiffnesses. . . . . 146
5.11 Associated phase contrast (left) and stained (right) images of the same diseased artery cross section. The red colour outlines the plaque region due to the high lipid concentration. . . . . 147
5.12 Average stiffness of the diseased vessel intima and both diseased and control walls. $n$ is the number of sections analysed. The data shows that the atherosclerotic plaque has a lower stiffness than the diseased and normal wall. . . . . 147

A.1 Angular separation between two interference orders at the FP output. 153

B.1 Experimental data and least-squares fitting (top) with residual data points (bottom) for methanol. . . . . 155
B.2 Experimental data and least-squares fitting (top) with residual data points (bottom) for water. . . . . 156
B.3 Experimental data and least-squares fitting (top) with residual data points (bottom) for toluene. . . . . 157
B.4 Experimental data and least-squares fitting (top) with residual data points (bottom) for ethanol. . . . . 158
B.5 Experimental data and least-squares fitting (top) with residual data points (bottom) for benzene. . . . . 159

# List of Tables

4.1 Experimental and theoretical values of the Brillouin frequency shift for different liquids as found from spectra acquired in a 90° scattering geometry at room temperature with NA = NA′ = 0.03. . . . . 98
4.2 Liquid benzene thermodynamic parameters. . . . . 107

# Abbreviations

| | |
|---|---|
| **AFM** | Atomic Force Microscopy |
| **AOI** | Area of interest |
| **AR** | Anti-reflection |
| **CAD** | Coronary Artery Disease |
| **BS** | Beam splitter |
| **DPSS** | Diode-pumped solid-state |
| **FP** | Fabry-Pérot |
| **FSR** | Free spectral range |
| **FWHM** | Full width at half maximum |
| **HR** | High-reflection |
| **HUVEC** | Human Umbilical Vein Endothelial Cells |
| **HWHM** | Half width at half maximum |
| **IOP** | Intraocular pressure |
| **LIDAR** | Light Imaging Detection and Ranging |
| **MI** | Myocardial infarction |
| **MRI** | Magnetic Resonance Imaging |
| **NA** | Numerical Aperture |
| **OCE** | Optical Coherence Elastography |
| **OCT** | Optical Coherence Tomography |
| **OD** | Optical Density |
| **OE** | Optical Elastography |
| **PALM** | Photoactivated Localization Microscopy |
| **PBS** | Phosphate buffered saline |
| **PSF** | Point Spread Function |
| **PWV** | Pulse wave velocity |

| | |
|---|---|
| **SC** | Schlemm's canal |
| **SNR** | Signal-to-noise ratio |
| **STORM** | Stochastic Optical Reconstruction Microscopy |
| **TIRM** | Total Internal Reflection Microscopy |
| **VIPA** | Virtually Imaged Phased Array |

# Chapter 1

# Introduction

Elasticity is a fundamental physical property of materials that has been the subject of research in many scientific fields. Over the last decade, a strong interest has grown in characterising the elasticity of microscopic-scale systems, such as biological tissues and cells. Several diseases have been associated with biomechanical changes of specific organic systems of the human body. Current solutions to measure mechanical properties of materials rely on the response analysis of an applied excitation to a specimen, which makes them destructive and limited by a poor spatial resolution. This project aims to develop a microscope based on spontaneous Brillouin light scattering which enables high resolution mechanical imaging in a non-invasive manner.

The thesis gives a detailed description on both the theory and the experimental techniques required to develop a confocal Brillouin microscope, which was applied to the investigation of tissue and cell mechanics responsible for diseases such as glaucoma and atherosclerosis. The manuscript starts from a general overview on Brillouin spectroscopy, describing its evolution from a point sampling technique into a new imaging modality. The theory governing the physical principles of spontaneous Brillouin light scattering is given in Chapter 2. Chapter 3 introduces a new type of Fabry-Pérot (FP) etalon which was employed in our spectrometer to disperse the inelastic scattered light. The experimental methods used to obtain high resolution Brillouin imaging are explained in Chapter 4. Final results are presented

and discussed in Chapter 5.

## 1.1 Elastography

Elastography refers to the field of research that aims to study elasticity properties of biological systems by different imaging techniques. Standard imaging modalities are based on ultrasound waves and magnetic resonance. Ultrasound techniques use high-frequency sound waves to image internal body structures such as soft tissues and organs [1, 2]. Ultrasound pulses are sent into the body by means of a transducer and their reflections (echoes) are recorded to yield an image. On the other hand, Magnetic Resonance Imaging (MRI) uses strong magnetic fields and radio waves to yield an image of the body anatomy [3, 4]. Although these techniques have been extensively used in clinical practices as the main diagnostic tool for diseases such as cancer and coronary atherosclerosis, they are inherently limited by a spatial resolution of the order of hundreds of microns [5].

Over the last decades, the scientific community has made great efforts to increase the spatial resolution of elastography imaging systems to a micrometer scale. This would enable mechanical properties of small biological systems (e.g. cells) to be investigated and eventually lead to a better understanding and an earlier prevention of diseases. The employment of light as a means to accomplish this goal has led to the establishment of Optical Elastography (OE). OE is a rapidly expanding field of research that aims to gain elasticity information of biological specimens by optical and mechanical means. As a result of the work by research groups world-wide, OE is fast becoming indispensable in a wide range of biological applications, such as the understanding of the origin of cardiovascular diseases, glaucoma, embryogenesis and bacterial meningitis, just to mention a few. Current solutions for micro-scale elastography rely on analysing the response of a tissue sample to an invasive mechanical excitation, which makes these techniques both destructive and difficult to use *in situ* and virtually impossible to implement *in vivo*. For instance, Optical Coherence Elastography (OCE) makes use of Optical Coherence Tomography (OCT) to generate high resolution stiffness images and has been applied to study deformation of tissues under compressive loads [5, 6, 7, 8]. The application of external loads to

retrieve elasticity information makes this technique invasive and eventually destructive. Furthermore, results are difficult to reproduce because of the requirement of identical loads conditions [5].

Dynamic viscoelastic properties of living cells in culture have been partially investigated by means of Atomic Force Microscopy (AFM) nanoindentation [9, 10, 11]. In more details, AFM imaging is combined with the indentation process to image the spatial distribution of cell mechanics [12]. Sharp indenters are used to probe the cell cytoskeleton, and hardness information is derived by analysing the force response through different contact models [12]. The dependency of these models on the indenter tip geometry and size has been the main reason for a significant uncertainty on the data acquired by AFM elastography. In addition, this technique can only measure surface stiffness of samples with a penetration depth of $1 - 20$ nm [13]. Consequently, this cannot provide three dimensional stiffness images of cells. Spatial resolution is determined by the tip radius, which for many biological applications is usually of the orders of hundred nanometers. In fact, the smaller the tip radius, the deeper the penetration inside the cell membrane which ultimately can lead to irreversible damages [12].

In contrast to these techniques, Brillouin spectroscopy permits the determination of the elasticity modulus of sample volumes of a few cubic mm, predominantly determined by the beam diameter of the laser illuminating the sample. The light scattered elastically (Rayleigh) from the tissue has the same frequency as the illumination. The spectrum however contains two inelastic side bands, usually referred to as the Stokes and Anti-Stokes Brillouin peaks. These are typically shifted by a few GHz from the Rayleigh frequency. The location, width and strength of the Brillouin peaks of the light scattered off the sample are measured and elasticity data is derived in a non-invasive manner. The combination of Brillouin spectroscopy with confocal microscopy has yielded a confocal scanning Brillouin microscope that permits 3D imaging of the tissue stiffness.

Hitherto Brillouin imaging has only been used with low numerical aperture (NA $< 0.2$) microscope objectives resulting in rather large probe volumes. Primarily, this restriction arose in an attempt to limit spectral broadening of the Brillouin peaks associated with collection of photons over a wide range of scattering an-

gles. The theoretical and experimental results presented in the thesis show that the spectral broadening is minimised in a backscattering geometry [14]. Consequently, elasticity information can be acquired from sample probe volumes smaller than a cubic micron due to the optical sectioning ability of the confocal arrangement. In our setup the light of a single longitudinal-mode laser is focused into the sample and the scattered light is collected and spectrally analysed by multiple etalons in a cross-axis configuration.

## 1.2 Historical Overview on Brillouin Spectroscopy

Light scattering is progressively becoming a reliable means to study intrinsic properties of both organic and inorganic materials. The scattering of light is a physical process that can be classified to be either of elastic or inelastic nature. Rayleigh scattering is the dominant elastic scattering process arising from the interaction of photons with particles of smaller dimension than the wavelength of light [15]. This has been widely used to determine molecular dimensions [16] and to enhance the imaging contrast of transparent samples [17]. On the other hand, Raman scattering is an inelastic scattering process that stems from the interaction of photons with the vibrational and rotational modes of molecules [18]. The frequency shift of the Raman scattered light provides important information about chemical bonds, molecular structures and intermolecular interactions of matter. For this reason, Raman scattering has been widely employed in biomedical sensing and diagnosis of diseases such as cancer [19, 20].

Brillouin scattering, first reported in 1922 [21], is a weak inelastic scattering process arising from the interaction of light with inherent thermal density fluctuations propagating at the hypersound velocity inside media. Unlike standard contact techniques described previously, Brillouin spectroscopy allows mechanical properties of materials to be determined in a non-invasive and non-destructive manner.

Since the advent of lasers, Brillouin spectroscopy has been extensively used to study thermodynamic and viscoelastic properties of materials [22, 23], such as the strain and temperature of solids [24, 25]; the elastic constants as a function of both pressure [26] and temperature [27]; the temperature phase transitions in crystals [28,

29]; and both hypersound velocity and heat ratio in liquids [30]. The complete elastic tensor of spider silks has been determined by analysing the Brillouin spectra obtained from different optical geometries [31]. Interfacial hydrodynamics investigations in solid-liquid interfaces have also been carried out by near-field Brillouin scattering where an evanescent field has been used to illuminate the samples [32, 33, 34]. Furthermore, the acoustic dispersion behaviors of polymers at hypersonic frequencies [35, 36] has been determined by means of a backscattering arrangement.

The frequency shift of the inelastic scattered light due to thermal density fluctuations in media is typically within a range of $1 - 50$ GHz. This imposes a minimum resolving power of $\mathcal{R} > 10^6$, which standard spectrometers are not able to achieve [37, 38]. Since the release of piezoelectric stages, the Brillouin spectrum has been commonly investigated by scanning the optical cavity of Fabry-Pérot interferometers [39] and collected by means of single channel detectors such as high-sensitivity photodiodes and photomultipliers [37, 40, 41]. The development of new high-sensitivity multichannel detectors has enabled a more robust non-scanning mode using fixed cavity length FP etalons [42, 43, 44]. In this case, fast area detectors (e.g. CCD and photodiode arrays) have been employed, allowing the entire Brillouin spectrum to be collected in a single frame. Consequently, data acquisition times have been decreased from several hours to a few minutes. In addition, the obstacle of maintaining a sensible parallelism between the FP surfaces during the scanning process has been overcome by the use of the etalons [45, 46].

In 2005, Brillouin spectroscopy was extended, for the first time, from a point sampling technique into a new imaging modality. The first attempt was made by Koski and Yarger [47] with the design of a Brillouin imaging system in a backscattering geometry. Images from liquid interfaces were acquired. An adjustable slit was placed at the Fourier plane of a confocal arrangement to spatially filter the scattered light arisen from the probe volume. A Fabry-Pérot etalon of free spectral range of 30 GHz and a mirror reflectivity of 99.5% was used to disperse light. The Brillouin spectra were acquired by a cooled CCD camera with an exposure time of approximately 10 seconds. Nevertheless, the system designed by Koski was limited by a spatial resolution of $20\,\mu$m in an attempt to limit the spectral broadening arising from the employment of finite instrumental numerical apertures. A description and

analysis on the Brillouin spectral broadening is given in Section 4.2.

A fundamental step forward in Brillouin imaging has been enabled by the development of a novel type of Fabry-Pérot etalon known as Virtually Imaged Phased Array (VIPA) [48, 49]. This name is due to the similarity of the device operation with that of a series of multiple virtual sources interfering with each other as in a phased array [50]. The VIPA is an interference device formed of two high-reflectivity (HR) coated surfaces placed parallel to each other and incorporates an anti-reflection (AR) entrance window on one side that is used to minimise optical losses. Since spontaneous inelastic Brillouin scattering is a weak process, the employment of a VIPA spectrometer has been fundamental to enable fast data acquisition.

The elastic scattered light from biological samples is typically many orders of magnitude stronger than the Brillouin signal. For this reason, a high spectral contrast is required to perform spectral analyses of the Brillouin scattered light. A significant enhancement of the extinction ratio has been achieved by the development of a two-stage VIPA spectrometer [51]. A two-stage VIPA spectrometer employs two etalons of equal powers crossed with each other to spatially separate the Brillouin spectral peaks from the strong crosstalk caused by the elastic signal.

In 2008, biochemical images of the crystalline lens of a mouse eye were acquired by Scarcelli and Yun [52]. A confocal Brillouin microscope was designed with a dual-axis configuration of 6° beam cross angle to reduce collection of specular reflections [53]. A low NA microscope objective was engaged providing a lateral resolution of 6 $\mu$m and an axial resolution of 60 $\mu$m. A two-stage VIPA spectrometer with etalons of finesse 56 and free spectral range of 33.3 GHz was used to measure the Brillouin frequency shift and to enable fast acquisitions. With 10 mW at the sample plane, Brillouin spectra were acquired with a one second exposure. A single mode optical fibre was employed to ensure strict confocality, flexible beam delivery and minimal collection of stray light.

To date, Brillouin microscopy has enabled *in situ* and *in vivo* biomechanical imaging of the eye cornea and lens [52, 54, 55]. In this thesis Brillouin images of single cells and cross sections of coronary vessels are presented.

# Chapter 2

# Light Scattering

## 2.1 Overview

Light scattering is a phenomenon arising from the interaction of photons with matter. This process can be classified to be either of elastic or inelastic nature depending on the energy transfer during the interaction. This chapter gives an overall view on the theory of light scattering with a particular emphasis on inelastic Brillouin scattering.

There are several factors which give rise to different scattering scenarios. Particle size, vibrational and rotational modes of the molecules, thermodynamical properties of media, as well as both the polarisation and the angle of incidence of the beam of light are key parameters in different scattering processes. Figure 2.1 shows a diagram of the spectrum arising from the scattering of light by a variety of mechanisms. *Rayleigh scattering* is the dominant elastic process due to the instantaneous interaction of light with non-propagating density fluctuations of media [57]. *Brillouin scattering* and *Raman scattering* are the two inelastic scattering processes arising from the energy transfer during the interaction between incident photons and acoustic and optical *phonons* respectively. The Doppler effect [58] is responsible for either a gain (phonon generation) or a loss (phonon annihilation) in the energy of the scattering field depending on the propagation direction of phonons with respect to the

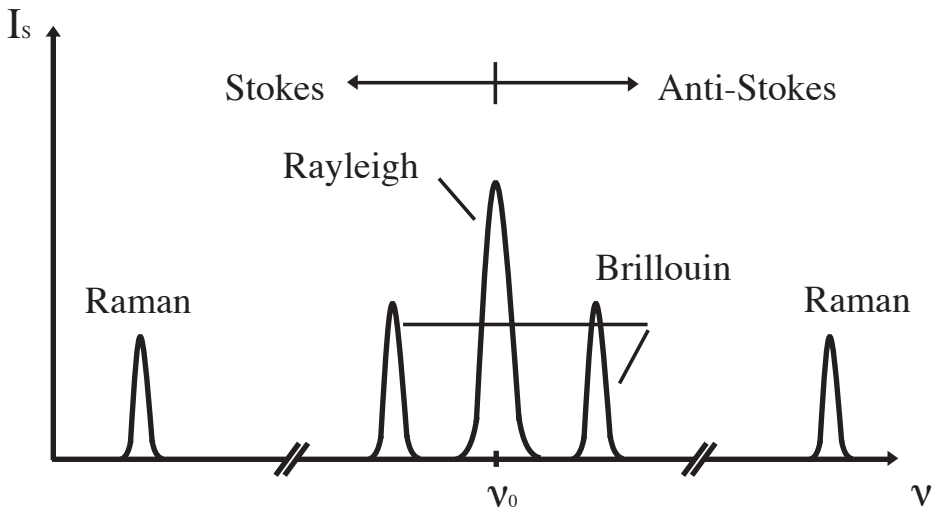



**Figure 2.1:** Typical spectrum of the scattered light composed of a central Rayleigh peak followed by a Brillouin and a Raman peak on each side. The two inelastic side bands are referred to as the Stokes and the Anti-Stokes peaks associated with a lower and higher frequency shift respectively. After [56].

incident photons. As a result, the scattered radiation results to be of lower (*Stokes*) or higher (*Anti-Stokes*) frequency with respect to the incident one, as illustrated in Figure 2.1.

### 2.1.1 Spontaneous and Stimulated Light Scattering

Inelastic scattering is a nonlinear process which can occur in two different regimes depending on the intensity of the incident light. For low photon density, scattering is known as *spontaneous*. In this case, the scattered light is proportional to the incident intensity and the process can be described by a quantum mechanical approach. However, when the incident power reaches a certain threshold, material fluctuations become altered by the strong electromagnetic field leading to a *stimulated* excitation of the medium. Stimulated light scattering can be described by semi-classical wave theory and has been found to occur in quartz and sapphire when the power density reaches $10^6\,\mathrm{W/cm^2}$ [59] and no optical distortions in the crystals were involved. Above this threshold, the strong interactions between light and matter can also lead to a total conversion of incident to scattered light and to the suppression of the Anti-Stokes component [60].

Stimulated Brillouin scattering has been widely investigated in optical fibres where it can lead to unsuitable effects such as amplitude distortion and a decrease in the signal-to-noise ratio [61, 62, 63]. These side effects still represent one of the main limitations in optical fibre communication.

In the following sections, light scattering will be considered in the spontaneous regime only.

## 2.2 Scattering from a Single Particle

Light scattering is a weak process. Most of the light incident on a medium is transmitted or absorbed and only a small amount is scattered. This section gives a description of the field distribution of the elastically scattered light by single particles as a key starting point for the understanding of the principles of light scattering theory.

From a classical point of view, light is described as an electromagnetic wave. An electromagnetic plane wave $\mathbf{E}$ of angular frequency $\omega$ is defined by

$$\mathbf{E} = \mathbf{E}_0 \cos\left(\omega t - \mathbf{k} \cdot \mathbf{r}\right), \tag{2.1}$$

where $\mathbf{E}_0$ is the wave amplitude, $c$ is the speed of light and $\mathbf{k}$ is the wavevector parallel to the direction of propagation of the wave. Equation 2.1, the most fundamental solution of the electromagnetic wave equation, stems from Maxwell's equations [64]. In particular, the wave equation describing the propagation of electromagnetic waves in vacuum is expressed as [65]

$$\bigtriangledown^2 \mathbf{E} - \epsilon\mu \frac{\partial^2 \mathbf{E}}{\partial t^2} = 0, \tag{2.2}$$

where $\epsilon$ is the *dielectric constant* (or permittivity) and $\mu$ is known as the *magnetic permeability*.

An electromagnetic wave $\mathbf{E_i}$ incident on a particle of radius $a$ much smaller than the wavelength of light ($a \ll \lambda_0$) induces a dipole moment $\mathbf{p}$ given by

$$\mathbf{p} = \alpha_p \mathbf{E_i}, \tag{2.3}$$

where the *polarizability* $\alpha_p$ is a measure of the electric charge separation in the particle volume $V_p$ [15, 66]. Consequently, the particle behaves similarly to an electric dipole. When the oscillations of the positive and negative poles are subject to an acceleration, the electric dipole in turn yields a new electromagnetic wave of equal frequency with respect to the incident one and radiating in $(\mathbf{r}, t) = (x, y, z, t)$, where $\mathbf{r}$ is the position vector and $t$ is the time parameter. This process is known as *Rayleigh scattering*. Figure 2.2 illustrates the scattering geometry where the dipole vector $\mathbf{p}$ is parallel to the polarisation of the incident field $\mathbf{E_i}$ along the $\hat{y}$ direction. The far-field ($r \gg \lambda$) electric field $\mathbf{E_s}$ of a linear dipole of induced moment $\mathbf{p}$ in

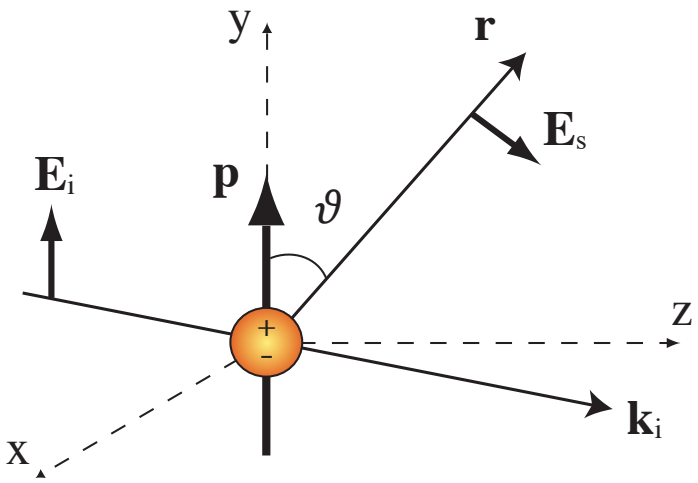



**Figure 2.2:** Scattering geometry for an incident field $\mathbf{E_i}$ linearly polarised along the $\hat{y}$ axis. $\mathbf{r}$ is the position vector at an observation point $Q$ in space relative to the radiating dipole whilst $\vartheta$ is the angle between the dipole moment $\mathbf{p}$ and $\mathbf{r}$.

vacuum is given by [65]

$$\mathbf{E}_s = -\frac{1}{4\pi\epsilon_0}\left(\frac{\omega}{c}\right)^2 \frac{1}{r^3}\,\mathbf{r}\times(\mathbf{r}\times\mathbf{p}), \tag{2.4}$$

where $\epsilon_0$ is the *vacuum permittivity* and $r$ is the modulus of the position vector (i.e. the distance of the observer from the dipole). Equation 2.4 shows that the scattered electric field $\mathbf{E_s}$ is proportional to the polarizability $\alpha_p$ as well as to the angle $\vartheta$ between the dipole moment vector $\mathbf{p}$ and the direction of observation $\hat{\mathbf{r}}$.

The general expression describing the angular intensity distribution $I_s \propto |\mathbf{E}_s|^2$

of the scattered light from a single dipole is given by [67]

$$\frac{I_s}{I_0} = k_s^4 \frac{\sin^2 \vartheta}{r^2} \alpha_v^2, \tag{2.5}$$

where $I_0$ is the intensity of the incident electromagnetic radiation, $k_s = 2\pi/\lambda$ is the wavenumber of the scattered light in a dielectric medium of refractive index $n$ ($\lambda = \lambda_0/n$), and $\alpha_v = \alpha_p/4\pi\epsilon_0$ is the *polarizability volume*. Equation 2.5 shows that for an incident linearly polarised light, Rayleigh scattering is maximised along the normal orientation of dipoles ($\vartheta = \pi/2$) whilst it is null along the dipole oscillating direction ($\vartheta = 0$). This can be observed in Figure 2.3, which shows that the three dimensional axial symmetry of the intensity distribution with respect to the dipole orientation results in a "donut" shape profile.

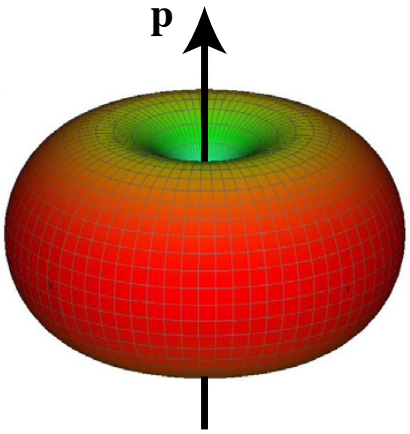



**Figure 2.3:** Intensity distribution of the scattered light by an electric dipole of momentum vector **p**. The scattered field shows an axial symmetry with respect to the dipole orientation. Intensity decreases from red to blue. From [68].

Figure 2.4 illustrates the scattered field distribution for different particle radii $a < \lambda_0$. For $a \longrightarrow 0$ the distribution resumes the donut shape illustrated in Figure 2.3. However, as the particle increases in size, the symmetry breaks and more light is scattered in the forward direction defined by the **k** vector of the incident radiation. This phenomenon is known as the *Mie effect* [65]. On the other side, when the particle radius is very large compared to the wavelength of the incident field ($a \gg \lambda_0$), light undergoes reflection as described by geometrical optics.

Another fundamental aspect is represented by the scattering dependence on the

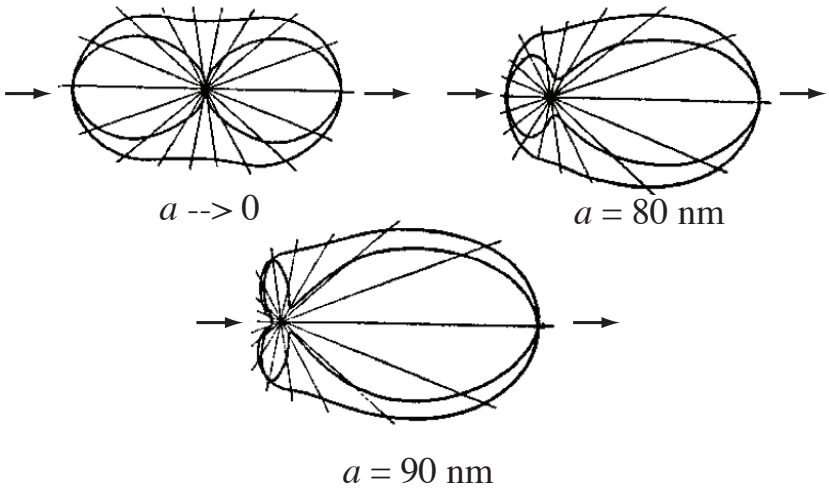



**Figure 2.4:** Polar diagram of the scattering distribution generated by linearly polarised light of $\lambda = 550$ nm. As the radius of the particle $a$ approaches to the wavelength, the scattering field increases in the forward direction of the incident beam. From Born and Wolf [65].

incident wavelength ($I_s \propto 1/\lambda_0^4$), which is known as the *Rayleigh law*. For instance, photons of higher energy are first scattered when they travel through the atmosphere. This process is responsible for the blue colour of the sky which gives a direct evidence of the Rayleigh scattering of light.

## 2.3 Raman Scattering

Raman scattering is an inelastic process first observed in 1928 by the Indian physicist Raman [69]. Raman scattering originates from the light interaction with translational, vibrational and rotational modes (or optical phonons) of molecules. An incident photon is absorbed and subsequently emitted via an intermediate quantum vibrational state of the matter such that the remitted photons satisfy the energy and momentum conservation. Raman scattering is not a resonant effect such as in the case of fluorescence and therefore it can take place at any wavelengths of light. Vibrational modes of molecules range $10^{12} - 10^{14}$ Hz whilst rotational modes are usually an order of magnitude lower [70]. Since vibrational energy states of molecules are less populated at room temperature, the Stokes intensity often results to be greater than that of the Anti-Stokes [71].

Thanks to the ability to retrieve unique fingerprints about chemical compounds that structure matter, Raman spectroscopy has been widely employed to investigate and analyse a wide range of materials [72]. Over the past decades, Raman spectroscopy has also shown great potentials to be used as a feasible diagnostic tool for several diseases such as cancer [20, 73].

## 2.4 Spontaneous Brillouin Scattering

Spontaneous Brillouin scattering, first reported by Léon Brillouin in 1922 [21], arises when light is scattered by thermal density fluctuations propagating inside media. Local variations in the refractive index can be seen as a periodic Bragg grating traveling through matter at the hypersound velocity [56]. From a quantum mechanical point of view, Brillouin scattering is the result of the interaction between photons and acoustic phonons. These are defined as quanta of discrete energy levels holding the same particle-wave duality of photons and provide a quantitative representation of the inherent material excitation. As previously mentioned, the Doppler effect is responsible for the Stokes and the Anti-Stokes shift [74] depending on the direction of the momentum vector of the acoustic phonons with respect to that of the incident photons, as illustrated in Figure 2.5. In terms of the energy conservation, this means that an incident photon can either transfer energy to or acquire energy from the interaction with a phonon. Convention established the Stokes and the Anti-Stokes components to be associated with a negative and a positive frequency shift of the scattered radiation respectively [75].

In the following sections, two equations describing the frequency shift and the linewidth of the Brillouin spectrum are defined. The intensity ratio of the elastic and the inelastic scattered light, known as the *Landau-Placzek ratio*, is determined. Finally, a description of the material mechanical properties with a particular insight into the Brillouin elastic modulus is given.

### 2.4.1 Spectral Shift and Linewidth

For simplicity we consider the case of a Stokes process in which an electromagnetic field incident on a medium yields a scattered wave of lower frequency, as illustrated

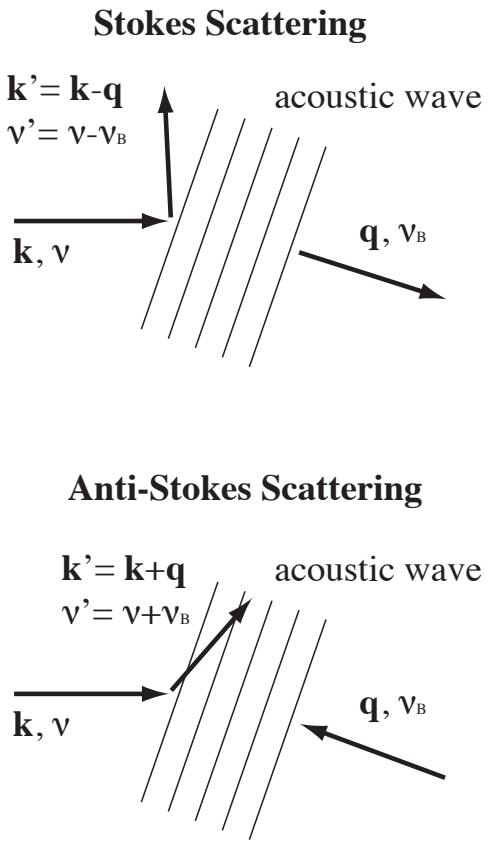



**Figure 2.5:** Stoke and Anti-Stoke frequency shifts diagram. The direction of the phonon wavevectors **q** is responsible for the frequency shift due to the Doppler effect. After [56].

in Figure 2.5. From a quantum mechanical point of view, this process sees the annihilation of a photon and the instantaneous generation of both a scattered photon and an acoustic phonon $q$, as dictated by the energy (E=$h\nu$) and the momentum ($\mathbf{p} = h\mathbf{k}$) conservation expressed as

$$\begin{aligned} \nu &= \nu' + \nu_B \\ \mathbf{k} &= \mathbf{k}' + \mathbf{q} \end{aligned} \tag{2.6}$$

where $\nu$, $\nu'$ and $\nu_B$ are the frequencies and $\mathbf{k}$, $\mathbf{k}'$, and $\mathbf{q}$ are the wavevectors of the incident and scattered photons and acoustic phonons respectively. A diagram of both the energy and momentum conservations is shown in Figure 2.6.

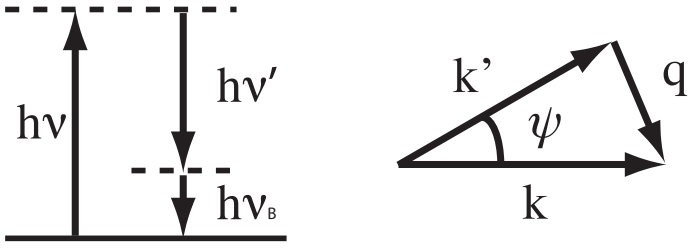



**Figure 2.6:** Energy (left) and momentum (right) conservation diagram. In the Stokes process the incident photon energy is conserved with the creation of a scattered photon and an acoustic phonon. The angle $\psi$ between incident and scattering wavevectors defines both the frequency shift and the spectral linewidth.

**Frequency Shift** Acoustic phonons travel in media at the adiabatic speed of sound $V$, also known as the hypersound velocity, and are characterised by a frequency $\nu_B$. Since the phonon frequency is several orders of magnitude lower compared to both the incident and scattered light frequencies [16], we can fairly assume that $\nu \approx \nu'$ and $|\mathbf{k}| \approx |\mathbf{k}'|$. Under this approximation we can define

$$\nu_B \equiv \frac{|\mathbf{q}|V}{2\pi}, \tag{2.7}$$

where the modulus of the phonon wavevector $\mathbf{q}$ is given by [76]

$$|\mathbf{q}| = \frac{4\pi n}{\lambda_0} \sin\left(\frac{\psi}{2}\right), \tag{2.8}$$

and $\psi$ is the scattering angle defined by the scalar product of the incident and scattering k-vectors

$$\psi = \cos^{-1}\left[\frac{\mathbf{k}\cdot\mathbf{k}'}{|\mathbf{k}||\mathbf{k}'|}\right]. \tag{2.9}$$

By combining equations 2.7 and 2.8 we finally obtain

$$\nu_B = \frac{2n}{\lambda_0} V \sin\left(\frac{\psi}{2}\right) \tag{2.10}$$

Equation 2.10 gives an analytical expression for the absolute frequency shift of the Brillouin spectral peaks with respect to the unshifted Rayleigh frequency. For $\psi = 0$

there is no shift in frequency whilst, for $\psi = 180°$, $\nu_B$ is maximised so that

$$\nu_B^{max} = \frac{2n}{\lambda_0} V \tag{2.11}$$

In this backscattering geometry, the Stokes shift is typically found within the range of $\nu_B \approx (1 - 50)$ GHz [77].

**Phonon Lifetime** Taking into account the quasi-particle nature of the acoustic phonons, it is possible to define the phonon lifetime as [71]

$$\tau_q = \frac{\rho_0}{\eta q^2} = \frac{\rho_0 \lambda_0^2}{16\pi^2 \eta n^2 \sin^2(\psi/2)}, \tag{2.12}$$

where $\rho$ and $\eta$ are the medium density and viscosity respectively. Equation 2.12 shows that for $\psi = 0$ the acoustic phonon lifetime is null, which gives a physical reason for the absence of Brillouin scattering in the forward direction. Conversely, $\tau_q$ and therefore $\nu_B$ are maximised for $\psi = 180°$. For a backscattering geometry in liquids, the lifetime has been found to be $\tau_q \approx 10^{-9}$ s [71]. Knowing that acoustic velocity $V$ is typically of the order of $V \sim 10^3$ m/s, it is possible to estimate the phonon propagation length to be of the order of $l_q = V\tau_q \approx 1\,\mu$m. This imposes a natural limit to the photon-phonon interaction length, which in turn sets a fundamental barrier on the achievable spatial resolution in Brillouin imaging, as discussed in Section 4.2.

**Linewidth** The short interaction period between the material excitation and the incident electromagnetic field leads to a finite spectral linewidth of the Brillouin scattered light, which is defined by [71]

$$\Delta\nu_B \equiv \frac{1}{2\pi\tau_q}. \tag{2.13}$$

Recalling Equation 2.12 we obtain

$$\Delta\nu_B = \frac{2\pi\Gamma\nu_B^2}{V^2}, \tag{2.14}$$

where $\Gamma = \eta/\rho$ is known as as the damping parameter. The full width at half maximum (FWHM) of the Brillouin peak can be further expressed in terms of the attenuation coefficient $\mu$ [52]

$$\Delta\nu_B = \frac{\mu V}{\pi}, \tag{2.15}$$

so that

$$\mu = \frac{2\Gamma\nu_B^2}{V}. \tag{2.16}$$

The natural linewidth of the Brillouin spectrum can therefore provide information about thermal relaxation processes and sound absorption in media, as demonstrated in previous analyses [78, 79].

### 2.4.2 Landau-Placzek Ratio

When considering the diffraction of light by weak sound waves in liquids, one can obtain the so called Landau-Placzek ratio defined as the ratio of the intensities of the Rayleigh and the Brillouin scattered light [80].

Einstein [81] and Smoluchowski [82] developed a theory for the isotropic light scattering by liquids using a statistical thermodynamics approach which describes the scattering process as due to local fluctuations in density. The intensity of the scattered radiation for a scattering volume element $V_s$ has been found to be proportional to the mean-square fluctuation $\langle(\Delta\epsilon)^2\rangle$ of the dielectric constant $\epsilon$ about its mean value [83]. For an incident monochromatic linearly polarised wave of electric field $\mathbf{E}$ perpendicular to the scattering plane, which is defined by the incident $\mathbf{k}_0$ and scattering $\mathbf{k}_s$ wave vectors, the scattered light intensity $I_s$ from each volume $V_s$ element is given by [84]

$$\frac{I_s}{I_0} = \frac{\pi^2}{r^2\lambda_0^4} V_s^2 \langle(\Delta\epsilon)^2\rangle, \tag{2.17}$$

where $I_0$ is the intensity of the incident beam. Assuming the fluctuations to be uncorrelated in subsequent volume elements, the total intensity of the scattered light would be therefore the sum of the intensities from each radiating electric dipole [84].

The Einstein-Smoluchowski approach to the problem was based on the choice of the dielectric constant as a function of both medium density $\rho$ and temperature $T$ ($\epsilon = \epsilon(\rho, T)$). Although this formulation gives an expression for the total scat-

tered intensity, it cannot separate the contribution of the central Rayleigh scattering $I_c$ from the Brillouin doublet $2I_B$. This limitation was overcome by Landau and Placzek thanks to a change in the thermodynamic variables. Expressing the dielectric constant as a function of two different independent variables, namely the non-propagating local entropy $S$ and pressure $P$ fluctuations in the liquid ($\epsilon = \epsilon(S, P)$), it was possible to derive an expression, known as the Landau-Placzek ratio, able to separate the two scattering intensities [84]. The Landau-Placzek ratio is generally expressed in the form

$$\frac{I_c}{2I_B} = \frac{C_P - C_V}{C_V}, \tag{2.18}$$

where $C_P$ and $C_V$ are the material heat capacities at constant pressure and volume respectively. Equation 2.18 is a good approximation for most liquids whilst for solids, where $C_P \approx C_V$, other non-negligible thermodynamic terms have to be included [85].

In the case of water of polarizability volume $\alpha_v = 1.45 \cdot 10^{-24}$ cm$^3$, and assuming a wavelength of $\lambda = 633$ nm and the observer distance from the scattering volume being $r = 1$ cm, simple calculations using equations 2.5 and 2.18 gave a factor of $10^{-8}$ for the intensity of the Brillouin scattered light with respect to that of the incident radiation ($I_0/2I_B \simeq 10^{-8}$). This estimate provides a quantitative perception of the weakness of the Brillouin scattering signal.

## 2.5 Mechanical Properties

Materials are characterised by mechanical properties describing their response to an applied force. The structure and composition of the material determine its response, which can be either elastic or inelastic. Figure 2.7 shows a typical stress-strain curve formed by an elastic and an inelastic region. The stress is defined as a force per unit area and can be of different types (e.g. shear, tensile, compressive) depending on the direction of the force vector with respect to the material. On the other hand, the strain is the material deformation defined as a change in size by unit length. An elastic strain is given when the deformation is linear with the applied stress. In other words, an elastic strain takes place instantaneously when a stress is applied and returns to its original state when the force is removed. Conversely, the strain is inelastic when it is non-linear with the stress, as illustrated in the graph. The extent

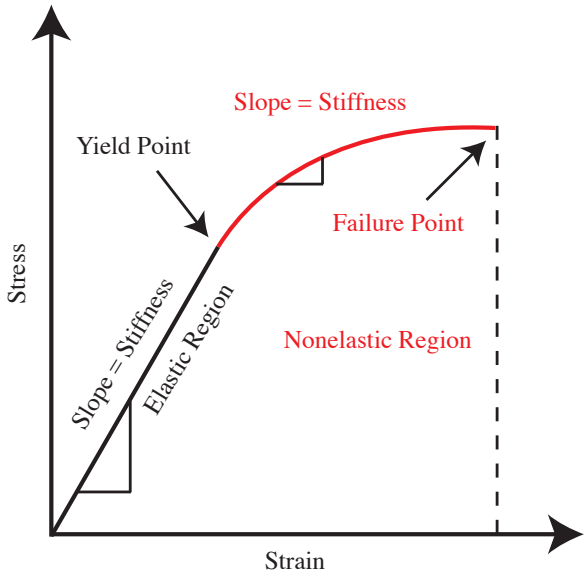



**Figure 2.7:** Typical stress-strain curve formed by an elastic and an inelastic region. The slope of the curve in the linear regime gives the stiffness of a material. After [86].

of the elastic region, where the stiffness is typically measured, mainly depends on the material structure. Rupture of the material occurs in the inelastic regime for an excessive amount of stress.

### 2.5.1 Elastic Moduli

The mechanical properties of materials are defined by several physical quantities that stem from the Hooke's Law [87]. Figure 2.8 shows a diagram of the longitudinal and shear stress associated with the Young's modulus ($E$) and the shear modulus ($G$). The Young's modulus is the ratio of the tensile (or compressive) stress and strain in

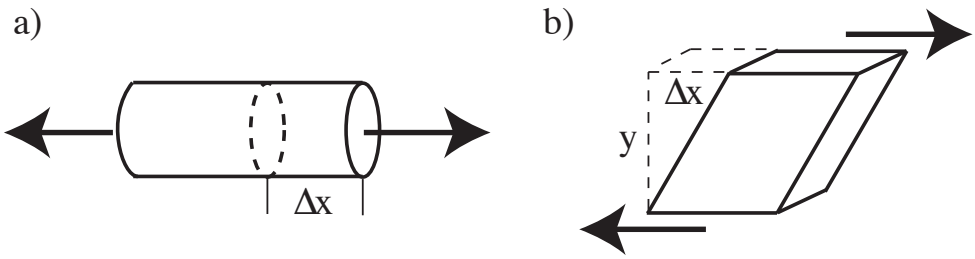



**Figure 2.8:** Diagram of the longitudinal tensile stress a) and the shear stress b). The ratio of the stress and the strain gives the Young's and shear moduli.

the linear regime and defines the stiffness of a material. The steeper the slope, the higher the stress required to separate the atoms and stretch the material. Young's modulus derived in SI unit is expressed in Pascal (Pa). Similarly, the shear modulus is defined as the slope of the shear stress-strain curve in the linear region. Specifically, the shear modulus describes a material response when the strains perpendicular to the stress direction are zero, i.e. when a material is subject to shape deformation without affecting its volume. In the inelastic regime, the stiffness is given by the slope of the tangent at each point of the stress-strain curve.

As previously mentioned, standard methods to measure stiffness analyse the response of materials under uniform compressive loads, which make them invasive. Conversely, spontaneous Brillouin light scattering provides the unique opportunity to investigate the mechanical properties of materials in a non-invasive manner. A beam is used as a probe and the spectrum of the scattered light arising from the interaction with longitudinal and shear acoustic waves contains fundamental information about the elasticity of the material investigated. Since shear transverse acoustic waves of isotropic materials are silent in the backscattering geometry ($\psi = 180°$) [54], the research conducted was mainly focused on the analysis of the spectrum arising from longitudinal acoustic waves. In this case, the Brillouin frequency shift $\nu_B$ and the spectral linewidth $\Delta\nu_B$ are associated with the longitudinal modulus $M$, which is defined as the ratio of axial stress to axial strain and differs from the standard Young's modulus due to the strict uniaxial state of material perturbation generated by the longitudinal acoustic waves. In other words, the uniaxial perturbation yields a longitudinal strain without formation of a shear strain.

Biological specimens have similar mechanical properties to those of viscoelastic materials [88], whose response to an applied stress force is typically characterised by a fast deformation followed by a slow return to the original state. In particular, viscoelastic materials show both elastic and viscous properties resulting in a time-dependent strain. The complex longitudinal modulus $M$ of a viscoelastic medium can be derived from the differential equation describing the propagation of a longitudinal acoustic wave in that medium [88] and is expressed as

$$M = M' + iM'' = \rho V^2 + i(\rho V^3 \mu / \pi \nu_B), \tag{2.19}$$

whence

$$M' = \rho V^2 \tag{2.20}$$

and

$$M'' = \frac{\rho V^2 \Delta\nu_B}{\nu_B}. \tag{2.21}$$

The real part $M'$ of the longitudinal bulk modulus is referred as the *storage modulus* and describes the elastic response, whilst the complex part $M''$ known as the *loss modulus* is associated with the viscous response of the vicoelastic material. Considering the case of a backscattering geometry and recalling equation 2.10, we obtain

$$M' = \rho \left( \frac{\nu_B \lambda_0}{2n} \right)^2, \tag{2.22}$$

which gives an analytical expression relating the longitudinal storage modulus, which we refer as the Brillouin modulus, with the Brillouin frequency shift.

Despite the similarity, the Brillouin longitudinal modulus $M'$ has been found to have greater values compared to the conventional Young's modulus. In fact, longitudinal acoustic waves act as rapid and unidirectional oscillating stresses and slow relaxation processes are not fast enough to respond to the GHz acoustic modulation [54].

The Brillouin modulus can be further expressed in terms of the bulk modulus $K$ and the shear modulus $G$ [89]

$$M' = K + \frac{4}{3}G, \tag{2.23}$$

where the bulk modulus $K$ measures a substance variation in volume as a response to a uniform applied pressure such as a uniform load [90]. The bulk modulus $K$ is related to the Young's modulus $E$ through the equation [91]

$$K = \frac{E}{3(1-2\sigma)}, \tag{2.24}$$

where $\sigma$ is known as the Poisson's ratio defining the compressibility of materials. A medium tends to expand orthogonally with respect to the direction of compression, as shown in Figure 2.9, and the Poisson's ratio gives a measure of the amount of

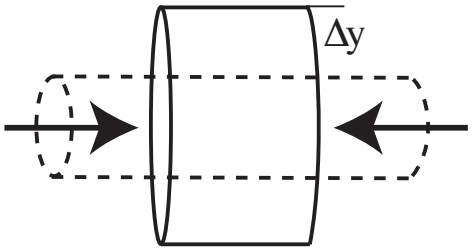



**Figure 2.9:** Diagram of the compressive stress and the resulting orthogonal strain. The Poisson's ratio measures the material expansion to an applied compression.

orthogonal expansion with respect to the compression applied to the medium. For this reason, in the case of low viscosity media such as in liquids, $\sigma$ is generally very close to a value of 0.5 [31]. On the other hand, most metals have compressibility of $\sigma \approx 1/3$ so that $K \approx E$. By combining equation 2.23 and 2.24 we obtain

$$M' = \frac{4}{3}\left[\frac{E}{4(1-2\sigma)} + G\right], \tag{2.25}$$

which shows that the liquid incompressibility is responsible for the large difference between Brillouin and Young's moduli in materials of high water content, such as biological samples. Nevertheless, recent analyses [54] have empirically found a log-log linear relationship between Brillouin and Young's moduli, which can be expressed as

$$\log(M') = a\log(E) + b, \tag{2.26}$$

where $a$ and $b$ are two arbitrary coefficients. This relationship has been demonstrated by measuring the stiffness of bovine lenses at different ages with conventional compressive stress-strain methods and fitting the resulting values with those obtained from the Brillouin shift. The linear correlation, further validated by our experimental results illustrated in Section 5.1, endorses Brillouin spectroscopy as a reliable method to measure stiffness.

# Chapter 3

# Multiple Beam Interference

The small frequency shift ($1 - 50$ GHz) of the Brillouin doublet from the central Rayleigh peak imposes a spectral resolution $\delta\nu < 1$ GHz and a resolving power $\mathcal{R} > 10^6$, which standard spectrometers are not able to achieve [37, 38]. Besides multipass diffraction grating monochromators [92, 93, 94] and heterodyne light beating methods [95, 96, 97], Fabry-Pérot interferometers have been mainly engaged in Brillouin spectroscopy thanks to the high angular dispersion [39, 40]. Since the release of piezoelectric stages, the spectrum has been commonly acquired by scanning the optical cavity of the Fabry-Pérot interferometer and collected by means of single channel detectors such as high-sensitivity photodiodes and photomultipliers [37, 40, 41]. The development of new high-sensitivity multichannel detectors (e.g. CCD and photodiode arrays) has allowed it to operate in a faster nonscanning mode using fixed cavity length FP etalons [42, 43, 44]. Furthermore, the general requirement of maintaining a sensible parallelism of $\lambda/100$ or higher during the scanning process with a conventional FP interferometer has been overcome [45, 46]. In fact, whilst a Fabry-Pérot is an empty cavity constructed from two highly reflective mirrors translating in the axial direction, an etalon is a device typically made of either glass or silica to ensure high parallelism between the two dielectric coated surfaces.

In the following sections, the principles governing FP interferometers are described and extended to the case of a VIPA etalon. The longitudinal modes of a He-Ne laser are investigated to calibrate the etalon. A two-stage VIPA spectrometer

developed in our laboratory is described.

## 3.1 Fabry-Pérot Interferometer

A Fabry-Pérot interferometer is made out of two highly reflecting surfaces parallel to each other. We shall define $r$ and $t$ as the complex amplitude reflection and transmission coefficients of an incident beam traveling at an angle $\theta$ with respect to the surface normal, so that for an ideal lossless system

$$|r|^2 + |t|^2 = 1. \tag{3.1}$$

When the incident beam travels through the FP cavity, light gets partially transmitted and reflected through both surfaces. The phase delay $\delta$ of the beam after a full pass (i.e. a double reflection) inside the cavity is given by [98]

$$\delta = \frac{2\pi n d \cos\theta}{\lambda} = \frac{2\pi n d \cos\theta \nu}{c}, \tag{3.2}$$

where $n$ is the refractive index of the interferometer and $d$ is the distance between the two surfaces. Figure 3.1 shows a diagram of a FP illustrating the transmission and reflection fields for several passes. Assuming that $t$ and $r$ are equal for both

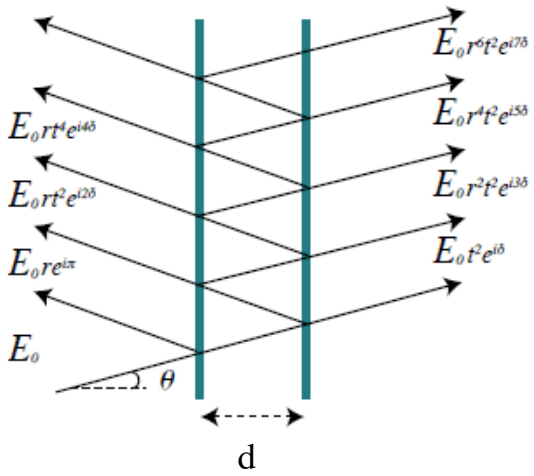



**Figure 3.1:** Transmission and reflection fields of a Fabry-P´erot interferometer.

surfaces, the sum of all the transmitted fields gives the total transmitted amplitude

$$\begin{aligned} E &= E_0 \left[ t^2 e^{i\delta} + r^2 t^2 e^{i3\delta} + r^4 t^2 e^{i5\delta} + ... \right] \\ &= E_0 T e^{i\delta} \sum_{j=1}^{N} R^m e^{i2\delta j} \\ &= E_0 \frac{T e^{i\delta}}{1 - R e^{2i\delta}} \end{aligned} \tag{3.3}$$

from which we obtain the function describing the total transmitted intensity distribution

$$\frac{I}{I_0} = \left| \frac{E}{E_0} \right|^2 = \frac{(1-R)^2}{|1 - R e^{2i\delta}|^2} = \frac{(1-R)^2}{1 + R^2 - 2R\cos 2\delta}, \tag{3.4}$$

where $R = |r|^2$ and $T = |t|^2$ are the reflection and transmission intensity coefficients, respectively. By recalling simple trigonometric identities, we can rewrite equation 3.4 as follow

$$\frac{I}{I_0} = \frac{1}{1 + F \sin^2 \delta}, \tag{3.5}$$

where

$$F = \frac{4R}{(1-R)^2}. \tag{3.6}$$

Equation 3.5 is known as the *Airy function* and describes the intensity profile of the total transmitted field of a Fabry-Pérot interferometer. Figure 3.2 illustrates the intensity distribution of a FP as a function of frequency. Constructive interference only occurs at certain angles leading to *Haidinger fringes of equal inclination*, and therefore to a ring pattern in the far field. Maxima of the Airy function, i.e. when $I/I_0 = 1$, occur for

$$\delta = m\pi \qquad\qquad |m| = 0, 1, 2, .. \tag{3.7}$$

where $m$ is an integer indicating the interference order. The *free spectral range* (FSR) of a FP is defined as the change in frequency $\Delta\nu$ required to vary the phase $\delta$ by $\pi$. Consequently, by imposing $\delta = \pi$ in equation 3.2 it follows that

$$\Delta\nu = \frac{c}{2nd\cos\theta}, \tag{3.8}$$

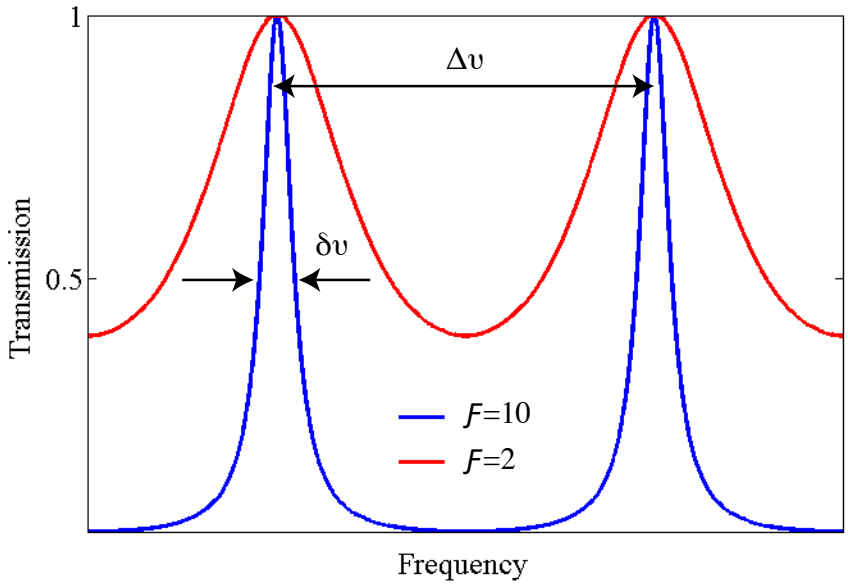



**Figure 3.2:** Normalised Airy functions of a Fabry-Pérot for different finesse $\mathcal{F}$ values. The peak separation $\Delta\nu$ and the linewidth $\delta\nu$ define the FP free spectral range and the spectral resolution, respectively.

or in terms of the optical wavelength

$$\Delta\lambda = \frac{\Delta\nu\lambda^2}{c} = \frac{\lambda^2}{2nd\cos\theta}. \tag{3.9}$$

Furthermore, the transmission drops to one half for $F\sin^2\delta = 1$, so that

$$\delta \approx m\pi \pm \frac{1}{\sqrt{F}}. \tag{3.10}$$

From this condition we have that the FWHM of the transmission peaks is given by

$$\Delta\delta = \frac{2}{\sqrt{F}} = \frac{1-R}{\sqrt{R}}. \tag{3.11}$$

The *finesse* $\mathcal{F}$ of a Fabry-Pérot is defined as the ratio of the FSR associated with the spacing between adjacent fringes, and the FWHM [99]

$$\mathcal{F} = \frac{\pi}{\Delta\delta} = \frac{\pi\sqrt{R}}{1-R}. \tag{3.12}$$

In other words, $\mathcal{F}$ is a measure of the number of total beam passes that occur inside the FP cavity. Figure 3.2 shows how the FP intensity profile varies for different values of the finesse.

We can further define the spectral resolution as the ratio of the free spectral range and the finesse

$$\delta\nu = \frac{\Delta\nu}{\mathcal{F}}. \tag{3.13}$$

The higher the finesse the greater the spectral resolution, which is typically of the order of hundreds MHz [99]. Despite the high spectral resolution, the FP has a relatively small FSR compared to other devices, such as diffraction gratings, which on the other hand are typically limited by a low resolution power ($\delta\nu \sim 10{-}100$ GHz) [99, 100].

## 3.2 Virtually Imaged Phased Array (VIPA)

Despite the high spectral resolution, both scanning and non-scanning FP interferometers are fundamentally limited by a maximum throughput efficiency, the magnitude of $1/\mathcal{F}$ [52]. Consequently, the high finesse demand in Brillouin spectroscopy has typically limited the transmission of the input signal to be less than 1%, therefore leading to long data acquisition times. Up to several hours have been required to acquire a single spectrum [101, 102]. Diffraction grating monochromators, on the other hand, can provide a throughput efficiency of up to 25% [93, 94]. Nevertheless, the scanning process involved in the data acquisition is slow as they measure the spectral contents sequentially [52].

In order to overcome the long data acquisition times and simultaneously maintain a high spectral resolution, a novel type of the Fabry-Pérot etalon, named Virtually Imaged Phased Array, has been developed to enable minimal insertion losses, therefore allowing fast detection of the interference pattern. This name is due to the similarity of the device's operation with that of a series of multiple virtual sources interfering with each other as in a phased array [48]. The VIPA is an interference device based on a totally and a partially reflective coated layer placed parallel to each other with the addition of an AR coated entrance window on one side. The AR entrance window consists of a $R < 0.1\%$ reflective surface that maximises the

amount of input radiation incident at a small angle $\theta$ [50]. Figure 3.3 shows the schematic diagram of a VIPA spectrometer. Both parallel surfaces have high reflec-

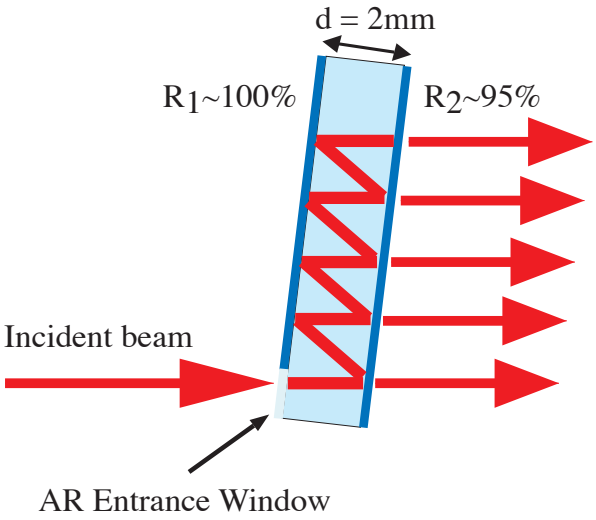



**Figure 3.3:** Basic diagram of a VIPA etalon. The input beam enters at a certain angle through the AR coated window and undergoes multiple reflections inside the cavity as in a normal FP etalon.

tivity in order to obtain a high finesse. Nevertheless, the first VIPA surface (where the entrance window is located) has typically $R_1 > 99.9\% > R_2$ so that light does not exit in the backwards direction. This allows both finesse and throughput efficiency to be maximised. Considering the VIPA as a phased array, the output beam direction can be determined by the phase difference introduced by the single array elements, i.e. the phase difference between each subsequential "virtual source" [49]. Besides the optical path difference, the phase shift is wavelength dependent making the VIPA a highly angular dispersive device. The principles of multiple beam interference that govern the VIPA are equal to those derived for a normal Fabry-Pérot interferometer. The output intensity distribution of a VIPA is therefore described by the Airy function, which is illustrated in Figure 3.2.

### 3.2.1 Optical Arrangement

The optical arrangement that employs the VIPA as a high efficiency spectrometer is shown in Figure 3.4. An incident collimated beam is focused by a cylindrical

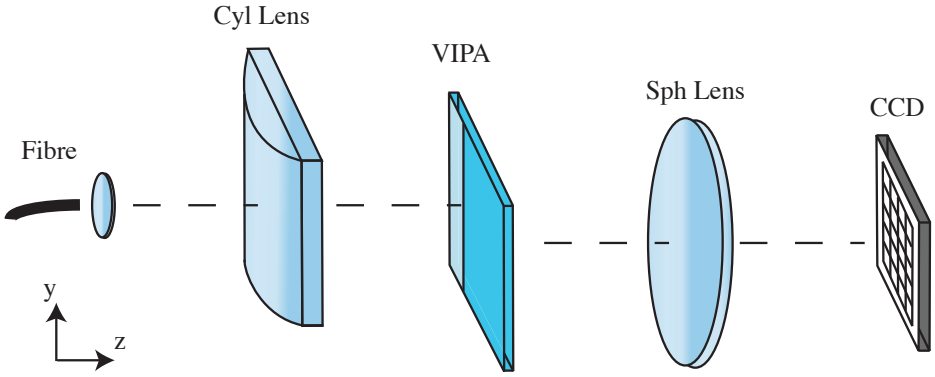



**Figure 3.4:** Diagram of the optical arrangement of a VIPA spectrometer. The scattered radiation delivered by a single-mode fibre is first collimated and then focused by a cylindrical lens to the VIPA entrance window. A spherical lens translates the spectral content into a spatial domain. The spectrum is recorded by a CCD camera allowing fast data acquisition.

lens to the entrance window of the VIPA. The output field of the etalon is Fourier transformed by a spherical lens so as to spatially disperse the spectral content of the scattered light. A multichannel array detector (e.g. a CCD camera) acquires the resulting fringe pattern where lines of different frequencies are spatially separated.

### 3.2.2 VIPA Illumination

The finite angle of convergence of the focused beam given by the cylindrical lens defines the illumination window of a specific region of the fringe pattern. In fact, the intensity profile that is formed at the detector plane is the product of the intensity distribution of the incident beam and the etalon Airy function. In an ideal scenario, the resulting spectral pattern is therefore made of straight fringes whose total intensity is distributed over a Gaussian envelope defined by the incident beam. In order to illustrate this principle, Figure 3.5 shows a simulation of the resulting spectral pattern given by the product of the Airy function and a Gaussian profile imposed by the incident beam converging at an arbitrary angle $\alpha$.

We want to confine the illumination within a single FSR unit of the VIPA, such that the intensity of the Brillouin peaks contained in that spectral region can be maximised. As a result, a shorter data acquisition time can be obtained. This

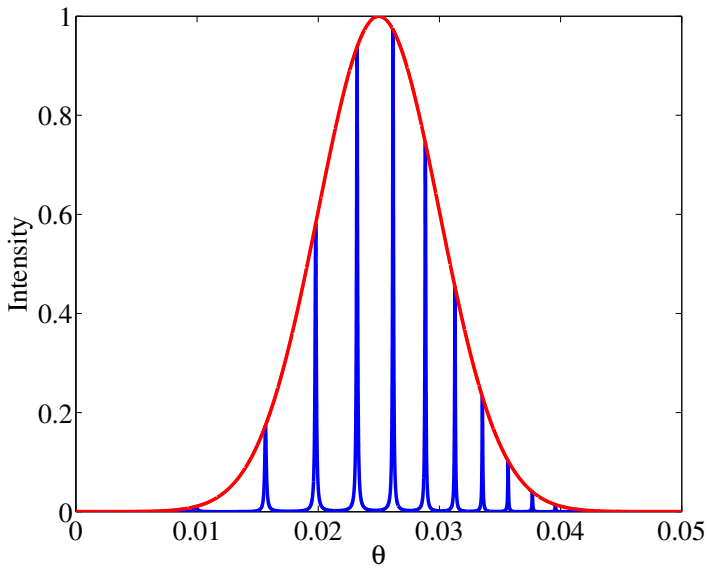



**Figure 3.5:** Angular intensity distribution at the VIPA Fourier plane. The straight fringes (blue) are confined in a Gaussian envelope (red) defined by the convergence angle of the focused beam. The strength of the Brillouin signal is maximised when the Gaussian encloses only two subsequent orders.

condition can be satisfied when the beam convergence $\alpha$ is

$$\alpha \geq \frac{1}{2}\sqrt{\frac{\lambda}{nd}}, \tag{3.14}$$

as illustrated in Appendix A. Given a certain beam size at the cylindrical lens, the condition for the beam convergence in turn sets the focal length to use for the VIPA illumination, as further discussed in Section 3.3.2.

### 3.2.3 Finesse Optimisation

Both beam convergence and angle of incidence define the number of full optical passes that take place inside the VIPA cavity. Given the relationship between the number of beam reflections inside the cavity $N_c$ and the finesse [103]

$$N_c \simeq \pi\mathcal{F}, \tag{3.15}$$

we need to find the minimum angle of incidence $\theta_0$ that maximises $N_c$, therefore providing the highest finesse.

Before proceeding with the analysis, a preliminary investigation regarding the location of the *beam waist*, defined as the beam radius at the focal plane, is necessary. In particular, we need to find the axial position of the VIPA with respect to the focal plane of the cylindrical lens that would provide the minimum angle of incidence $\theta_0$. Figure 3.6 shows diagrams of the incident Gaussian beam along the focal region, where the beam waist $w_0$ located at $z = 0$ is defined by [99]

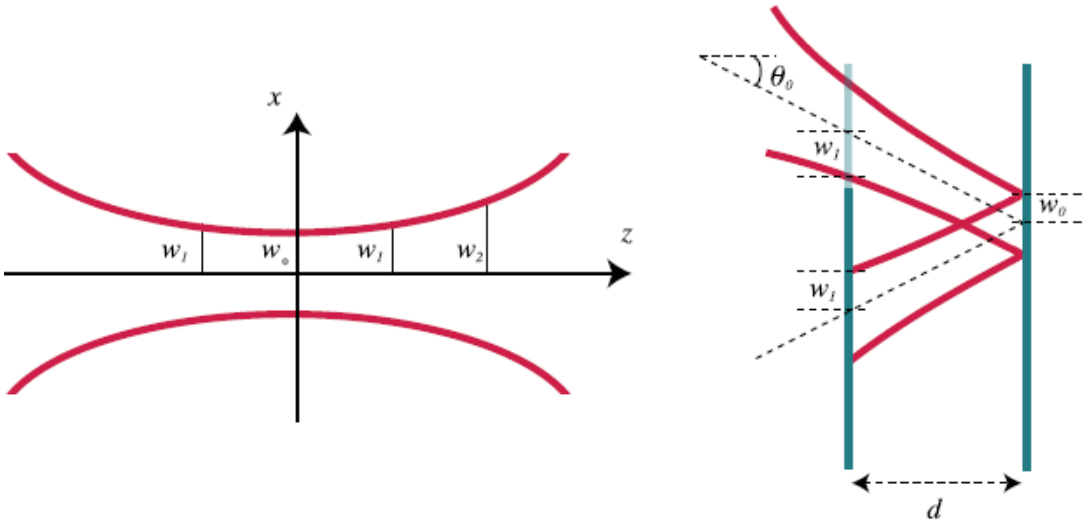



**Figure 3.6:** Gaussian beam convergence along the focal region (left) and at the VIPA entrance window (right). Refraction was neglected assuming a small angle of incidence $\theta_0$. The beam waist $w_0$ is defined at $z = 0$. Adjacent radii ($w_1$ and $w_2$) are located at a distance $d$ with each other. In order to minimise $\theta_0$, the sum of the beam radii at the first VIPA surface needs to be minimum.

$$w_0 = \frac{\lambda}{\pi\alpha}. \tag{3.16}$$

Simple geometrical evaluations dictate that the smallest angle of incidence is given when the sum of the beam radii at the first VIPA surface before and after the first reflection is minimum. Consequently, we need to establish whether $w_0$ needs to be located either at the first or at the second surface of the VIPA. Adjacent reference radii $w_1$ and $w_2$ are considered for $z = d$ and $z = 2d$, respectively, where $d$ is the

VIPA thickness. The beam radius as a function of $z$ is given by [99]

$$w(z) = w_0 \sqrt{1 + \frac{z^2}{z_0^2}}, \tag{3.17}$$

where $z_0$ is known as the *Rayleigh range* defined as the distance from the waist at which the spot size has grown by $\sqrt{2}$, i.e. when $w(z_0) = \sqrt{2}w_0$. The Rayleigh range is expressed as

$$z_0 = \frac{\pi w_0^2}{\lambda}. \tag{3.18}$$

If the beam waist were located at the VIPA entrance window we would have that after one reflection the beam radius at the first surface was $w_2 = w(2d)$. The sum of the two radii $w_0$ and $w_2$ is thus given by

$$w_0 + w(2d) = w_0 \left[ 1 + \sqrt{1 + \frac{4d^2}{z_0^2}} \right], \tag{3.19}$$

On the other hand, if the beam waist were located at the second surface we would have beam radii of equal size $w_1 = w(d)$, so that

$$2w(d) = 2w_0 \sqrt{1 + \frac{d^2}{z_0^2}}. \tag{3.20}$$

Since $2w(d) < w_0 + w(2d)$, it follows that in order to minimise the entrance angle $\theta_0$, the beam waist needs to be located at the second surface of the VIPA. Furthermore, by combining equation 3.18 and 3.16 and by imposing the condition for the beam convergence expressed in equation 3.14 we have that the Rayleigh range reduces to

$$z_0 = \frac{4nd}{\pi} \simeq 2d. \tag{3.21}$$

Since the depth of field given by the cylindrical lens is larger compared to the VIPA thickness, equation 3.21 suggests that the alignment of the VIPA with respect to the beam waist allows a certain degree of flexibility without a significant decrease in the finesse.

In order to estimate the minimum angle of incident $\theta_0$, we can start by referring to the diagram in Figure 3.7. In particular, we need to impose that the distance $\Delta x_0$

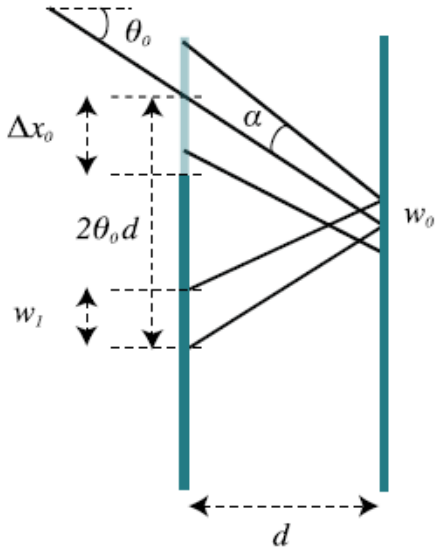



**Figure 3.7:** Ray tracing diagram of a beam incident at an angle $\theta_0$ with convergence $\alpha$. The beam waist is located at the second surface of the VIPA. The beam radius at the first surface after one reflection is given by $w_1 = w(d)$.

between the edge of the AR coated surface and the centre of the Gaussian beam cannot be smaller than the beam radius $w_1 = w(d)$ so that

$$\Delta x_0 \geq C w_1, \tag{3.22}$$

where C is a factor that takes into account both the tail of the intensity distribution of the Gaussian beam and a small region of transition from the AR to the HR coated surfaces of the VIPA. In fact, manufacturing processes inevitably lead to coating imperfections that result in a small gradient from the HR to the AR coated surfaces. This region of transition can be of the order of tens of microns and therefore it needs to be taken into account to avoid beam clipping. From simple geometrical rays tracing considerations, we have

$$2\theta_0 d - C w_1 \geq C w_1, \tag{3.23}$$

which leads to

$$\theta_0 \geq \frac{C w(d)}{d} = \frac{C w_0}{d}\sqrt{1 + \frac{d^2}{z_0^2}}. \tag{3.24}$$

If we further impose the condition on the beam convergence expressed in equation 3.14 to the beam waist we obtain

$$w_0 = \frac{2}{\pi}\sqrt{\lambda n d}. \tag{3.25}$$

By substituting equations 3.21 and 3.25 into equation 3.24 we finally obtain

$$\theta_0 \geq \frac{2C}{\pi}\sqrt{\frac{n\lambda}{d}\left[1 + \left(\frac{\pi}{4n}\right)^2\right]}. \tag{3.26}$$

Equation 3.26 gives the condition for the minimal angle of incidence $\theta_0$, which is critical in achieving both minimal insertion losses and the highest finesse, thus the highest spectral resolution.

### 3.2.4 Laser Longitudinal Modes

Laser radiation is well known to be not perfectly monochromatic [99, 104, 105]. The range of frequencies over which lasing can occur is ultimately determined by the energy transitions allowed by the gain medium. The characteristic linewidth due to the uncertainty on the energy transitions responsible for the emission is also subject to a broadening by a variety of mechanisms. In a gas laser such as He-Ne this is predominantly caused by random thermal motions of atoms leading to Doppler frequency shifting. This type of broadening is known as inhomogeneous broadening. The energy distribution in a He-Ne gain medium is of the Maxwell-Boltzmann type yielding a Gaussian lineshape with a FWHM of [99]

$$\Delta\nu_D = \nu_0\sqrt{\frac{8k_B T \ln 2}{Mc^2}}, \tag{3.27}$$

where $\nu_0$ is the central frequency, $k_B$ the Boltzmann's constant, $T$ the absolute temperature and $Mc^2$ the invariant mass of the gas atoms. For a He-Ne laser of central wavelength $\lambda_0 = 632.8$ nm, assuming $T \backsimeq 400$ K and $Mc^2 \backsimeq 3.2 \times 10^{-9}$ J, we have that $\Delta\nu_D \backsimeq 1.55$ GHz.

Besides the intrinsic linewidth due to the gain medium, the lasing frequency is further affected by the the laser cavity. This is typically constructed from two

highly reflective and parallel or concave mirrors forming a resonator. The laser resonant cavity structure gives rise to different transverse and longitudinal modes and therefore to multiple resonant frequencies allowed by the condition [105]

$$\nu_{m',n',q'} = \frac{c}{2L}\left(q' + \frac{1}{\pi}(m' + n' + 1)\arccos\sqrt{g_1 g_2}\right), \tag{3.28}$$

where the $m'$ and $n'$ are integers representing the transverse mode numbers, $q'$ the longitudinal mode number and

$$g_{1,2} = 1 - \frac{L}{R_{1,2}} \tag{3.29}$$

is a parameter defining the stability of the cavity depending on the cavity length $L$ and the mirrors radius of curvature $R$. Figure 3.8 gives a typical spectral diagram of the longitudinal modes arising in a HeNe laser. Assuming a perfectly stable laser

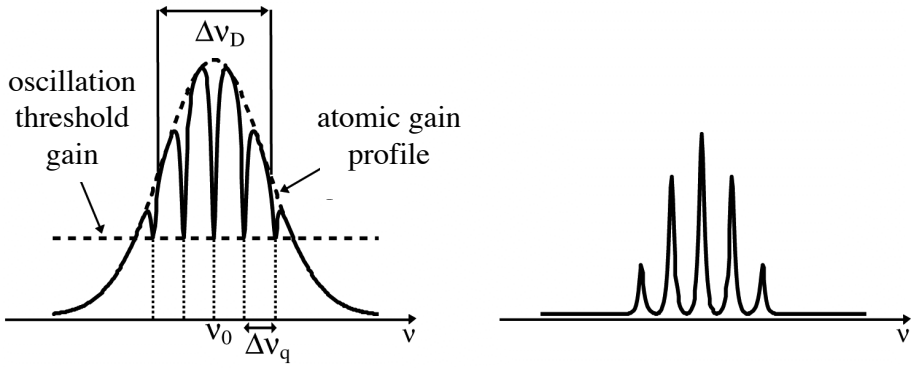



**Figure 3.8:** Multiple simultaneously oscillating longitudinal modes in a HeNe laser cavity. After [104].

cavity, that is when

$$\sqrt{g_1 g_2} = 1, \tag{3.30}$$

we obtain

$$\Delta\nu_{q'} = \nu_{q'+1} - \nu_{q'} = \frac{c}{2L}, \tag{3.31}$$

which gives the separation between the laser longitudinal modes.

### 3.2.5 VIPA Calibration

The narrow spectral lines produced by the laser radiation were considered suitable for the experimental characterisation of the VIPA. A previous analysis [106] has used a VIPA in conjunction with a diffraction grating to generate a high-resolution dispersion device able to separate the individual modes of a stabilised frequency comb laser into a two-dimensional array. A *Uniphase* HeNe laser with cavity length of $L = (418 \pm 2)$ mm emitting

$$\frac{\Delta\nu_D}{\Delta\nu_{q'}} = 4 \pm 1 \tag{3.32}$$

longitudinal modes equally spaced by $\Delta\nu_{q'} = (320 \pm 10)$ MHz was used. The laser beam was focused by a cylindrical lens to a solid silica VIPA etalon characterised by an optical thickness of $d = (8 \pm 0.5)$ mm, a length of $l = (23 \pm 0.5)$ mm and two HR coated surfaces of reflectivity $R_1 = 98\% \pm 1\%$ and $R_2 = 95\% \pm 1\%$ at $\lambda = 633$ nm. Assuming a normal angle of incidence $\theta = 0$ and the refractive index of silica $n = 1.47$, from equation 3.8 we have a theoretical free spectral range of $\Delta\nu = (12.8 \pm 0.5)$ GHz. Furthermore, considering an average reflectivity of $R = 97\% \pm 1\%$ and assuming the surfaces to be perfectly parallel and flat we obtain a theoretical finesse of $\mathcal{F} \simeq 103 \pm 5$ and therefore a spectral resolution of $\delta\nu = \Delta\nu/\mathcal{F} \simeq 12.5$ MHz and a resolving power of $\nu/\delta\nu \simeq 3.8 \times 10^7$.

During the alignment of the system, particular attention was paid to avoid beam clipping at the AR-HR interface to avoid formation of ghost patterns interfering at the detector plane. In order to ensure minimal insertion losses, the alignment was accomplished by looking at low interference orders and gradually decreasing the inclination angle of the VIPA to finally approach to the highest orders with the maximum output intensity. The resulting interference fringes formed at the Fourier plane of a diffraction-limited doublet were collected using a *Starlight Xpress Trius* CCD camera.

The 4 laser longitudinal modes were clearly resolved by the VIPA, as shown in Figure 3.9. A linescan was performed across the resulting straight fringes over one FSR. The resulting intensity plot shows a lower intensity for the higher interference order as a result of the Gaussian illumination envelope centered to the lower order. This acquisition allowed to estimate the finesse of the VIPA from experimental data

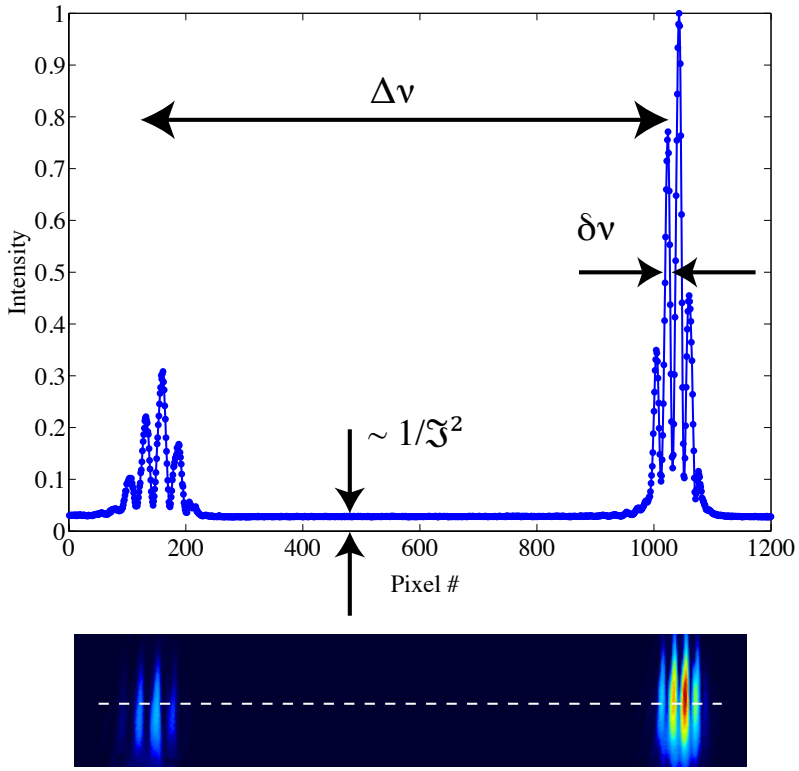



**Figure 3.9:** Normalised intensity profile as a function of the pixels number (top) obtained from a linescan (white dotted line) across the interference fringes shown in the bottom false coloured image. Blue dots are the experimental data.

as

$$\mathcal{F} = \frac{\Delta\nu}{\delta\nu} = 55.2 \pm 1.7, \tag{3.33}$$

where the error was due to the uncertainty on the number of pixels counted on the dispersion axis. The experimental finesse value was significantly lower than the theoretical one. This is not surprising as the manufacturing defects affecting both parallelism and flatness of the VIPA surfaces, which are typically required to exceed the order of $\lambda/100$, significantly decreases the resolution of the spectrometer [43, 107, 108].

A different approach to estimate the finesse was taken by measuring the intensity minimum $I_{min}$ of the interference pattern after subtraction of the camera background. By imposing $\delta = \pi/2$ on the Airy function, an expression for the

finesse as a function of $I_{min}$ can be obtained

$$\mathcal{F} = \frac{\pi\sqrt{F}}{2} = \frac{\pi}{2}\sqrt{\frac{1}{(I_{min}/I_0)} - 1}\,. \tag{3.34}$$

From equation 3.34 the finesse was estimated $\mathcal{F} = 57.8 \pm 1.9$, which is in good agreement with the previous measurement. Furthermore, by taking into account the average experimental finesse $\mathcal{F} = 56.5 \pm 2.3$ and the theoretical FSR, we estimated a spectral resolution of $\delta\nu = \Delta\nu/\mathcal{F} = (227.3 \pm 8.7)$ MHz.

Overall, the investigation on the spectral lines of a HeNe laser gave encouraging results motivating the employment of the VIPA in the design of a high resolution spectrometer suitable to resolve the Brillouin spectra.

## 3.3 Multistage VIPA etalons

A single VIPA setup, such as that illustrated in Figure 3.4, enables sub-GHz spectral resolution with minimal insertion losses. This allows the Brillouin spectral peaks of mostly transparent samples, such as liquids, to be localised and resolved from the central elastic peak. However, spectral analyses on turbid materials, such as biological specimens, might be compromised by a central Rayleigh peak which can be many orders of magnitudes greater than the adjacent Brillouin satellites. In this scenario, the spectral contrast, also known as the *extinction* of the spectrometer, becomes a key parameter. The extinction is defined as the ratio of the maximum to the minimum intensity transmitted by the spectrometer. Since the intensity transmission of the etalon is described by the Airy function, the spectral contrast can be expressed as a function of the finesse [43]

$$C = \frac{I_{max}}{I_{min}} = 1 + \frac{4\mathcal{F}^2}{\pi^2}. \tag{3.35}$$

A poor extinction results in the formation of a crosstalk between adjacent fringes due to the multiple beam scattering by surface imperfections of the VIPA. Strong crosstalks can eventually overwhelm the weak Brillouin peaks, therefore affecting the localisation accuracy at detection.

The strength of the light scattered by biological tissues is similar to that arising from intralipid solutions at concentration between 1% and 10% [51]. A single VIPA typically has an extinction of less than 30 dB. This impedes the detection of the Brillouin doublet even at minimal intralipid concentration, e.g. at concentration $10^{-7}$ %. In fact, above this level the Brillouin signal is completely overcome by the crosstalk. Spectrometers formed by multiple VIPA etalons mounted in tandem have been recently shown to achieve an extinction ratio of up to 80 dB [51, 54] making them suitable to retrieve and resolve the spectrum of highly scattering biological samples. The following sections describe the principle of cross-axis cascading with VIPA etalons and the realisation of a two-stage VIPA spectrometer whose extinction reaches up to 60 dB.

### 3.3.1 Cross-axis Cascading of Spectral Dispersion

The basic concept behind cross-axis multistage etalons is based on the rotational displacement of the dispersion axis with respect to the lines where the crosstalk arises. The dispersion axis of a spectrometer is defined in the spatial domain as the direction where the inelastic light spreads. The cross-axis cascading principle has been previously applied in the case of a double grating spectrometer where a 45°-tilted Dove prism was used to rotate the beam dispersion between the two diffraction gratings [109] resulting in an extinction of 75 dB. Nonetheless, conventional diffraction gratings are typically limited by a poor spectral resolution (usually of the order of 0.1 nm) and a slow data acquisition time, which make them unsuitable to perform spectral analysis of the Brillouin scattered light.

We applied the cross-axis cascading principle to design a more efficient multiple stage VIPA spectrometer. Figure 3.10 illustrates the cross-axis cascading dispersion in the case of both a single and a double stage VIPA. For a single VIPA, both Brillouin doublet and crosstalk arise along the same axis. Consequently, when the ratio of the Rayleigh to the Brillouin peak intensity is greater than the spectral contrast, both Stokes and Anti-Stokes peaks are overwhelmed by the stray light. Conversely, in the case of two VIPAs of equal dispersion power crossed with each other, the dispersion axis is rotated by 45° from the original $\hat{x}$ axis defined by the first VIPA, therefore lying on a diagonal direction with respect to the crosstalk formed

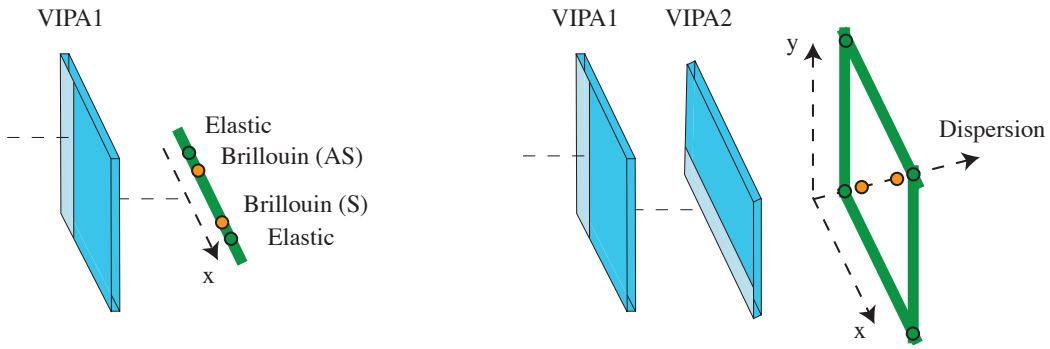



**Figure 3.10:** Dispersion axis in the case of a single (left) and a double stage (right) VIPA. In the first case, dispersion occurs along the same axis where the crosstalk (green line) arises. Conversely, the dispersion axis lies on a diagonal direction when two VIPA etalons of equal dispersion power are crossed. This enables the Brillouin doublet to be spatially separated from the crosstalk.

along the $\hat{x}$ and $\hat{y}$ directions. This allows the Brillouin doublet to be sufficiently separated from the frame where the stray light is spatially confined, thus significantly increasing the accuracy on the peaks localisation. This principle can be further extended in the case of a three-stage VIPA where a dispersion angle of 80° and an extinction ratio of up to 80 dB can be obtained [51]. In general, the total spectral contrast of a cross-axis cascading VIPA spectrometer can be expressed as [51]

$$C \simeq \left(\frac{4\mathcal{F}^2}{\pi^2}\right)^N, \tag{3.36}$$

where N is the number of etalons of equal dispersion power present in the system.

### 3.3.2 Two-Stage VIPA Spectrometer

Despite an increase in the extinction ratio, the higher the number of crossed etalons the greater the amount of optical losses affecting the system. For instance, a three-stage VIPA spectrometer has been empirically found to give an overall throughput efficiency of roughly 7% [51], which leads to a long data acquisition time. A reasonable compromise between spectral contrast and throughput efficiency was obtained with a stage constituted by two crossed VIPA etalons of equal dispersion power. Figure 3.11 illustrates the optical arrangement. The two VIPA etalons are crossed with each other to enable a beam propagation in orthogonal directions. A

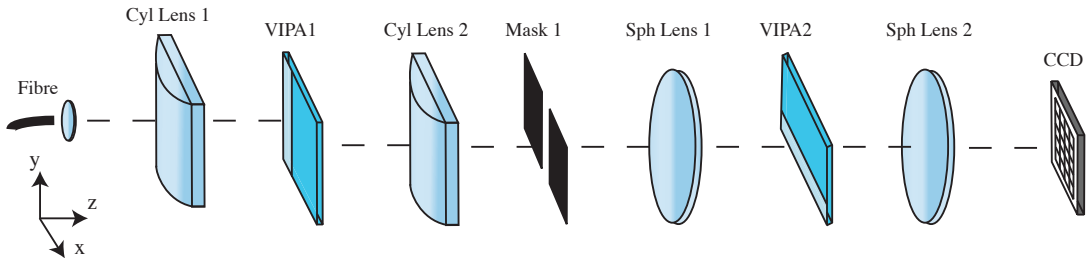



**Figure 3.11:** Diagram of a two-stage VIPA spectrometer. The two etalons are crossed with respect to each other. A spatial mask is placed between the two VIPAs in order to suppress part of the elastic light distributed along the vertical direction.

relay system constituted by lenses of equal focal lengths and set as in a $4f$ system was placed in between and after the two VIPAs. Spatial masks inserted at the Fourier plane of the relay system were used to suppress a substantial amount of stray light. The spectrum was acquired by an *Andor Neo* sCMOS camera having $2560 \times 2160$ active pixels and ensures 60% quantum efficiency with $1\,e^-$ read noise and 0.007 $e^-$/pixel/sec dark current level. Our VIPA etalons were custom built by *LightMachinery* with a total area of $22 \times 25$ mm, an entrance window area of $22 \times 2.5$ mm and a thickness of $d = 2.6$ mm. The etalon substrate was made of fused silica of refractive index $n = 1.47$. Both surfaces were dielectric coated and optimised for a wavelength of $\lambda = 561$ nm. The reflectivity was $R = 0.1\%$ for the AR entrance window, $R = 99.9\%$ for the HR coated front surface and $R = 95\%$ for the rear surface. Figure 3.12 shows the transmission profiles for the front and rear HR coated surfaces. Our VIPA provided a spectral resolution of $\delta\nu = (438 \pm 5)$ MHz, a free spectral range of $\Delta\nu = (39.5 \pm 0.5)$ GHz and a measured finesse of $\mathcal{F} = 90.2 \pm 0.5$. The experimental procedure described in Section 3.2.4 was used to measure both spectral resolution and finesse.

The scattered radiation delivered by a single mode optical fibre (*Thorlabs P1-460B-FC*, NA = 0.13) was collimated by an achromatic FiberPort (*Thorlabs PAFA-X-4-A*) of $f = 4$ mm focal length so that a Gaussian beam of $r_b = 0.35$ mm radius was obtained. The alignment of the fibre port was facilitated by means of a CCD camera monitoring the beam size and shape at a distance of $\sim 500$ mm from the fibre output.

Autofluorescence signals often arise from biological specimens, such as tissues

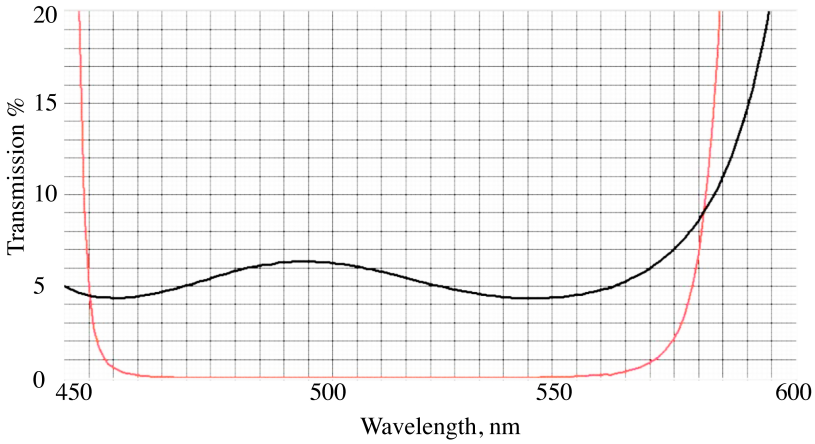



**Figure 3.12:** Transmission profile measured for the front (red) and rear (black) HR coated surfaces of the VIPA in the spectral range of $450 - 570$ nm.

and cells, due to molecular energy levels transitions induced by resonant photons [110]. Relaxation processes lead to the re-emission of photons of lower energies. When collected by the system, the fluorescence signal spreads along the same dispersion axis where the Brillouin spectral peaks are spatially formed. Inelastic Raman scattered light can further contaminate the region of dispersion thus increasing the uncertainty on the measurement. A narrowband optical filter transmitting over a small spectral region around the laser excitation wavelength was therefore essential to prevent propagation of unwanted inelastic light and background radiation along the spectrometer. In particular, a narrowband thin film filter (*Thorlabs MF565-24*, $\lambda = 565$ nm, $\Delta\lambda = 24$ nm) was placed after the fibreport collimator to suppress the parasitic light. The filter had a transmission of $T > 90\%$ at the laser wavelength and an extinction of approximately 50 dB outside its bandwidth.

The condition expressed by equation 3.14 imposed an angle of convergence of $\alpha = 6.06$ mrad for our system so that the intensity of the Stokes and Anti-Stokes Brillouin peaks was maximised within a single FSR of the VIPA. Consequently, the focal length of the cylindrical and spherical lenses, expressed as

$$f \simeq \frac{r_b}{\alpha}, \tag{3.37}$$

was required to be $f \simeq 100$ mm. This value took into account a factor of $C = 1.5$

to compensate for the tails of the beam Gaussian distribution, hence giving a more realistic estimate of the effective beam size at the pupil plane.

In a process similar to the one described in Section 3.2.1, a cylindrical lens focused the collimated beam onto the VIPA entrance window so that an elliptical beam shape was formed. The resulting intensity distribution was unvaried along the $\hat{y}$ axis whilst in the $\hat{x}$ direction it could be assumed to be a narrower Gaussian of FWHM $2w_0 \simeq 58.9$ $\mu$m. Furthermore, from equation 3.26 we obtain that in order to maximise the number of beam reflections inside the cavity and simultaneously minimise insertion losses, light needs to enter the VIPA at an angle of $\theta_0 \simeq 1.1°$. This angle could therefore maximise the finesse of the etalon.

#### 3.3.2.1 Relay systems for elastic light suppression

After each VIPA a $4f$ relay system with magnification of $M = 1$ was set so as to suppress most of the elastic light by means of two spatial masks. In particular, a second cylindrical lens was placed at its focal length distance from the first VIPA such to yield an intermediate interference pattern. A spatial mask was inserted at the Fourier plane to suppress most of the parasitic light. The spatial mask consisted of two vertical razor blades translating along the $\hat{x}$ direction used to block the straight fringes arising from Rayleigh scattering and surface reflections. Both sharp edges and a fine alignment along the $\hat{z}$ axis were required to avoid the formation of unwanted ghost patters due to diffraction. This setup enabled the transmission of the Brillouin peaks confined within one FSR, therefore dramatically decreasing the amount of elastic light entering to the second VIPA.

Figure 3.13 illustrates the contrast enhancement on the resulting spectral pattern obtained with the application of the spatial mask in between the two orthogonal VIPAs . The smaller the amount of light incident to the second VIPA, the higher the overall extinction of the spectrometer. A spherical doublet of 2" diameter was used to focus the residual scattered field onto the second crossed VIPA entrance window leading to a beam propagation along the $\hat{y}$ direction inside the etalon cavity. The second VIPA enabled the inelastically scattered light to be further dispersed along the diagonal direction with respect to the crosstalk lines.

A similar relay optical system constituted by two spherical doublets of same focal

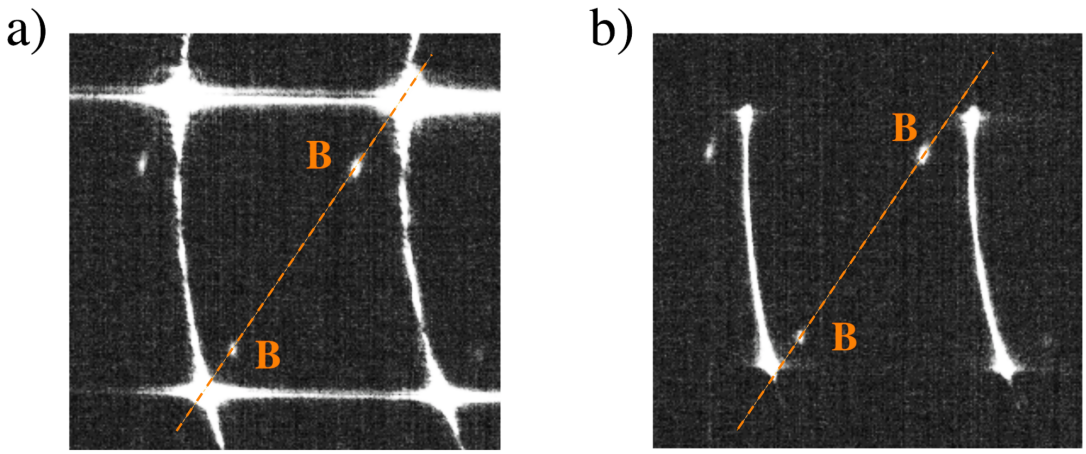



**Figure 3.13:** a) Spectral pattern at the detector plane without masks along the spectrometer. b) The application of a spatial mask in the first relay system allows the crosstalk along the horizontal direction to be cut off. A greater spectral extinction facilitates the localisation of the Brillouin doublet lying along the diagonal dispersion axis.

length ($f$ = 100 mm) was set after the second VIPA. This was used to extinguish the residual crosstalk along the $\hat{x}$ axis by means of a second spatial mask made of razor blades translating along the vertical direction. A high-sensitivity CCD camera could therefore acquire the resulting spectral pattern without being saturated by the elastic component.

#### 3.3.2.2 Optical aberration optimisation

The output field of the VIPA is composed of fringes of equal inclination as in a normal Fabry-Pérot interferometer. Although this field can be assumed to be located at infinity, the distance between the VIPA and the first lens of the relay optical systems is a parameter that needs to be accurately considered in order to minimise optical aberrations. The greater the amount of aberrations affecting the system, the lower the throughput efficiency and the localisation accuracy. In fact, aberrations introduced by lenses would lead to significant optical losses mainly because of beam clipping at the VIPA entrance window. In addition, shape distortion of the spectral peaks would increase the uncertainty in the measurement of the Brillouin frequency shifts. *Zemax* simulations have been carried out to investigate the optimal distance between the VIPA and the first achromatic spherical doublet of the relay telescope.

Figure 3.14 illustrates a diagram for two optical arrangements followed by the resulting Seidel coefficient diagrams for first order aberrations. An object located at

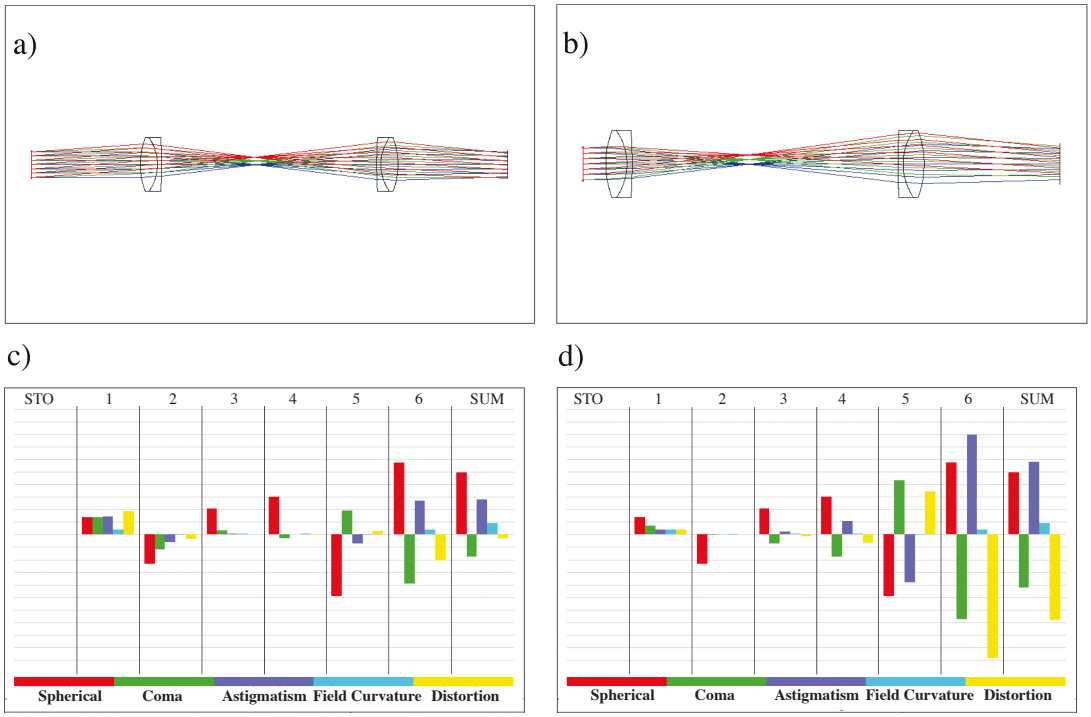



**Figure 3.14:** a) Relay telescope diagram in a $4f$ arrangement, and b) with a distance between first VIPA and doublet shorter than the lens focal length. The Seidel diagrams c) and d) show an increase in the off-axis optical aberrations when the $4f$ symmetry is broken. Grid lines are spaced by 10 $\mu$m.

infinity was taken with field angles of 0° (i.e. along the optical axis), 2° and 4° so that the aperture stop could be taken to a good approximation as the VIPA output. Parallel rays coming out of the aperture could be associated to those transmitted by the VIPA. Manufacturing specifications such as surfaces radii of curvature, optical thicknesses and refractive indexes for the achromatic doublets were taken from the Thorlabs website. The doublets were placed symmetrically reversed at a distance equal twice the effective focal lengths ($\sim$ 200 mm). The distance between the last surface of the second doublet and the image plane, i.e. the location of the second VIPA, was first optimised by Zemax. This was found to be close to the value of the achromatic doublet focal length, as expected. Next, optical aberrations present at the image plane were investigated by varying the distance between the aperture stop (location of the first VIPA) and the first doublet within the range of $15 - 100$

mm. The resulting *Seidel diagrams* show that whilst spherical aberration remains almost equal, the amount of Coma, Astigmatism and Distortion increases dramatically as the distance from the first VIPA to the relay telescope decreases. In fact, when the symmetry of the $4f$ system is broken, a bigger area of the second doublet surface is illuminated by the incident rays, as observed in the diagrams of Figure 3.14. This leads to an increase in the amount of those aberrations dependent on the pupil radius. Since the spectrometer operates with a narrow spectral bandwidth, chromatic aberrations were neglected in the analysis.

### 3.3.3 Apodization Beam Shaping

The intensity distribution of the VIPA output is characterised by a decaying exponential profile, as shown in Figure 3.1. A significant improvement in the extinction ratio of a single VIPA spectrometer can be achieved by imposing a Gaussian intensity profile at the output, which would yield an interference pattern made of sharper peaks than those given by the standard Airy function which stems from the sum of the geometrically decaying amplitudes, as dictated by equation 3.3. This results in a reduced crosstalk at the focal plane the a Fourier-transform lens placed next to the VIPA, and therefore in an increase in the extinction ratio.

Beam shaping by imposing a given intensity transmittance is a technique known as *apodization*. Different apodization approaches have recently seen extensive use in Fourier transform spectroscopy in the attempt to increase the signal-to-noise ratio (SNR). For instance, the application of an apodizing function to certain regions of an interferogram can lead to the attenuation of the high spatial frequency information of the spectrum, hence resulting in a higher SNR [111].

There is a variety of commercially available apodization filters that are used to yield a uniform illumination profile in an optical system. For instance, a Gaussian beam profile can be obtained from a flat beam by means of an apodization filter made of high optical density at the edges and continuously decreasing towards the centre of the filter. For our purposes, an ideal apodization filter would convert the exponentially decaying beam into a Gaussian like intensity profile [48, 112]. The application of such a filter next to the VIPA etalon could eventually increase the extinction ratio by a factor of two as compared to conventional VIPAs arrange-

ments [113]. Nevertheless, since an exponential-to-Gaussian profile filter is not yet commercially available, a different approach was taken. The continuously variable neutral density (ND) filter shown in the left hand side of Figure 3.15 was used. The

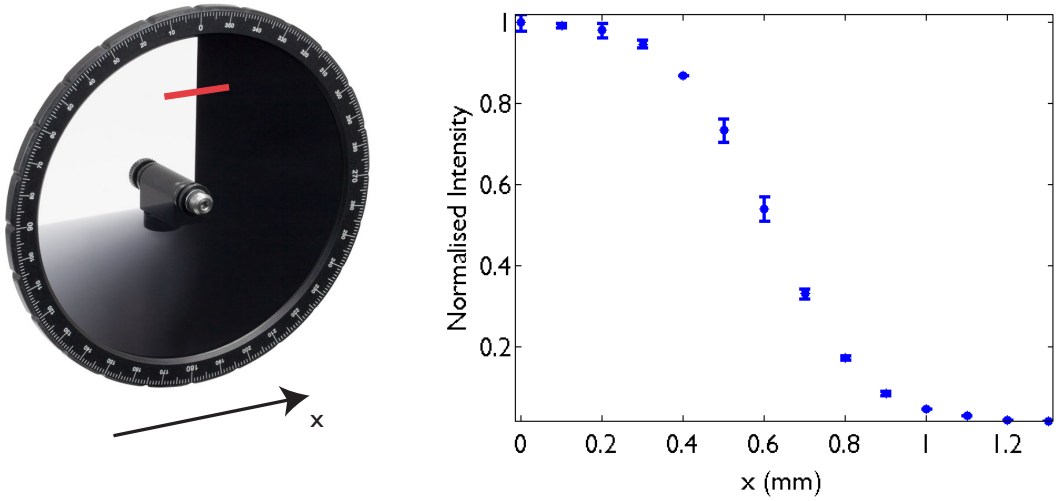



**Figure 3.15:** Circular, continuously variable neutral density filter (left). The filter was translated along the $\hat{x}$ direction so that the transmitted beam intensity was measured within the region of transition (red line) passing from an OD = 0 to OD = 4. The resulting transmission profile (right) in this region is shown to be smoother than a theoretical step function.

optical density (OD) defined by

$$\mathrm{OD} = \log_{10}\left(\frac{1}{T}\right), \tag{3.38}$$

where $T$ is the transmission coefficient, gradually varies around the circular filter within a range of OD $= 0 - 4$. It is practically not possible to produce a perfectly sharp transition from $OD = 0$ to 4.

When the transmission profile is measured at the transition region, the result is shown in the right hand side of Figure 3.15. As expected, the filter was found to have a more rounded profile within a region of 1 mm across the edge rather than a sharp step function. The transmission profile across the edge of the transition region of the neutral density filter was used to apodize the exponentially decaying beam of the VIPA output. Figure 3.16 illustrates the resulting product between the transmission profile obtained in the measurements and an exponentially decaying profile equal to

that of the output field of the VIPA. Even though a perfect Gaussian profile could

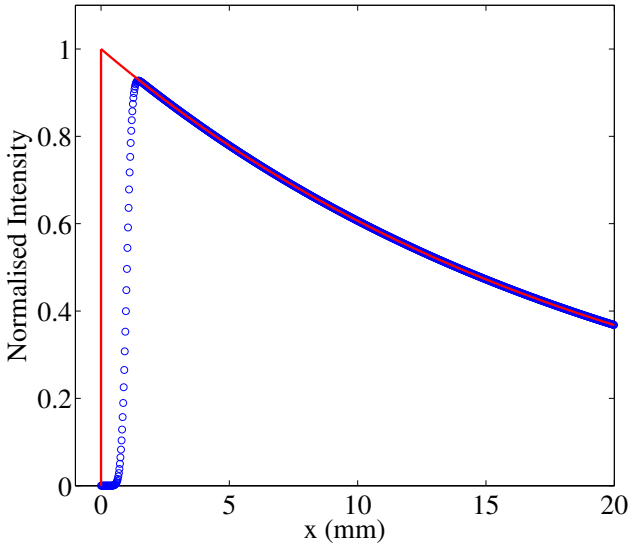



**Figure 3.16:** Product of an exponential function (red) characterising the intensity output of the VIPA and the transmission profile obtained with the neutral density filter.

not be obtained, a more rounded shape was achieved by placing the varying neutral density filter such that the maximum intensity of the exponentially decaying beam was accurately aligned at the transition region. The truncated Gaussian profile at the VIPA output led to a significant reduction of the crosstalk resulting in an increase in the extinction ratio by $\sim$ 10 dB with 2 dB excess loss only, as further discussed in the following section.

An ideal configuration would have a linearly varying reflectivity at the second surface of the VIPA so as to yield a Gaussian beam profile at the output without the need of an additional apodization filter. A self-apodizing VIPA would result in a higher throughput efficiency. Nevertheless, gradual variations in the surface reflectivity may result in a change in the optical paths and therefore in the phase of the transmitted beams. To date, this represents the main manufacturing limitation for commercial VIPAs.

### 3.3.4 Throughput and Extinction Measurement

A VIPA etalon can be calibrated by first looking at low interference orders, i.e. at large angles $\theta$. This ensures that light enters the etalon through the entrance window without optical losses. In fact, besides ghost reflections the beam can be easily clipped in proximity of the transition region of the VIPA that outlines the AR and HR surfaces. A high-precision rotational stage can be useful to gradually decrease the incident angle producing higher interference orders. A power meter can be used to measure the throughput efficiency of the VIPA during the alignment. Maximising the output power at higher orders whilst varying the $z$ position of the VIPA along the optical axis is a reasonable approach to ensure that the beam waist is at the right location. A conventional camera can monitor the beam at the entrance window to avoid beam clipping along the transition region between AR and HR coated surfaces.

A throughput efficiency of $55.5\% \pm 0.5\%$ was measured at the Fourier plane of the $4f$ system. The measurement was made with no spatial masks in the system and by reading the optical power at both the fibre port output and the focal plane of the second cylindrical lens. A transmission of $37.0\% \pm 0.5\%$ was measured from the intermediate plane of the first relay system to the detector plane. This gave an overall throughput efficiency of $20.5\% \pm 0.5\%$, in agreement with previous reports [51].

A measurement of the extinction ratio of both a single-stage and a double-stage VIPA was carried out by coupling a single longitudinal mode laser directly into the spectrometer. An anodised metal box was used to enclose the optical system so to avoid detection of any background stray light coming from the surrounding laboratory environment. In order to proceed with the extinction measurements, a low-cost *Pulnix* CCD camera was used. A variety of neutral density filters of calibrated optical densities ranging $\mathrm{OD} = 0 - 7$ was used to overcome the limited dynamic range of the camera. This enabled to reconstruct the inherent spectral profile of the VIPA, in particular when the intensity of the incident light was higher compared to the saturation level of the camera. Images of the interference pattern composed of two subsequent interference orders were acquired starting from the highest OD

to ensure that peaks of equal intensities were not saturating the camera pixels. A linescan along the dispersion axis confined by two interference orders was obtained to retrieve the intensity profile. Figure 3.17 shows the non-saturated interference pattern in the case of a two-stage VIPA where a linescan along the dispersion axis was performed between two adjacent orders. This process was iterated by gradually

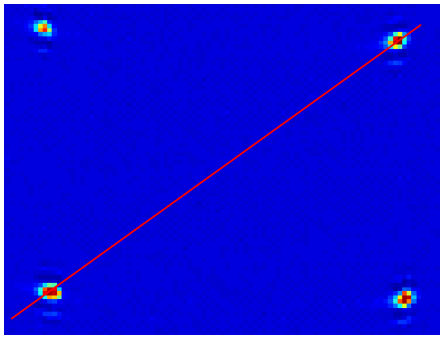


**Figure 3.17:** Interference pattern of a two-stage VIPA spectrometer. The intensity of the spectral peaks due to the laser radiation was set to be equal. The highest OD filter was first used to keep the interference peaks below the saturation level of the CCD camera. A linescan (red line) along two subsequent interference orders was performed to retrieve the intensity profile.

lowering the optical density of the filters until the camera was almost completely saturated by the crosstalk caused by stray light. The acquisition time was kept constant at 200 ms at each measurement. From the spectra acquired at different OD levels, a full dynamic range intensity profile was reconstructed by rescaling the raw spectra acquired according to the respective attenuation levels. Figure 3.18 shows the resulting extinction curves in the case of a single-stage and a two-stage VIPA spectrometer. With the camera placed at the focal plane of the second cylindrical lens, an extinction ratio of $\sim$ 30 dB was measured for a single VIPA. The spectral contrast achieved is in agreement with previously reported measurements [51]. A two-stage VIPA gave an overall extinction of $\sim$ 48 dB. This was further increased by $\sim$ 4 dB with the insertion of the spatial mask at the Fourier plane of the first relay system, i.e. between the two VIPAs. In fact, whilst the second spatial mask is used to reduce the amount of stray light delivered to the camera to avoid saturation, the first one actively improves the spectral contrast because of the lower amount of light entering the second VIPA. The application of the apodization filter gave an

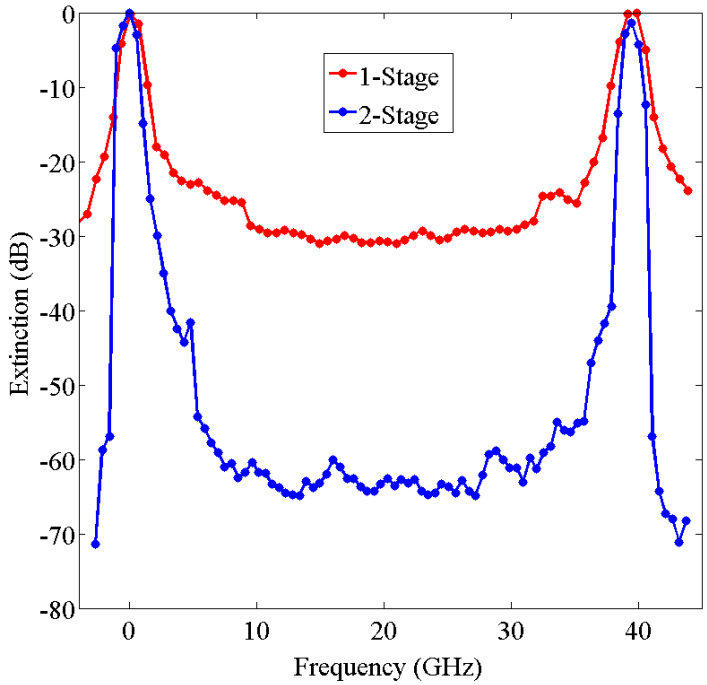



**Figure 3.18:** Normalised spectral response of both single (red) and double (blue) stage VIPA spectrometer to a single longitudinal mode laser radiation. The extinction ratio increases by 30 dB from a single to a double stage spectrometer.

additional $\sim$ 9 dB improvement, hence an overall extinction ratio of up to 60 dB was achieved by our two-stage spectrometer. This value was considered to be sufficient to resolve Brillouin spectra of semi-transparent biological samples.

## 3.4 Spectral Contrast Enhancement

An extinction ratio of up to 80 dB can be obtained with a three-stage VIPA configuration [51]. However, this would give a maximum throughput efficiency of 7%, which would make it unsuitable for detecting low intensity signals such as the Brillouin scattered light. In an ideal setup, a single VIPA of high spectral contrast would be used to minimise data acquisition times. This could be achieved by suppressing the Rayleigh scattered light so that only the Brillouin spectrum would be dispersed by the etalon and acquired by the detector. Since narrowband dielectric filters are not available with bandwidths of the order of 1 GHz, other approaches need to be

considered.

### 3.4.1 Molecular Absorption Filter

There are currently two different methods that could potentially be used in conjunction with a single stage VIPA. The first method relies on the application of molecular absorption filters, which have been widely employed in Brillouin Light Imaging Detection and Ranging (LIDAR) for remote sensing of ocean temperatures [114, 115, 116]. A gas cell can act as a notch filter if the incident light is in resonance with the associated narrowband atomic energy transition. Photon absorption can impede the elastically scattered light to be transmitted, leaving the off-resonant inelastic field almost unchanged. In Brillouin LIDAR systems, an optically pumped absorption filter constituted of Rubidium has been shown to achieve a suppression ratio of 50.5 dB for a laser wavelength of 543.3 nm [117]. The same principle has been recently applied to enhance a two-stage VIPA spectrometer [118]. A cylindrical iodine absorption cell was used to absorb a 532 nm single mode solid-state laser line by increasing the medium temperature. A 50 dB suppression of the Rayleigh peak was obtained at a cell temperature of 100°C. Figure 3.19 shows a diagram of the vapour cell operating as a notch filter.

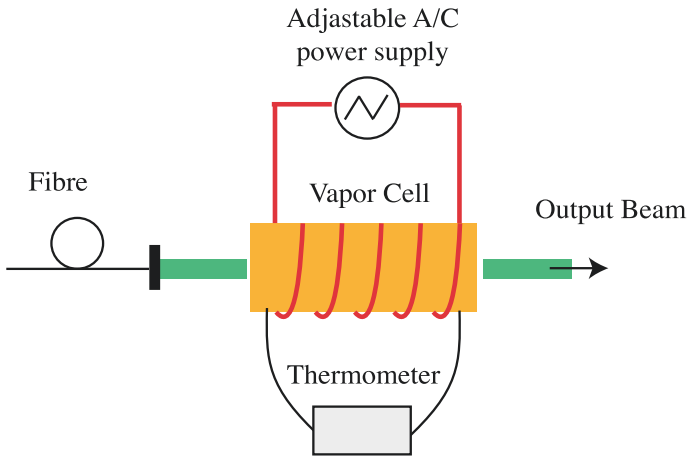



**Figure 3.19:** Diagram of the vapour cell arrangement. The output beam of the fibre passes through the vapour cell where absorption of the Rayleigh scattered light takes place. The cell is heated up to a temperature of 100 °C. After [118].

Although an absorption filter can eliminate the undesired elastic light collected by the system, the Brillouin signal is also significantly attenuated when passing through the cell due to an increase in the iodine vapour density at high temperatures. Furthermore, this approach relies on specific atomic and molecular compounds whose allowed energy transitions match the resonant frequency of the laser line. Nevertheless, it is rather difficult to find media with a single absorption line due to the more complex energy levels characterising a certain molecular structure. Multi atomic transitions might induce photon absorption at different frequencies within a small spectral range. This can result in the suppression of the Brillouin scattered light at those frequencies, as in the case of a iodine gas cell [118, 119]. In addition, the employment of absorption filters would restrict the choice of the laser wavelengths suitable for Brillouin spectroscopy to those dictated by the atomic structure of a limited range of absorption media (e.g. Rubidium, Iodium).

### 3.4.2 Heterodyne Interferometry

A more flexible and reliable approach might see the application of an heterodyne interferometric system to the spectrometer. Heterodyne techniques are mainly employed in optical fibre sensing and characterisation where stimulated Brillouin scattering can provide information about tensile stress and temperature of the fibre silica. Conventional heterodyne detection make use of the cross-correlation between the Brillouin radiation and a modulated local oscillator reference signal of frequency close to the Brillouin scattered light [97, 120]. A beating component arises when the two signals are mixed. This is characterised by a lower frequency given by the difference of the Brillouin and the local oscillator frequency. A digital correlator is used to separate both a DC term and other high-frequency components from the beat term. A spectral resolution of hundreds kHz has been demonstrated to be achieved by time domain heterodyne detection [96].

A purely interferometric approach designed to suppress the elastic contribution without the requirement of fast detectors and other narrowband and spectrally tunable sources of light is proposed here. In a configuration similar to that of a conventional Michelson interferometer, the radiation of a stabilised single longitudinal mode laser can be used as a reference to destructively interfere with the coher-

ent elastic Rayleigh scattered light so that only the inelastic contribution would be detected.

Interference in a Michelson interferometer is governed by the *Superposition Principle*. This states that the total amplitude of two waves of equal frequency $\omega$ at a point $r$ is the sum of the amplitudes

$$E(r,t) = E_1 e^{i(\phi_1(r)-\omega t)} + E_2 e^{i(\phi_2(r)-\omega t)}, \tag{3.39}$$

where $\phi_1$ and $\phi_2$ are the relative phase of the two waves. The intensity at point $r$ will be the modulus square of the total amplitude $E$, that is expressed as

$$I = |E|^2 = |E_1|^2 + |E_2|^2 + 2Re[E_1 E_2^* \exp(\Delta\phi)], \tag{3.40}$$

where the phase difference $\Delta\phi = \phi_2 - \phi_1$ can be defined in terms of the optical path difference $\Delta z$ relative to the two beams travelling in the parallel $\hat{z}$ direction (i.e. for $\theta = 0$)

$$\Delta\phi = \frac{2\pi n \Delta z}{\lambda} \tag{3.41}$$

so that

$$I = I_1 + I_2 + 2\sqrt{I_1 I_2}\cos\left(\frac{2\pi n \Delta z}{\lambda}\right) \tag{3.42}$$

Consequently, for two beams of equal amplitude ($E_1 = E_2$) we have

$$I = 2I_0\left[1 + \cos\left(\frac{2\pi n \Delta z}{\lambda}\right)\right]. \tag{3.43}$$

Assuming that the elastic signal has same spectral content of the reference so that equation 3.43 is applicable to each delta function spectral component, and hence to the total distribution, we have that constructive interference occurs for $\Delta z = n\lambda$, whilst total destructive interference when $\Delta z = (n + 1/2)\lambda$.

An experimental setup to test the proposal is shown in Figure 3.20. The laser radiation is split in two arms by a partially reflective mirror M. In one arm the light probes the sample and the scattered light is coupled back into a single-mode fibre S1. The second arm can be used to couple the laser beam into a second fibre S2 by means of a fibre port mounted on a high-precision translational piezo (PZ)

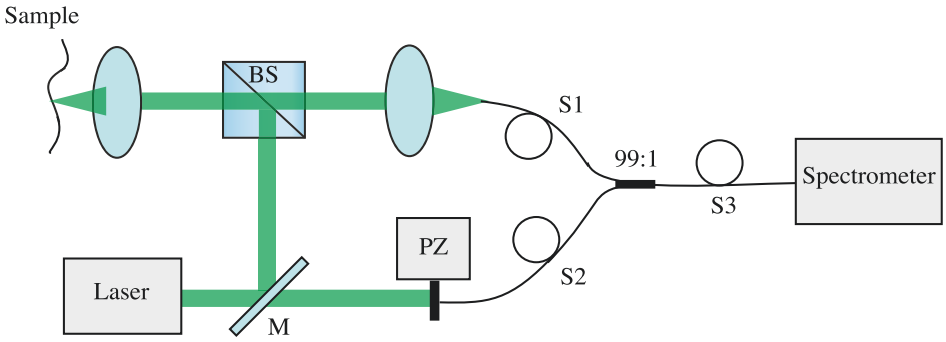



**Figure 3.20:** Optical arrangement for a Michelson interferometric system. The Rayleigh scattered light is suppressed by destructive interference with a reference signal coupled into a single mode fibre.

stage. The scattering and the reference signal are combined by a fibre coupler so that interference occurs. This would determine the output intensity of the SM fibre S3.

In more detail, a translation of the fibre S2 along the $\hat{z}$ direction can introduce an optical path difference of half a cycle ($\Delta z = \lambda/2$) between the reference and the Rayleigh signal. In addition, translation in the $\hat{x}$ and $\hat{y}$ directions varies the amount of light coupled into the fibre so that the amplitude of the reference signal can be matched with that of the light scattered by the sample. The interference pattern arising at the S3 output, i.e. at the entrance of the spectrometer, is a Gaussian distribution due to the single mode of propagation through the fibre. Consequently, destructive interference would result in the absence of parasitic light at the spectrometer without the appearance of other interference fringes. This would allow only the Brillouin scattered light to be dispersed by a single VIPA, which could significantly increase the extinction ratio.

The main limitation of the configuration described is given by the thermal drifts of the various optical components due to even small thermal fluctuations occurring in the surrounding environment. Indeed, thermal drifts may cause changes in the optical path length, therefore resulting in random intensity fluctuations at the fibre output. An outer shell insulating the system might be required for thermal drift monitoring and prevention.

### 3.4.3 VIPAs of different dispersion power

Although the presence of the elastically scattered light in the spectrometer is one of the main limiting factors in Brillouin spectroscopy, alternative broadband light sources can also affect the spectral analyses. All the extra inelastic contribution transmitted through the narrowband filter placed at the entrance of the spectrometer would spread along the dispersion axis defined by the VIPA arrangement, therefore resulting in a continuos crosstalk overwhelming part or the entire Brillouin peaks. In particular, any sources of background light and autofluorescence signals emitted by the samples can eventually compromise the localisation of the Brillouin peaks. This problem can arise for either a single VIPA or multiple crossed VIPA etalons of equal dispersion power (i.e. with an equal free spectral range). In the case of a two-stage VIPA spectrometer, all the extra inelastic contribution would spread along the same diagonal dispersion axis where the Brillouin peaks are formed.

A different scenario arises if crossed etalons of different dispersion powers would be employed. Although the angle between the first and the second dispersion axis remains at 45°, the free spectral range of the second etalon would ultimately determine whether dispersion arises along multiple lines. In fact, a two crossed VIPA configuration with etalons of different dispersion powers would give rise to parallel but spatially separated spectral lines for the Stokes and the Anti-Stokes shifts. In order to better understand this concept, a computational simulation for a tandem of two crossed VIPAs of free spectral range $\Delta\nu_1 = 33$ GHz and $\Delta\nu_2 = 20$ GHz was carried out. Figure 3.21 shows the resulting interference pattern at detection with the Anti-Stokes dispersion lines outlined over a full FSR. Light is dispersed along a diagonal direction at 45° with respect to the $\hat{x}$ axis. The first dispersion line covers a spectral range of $0 - 20$ GHz, i.e. it first covers the FSR of the second VIPA. The residual spectral range $(20 - 33$ GHz) is spread along a second line arising from the horizontal axis in correspondence to the end of the first dispersion line and intersects with the vertical axis. The sum of the two spectral lines gives the free spectral range of the first VIPA. A symmetrical behaviour characterises the Stokes dispersion lines originated from the other extreme of the interference pattern. In this case dispersion would take place in the opposite direction. Consequently, an appropriate choice of

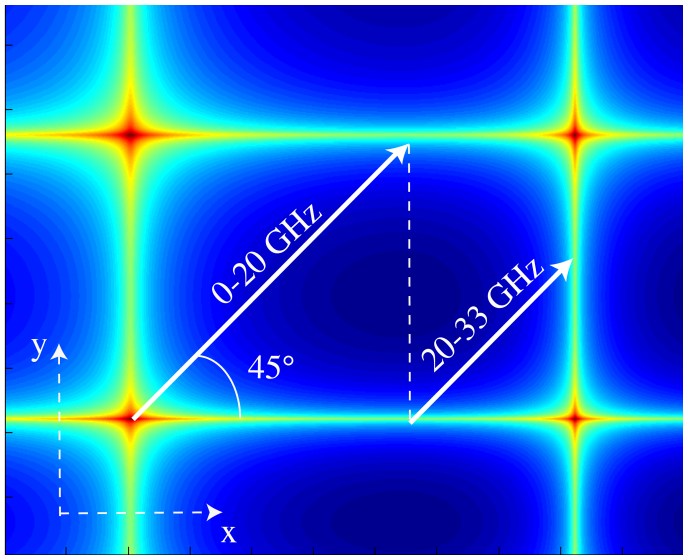



**Figure 3.21:** Logarithmic intensity of a two-stage VIPA of free spectral ranges $\Delta\nu_1 = 33$ GHz and $\Delta\nu_2 = 20$ GHz. The Anti-Stokes dispersion axis (white arrow) is formed at 45° with respect to the first VIPA dispersion axis along the $\hat{x}$ direction.

the VIPAs free spectral range can be found so that the Stokes and Anti-Stokes lines would not overlap together for a wide spectral interval.

Although fluorescence can also have an Anti-Stokes component due to thermal energy transitions [121, 122], samples autofluorescence mainly arises due to Stokes shift. As a result, whilst the Stokes shifted Brillouin peaks would be affected by the parasitic inelastic light propagating through the spectrometer, the Anti-Stokes peaks would arise along the dispersion lines where no other inelastic spectral content would be present. This would enable the Brillouin signal to be still detected with great accuracy even in presence of a significant amount of autofluorescence and stray light.

A two-stage VIPA spectrometer with an appropriate choice of the etalon free spectral ranges might allow the application of Brillouin microscopy together with other imaging modalities, such us fluorescence microscopy.

# Chapter 4

# Experimental Methods

Previous investigations established the VIPA etalon as a suitable disperser device to measure the spectral information of the Brillouin scattered light. Given the high throughput efficiency, the VIPA spectrometer was used to enable fast scanning over a variety of biological samples. Since biological specimens have a limited lifetime, a fast data acquistion of the Brillouin spectra (i.e. below 1 second) was essential to yield an efficient imaging system.

Following the design of a robust spectrometer of high spectral contrast and resolution, several imaging modalities were tested to investigate the best performance in terms of spatial resolution, signal strength and suppression of stray light. Before focusing on high resolution Brillouin microscopy, a single-point 90° scattering geometry was designed to retrieve preliminary data of the Brillouin spectra of a variety of liquids. A detailed analysis on the spectral broadening of the Brillouin peaks due to finite illumination and collection system numerical apertures was carried out. Theoretical and experimental results confirmed that spectral broadening is minimised in a backscattering geometry, hence allowing the employment of high NA microscope objectives. This work has been published in *Applied Physics Letters* [14].

The spectral broadening analysis was necessary to find the optimal geometry to extend Brillouin spectroscopy from a point-sampling technique to a new high resolution imaging modality. Two different backscattering configurations were investigated. The first consisted of a confocal dark-field arrangement where the sample

was illuminated by a cone of light yielded by an annular beam focused by an objective lens. The scattered field was collected through the centre of the same pupil. Conversely, undesired surface reflections were rejected by the system. The detection of the scattered signal was of great advantage to maintain a high spectral contrast given the relatively low amount of light incident to the etalons. Images were acquired by scanning over the sample by means of a motorised stage.

Despite the minimal parasitic stray light collection, the use of the dark field arrangement was limited by a poor axial resolution. In fact, the narrower the annular beam focused to the sample, the greater the depth of field. An infinite narrow annular beam would generate a so-called *Bessel beam* characterised by an infinite depth of field [123, 124]. Furthermore, data acquisition times were strongly affected by the employment of a customised 45° prism drilled on two sides so as to yield two concentric holes on the opposite surface, which reflected $< 18\%$ of the input light at illumination. Consequently, the second configuration consisted of a scanning confocal system where the prism was replaced by a beam splitter to provide a uniform illumination. The confocal arrangement enabled high spatial resolution imaging and a significant decrease in the data acquisition times. The Brillouin microscope employed a two-stage VIPA spectrometer together with a high NA oil immersion objective to obtain high spectral contrast, which enabled the localisation of the Brillouin peaks of turbid samples. Fast, high resolution Brillouin imaging of biological specimens had become therefore a realistic proposition.

## 4.1 90° Scattering Geometry

Initial setup and system verification was performed by measuring the Brillouin spectra of assorted liquids with a 90° scattering geometry using low NA lenses. A 90° scattering geometry is a dark-field arrangement where the incident illumination laser beam forms a 90° angle with respect to the collection axis. Consequently, surface reflections were suppressed so as to allow detection of the isolated scattered light.

The 90° scattering geometry setup has seen extensive use in Brillouin spectroscopy. One of the first designs of this optical arrangement was realised by Chiao and Stoircheff in 1964 [22]. A He-Ne laser was combined with a scanning Fabry-Pérot

interferometer and a photo detector to analyse spectral variations of the Brillouin scattered light in response to changes in temperature of a variety of liquids. Maguire *et al.* [125] used this configuration to determine values of the Landau-Placzek ratio of liquids by means of an argon-ion laser operating at 200 mW and a piezoelectrically scanned Fabry-Pérot interferometer of finesse 35. Similar configurations were used to investigate temperature variations of glass [23, 37, 126, 127] and ethanol [128, 129]. Benedek and Fridtsch engaged a high resolution grating spectrograph to measure elastic constants of alkali halide crystals [74] and liquids [25].

Itoh and Ko were the first to employ an angular dispersion non-scanning Fabry-Pérot etalon device together with a high-sensitive CCD camera in a 90° arrangement [45, 46, 102]. As a result, acquisition times of the Brillouin spectra of liquids were reduced to a few seconds. More recently, Koski *et al.* measured the light scattered by acoustic phonons of solids and liquids at high pressure by combining a high-pressure cell containing the samples with a non-scanning Fabry-Pérot etalon and a CCD camera for data acquisition [43].

Figure 4.1 shows the optical setup of our 90° scattering geometry system. A

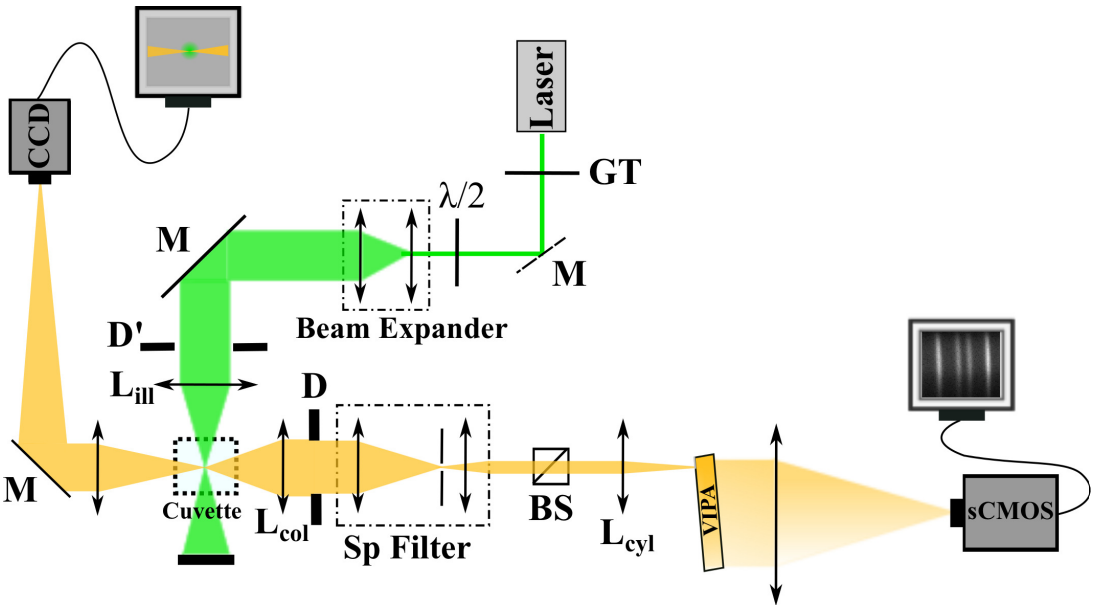



**Figure 4.1:** Optical setup for a 90° scattering geometry.

diode-pumped solid-state (DPSS) single longitudinal mode *Cobolt Jive* laser was used as a light source of $\lambda = 561$ nm and maximum power of 300 mW. A single

longitudinal mode laser was essential to perform Brillouin spectral analyses. In fact, since the resulting spectral profile at the Fourier plane of the VIPA is the convolution of the Airy function and the laser spectral line [130], the narrower the spectral bandwidth the higher the instrumental finesse. The Cobolt laser ensured a high level of stability of approximately 50 MHz and a narrow spectral bandwidth of $< 1$ MHz, which was far below the spectral resolution of our VIPA spectrometer. Conversely, gas lasers such as He-Ne are characterized by several longitudinal modes depending on the gain media and cavity lengths, as described in Section 3.2.4. Furthermore, standard diode lasers suffer from high instability because of the appearance of multiple oscillating frequency lines [131]. Each laser spectral line leads to the formation of an associated Stokes and an Anti-Stokes peak due to light scattering from acoustic phonons, which impede measurement of the Brillouin frequency shift.

The 0.7 mm diameter Gaussian beam emitted by the single longitudinal mode laser was expanded to 25 mm in order to fill the surface of an achromatic lens $L_{\text{ill}}$ ($f = 30$ mm), which focused the light from air into a glass cuvette filled with the liquid sample. Equation 2.5 has shown that the theoretical intensity of the scattered light is zero along the direction of the incident electric field $\mathbf{E}$. In order to maximise the signal strength, a Glan-Thompson (GT) polariser and a half-wave plate ($\lambda/2$) were used to provide s-polarised light at the sample plane. The light scattered by liquids was collected by a second achromatic lens $L_{\text{col}}$ of equal focal length ($f = 30$ mm) to that of $L_{\text{ill}}$ so as to maximise collection of light from the scattering volume. Successively, the scattered radiation was spatially filtered by means of a 75 $\mu$m diameter pinhole to ensure confocal arrangement. Most of the light emitted outside the scattering volume was therefore suppressed.

Since many liquids are transparent at 561 nm and collection of surface reflections was minimised by geometry, the signal detected was reduced to the Rayleigh scattered light. The absence of the elastic crosstalk enabled the use of a single VIPA to measure spectral properties of liquids. In a way similar to that described in Section 3.2.1, a cylindrical lens $L_{\text{cyl}}$ ($f = 200$ mm) focused the light onto the VIPA entrance window. The VIPA used in the present arrangement had an experimental spectral resolution of $\delta\nu = (438 \pm 5)$ MHz, a free spectral range of $\Delta\nu = (39.5 \pm 0.5)$ GHz and a finesse of $\mathcal{F} = 90.2 \pm 0.5$. The output field of the VIPA was Fourier transformed

so as to spatially disperse the Brillouin spectrum, which was then recorded by the Andor Neo sCMOS camera with an integration time of a few seconds.

Since the scattered radiation from liquids is weak and thus not visible to the naked eye, the alignment process of the confocal detection required additional optics. A *Starlight* CCD camera was placed at the conjugate plane of the pinhole. This allowed to monitor the scattering volume and to match it with a reference beam sent through the collection arm. A reference of the pinhole location could be taken by imaging the laser beam when passing through the spatial filter. Once the reference was recorded, fine system alignment could be performed by monitoring and translating the probe volume in the three dimensions. A mirror M placed along the illumination arm was used to control the scattering volume. The high-precision alignment process of the 90° geometry confocal system was of fundamental importance to maximise collection of the weak scattering signal.

### 4.1.1 Data Fitting

The spectra acquired experimentally are processed to obtain measurements of the Brillouin frequency shifts, spectral linewidths and peak intensities by means of least-squares fits. The data processing initially involves an image background subtraction followed by a fit. Figure 4.2 shows the resulting fit for the spectrum acquired with liquid Benzene, which is composed by a central Rayleigh peak and a Stokes and a Anti-Stokes Brillouin peak. A linescan of the intensity profile is taken along the dispersion axis in the region where the signal strength is maximised by the illumination, as described in Section 3.2.1. An average of the intensity profiles along the $\hat{y}$ direction can significantly improve the signal-to-noise ratio (SNR) of the resulting spectral profile.

The Matlab code uses a non-linear optimisation algorithm to decompose a complex, overlapping-peak signal into its component parts. In other words, the fundamental underlying peak intensity profiles whose sum yields the resulting spectral distribution can be identified. This can be observed in Figure 4.2 where the spectrum is decomposed into three peaks, i.e. the central Rayleigh and the two adjacent Brillouin peaks. Each peak is fitted by an appropriate Lorentzian function describing the inherent spectral profile of the Brillouin scattered light. The fitting error (expressed

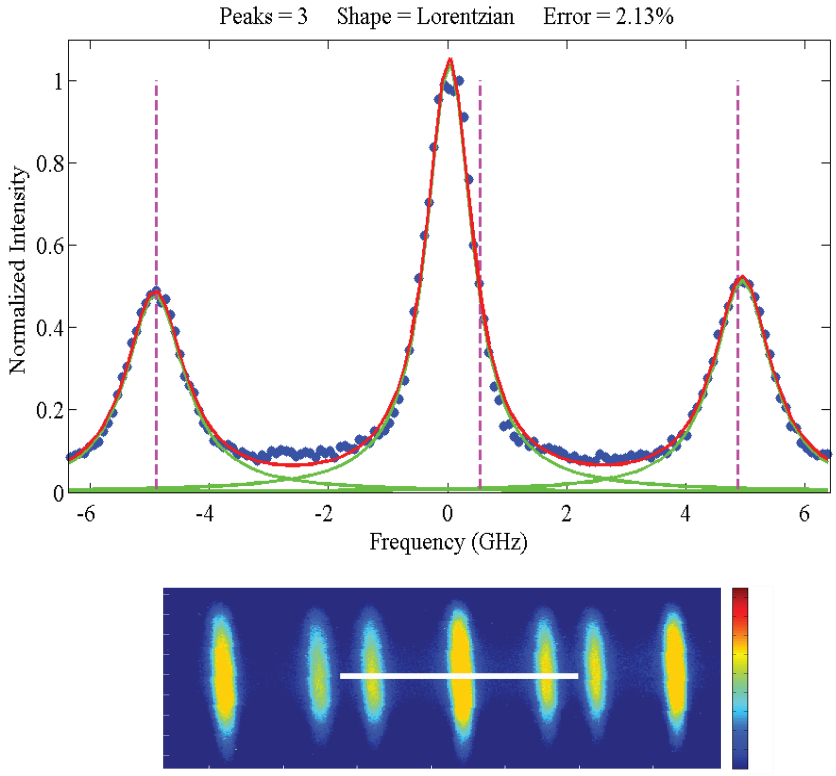



**Figure 4.2:** Least-squares fit of the Brillouin spectrum of Benzene (top) and raw fringe pattern acquired by the CCD camera. Blue dots represent experimental data. Bespoke algorithms decompose the signal into the three components (green lines) whose sum makes up the resulting profile (red line). A Lorentzian function is used to fit the spectral peaks.

by the standard deviation and the interquartile range) describes the spread of the data from the mean value. When measuring the frequency shift of the Brillouin doublet, a reference frequency is taken at the location of the Rayleigh peak.

### 4.1.2 Spectral Axis Linearisation

The interference pattern arising from the VIPA is described by the Airy function, as discussed in Section 3.1. The pattern is recorded by the sCMOS camera and processed by bespoke algorithms written in *Matlab* for spectral axis linearisation, background subtraction and Lorentzian fitting. Finally, values for the frequency shift, spectral linewidth and intensity of the Brillouin peaks are obtained.

The linearisation stage is required because the angular (or spatial if considered

in the Fourier plane) separation follows a square root dependency, as shown in Appendix A. This dependency can be observed in Figure 4.3, which presents a spectrum containing several interference orders acquired with liquid benzene. Peaks

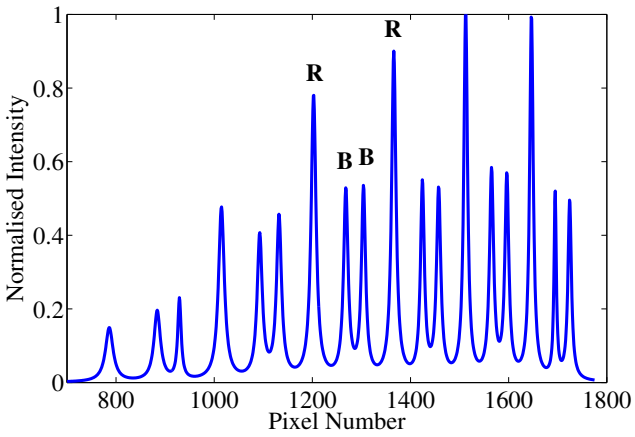



**Figure 4.3:** Measured spectral intensity of liquid benzene for seven subsequent interference orders. The separation between the Rayleigh peaks observed in the graph decreases as the square root of the $\hat{x}$ axis, which is here expressed in terms of the camera pixel numbers.

of higher intensities arise from the elastic Rayleigh scattering whilst the doublets appearing in between two adjacent orders are the Stokes and Anti-Stokes Brillouin peaks. The lower the interference order, the shorter the separation between two Rayleigh peaks. In the frequency domain, the interval between adjacent orders is a constant defining the FSR of the VIPA. Figure 4.4 shows a plot of the measured interval widths as a function of the orders associated with multiple FSRs. The approach used to equalise the separation between successive Rayleigh peaks involved the application of a suitable function to scale the $\hat{x}$ axis. The best function depends on features of the etalon, such as the refractive index and the etalon tilt [43], and was empirically determined as

$$f = \left( \frac{x + b * c}{c} \right)^{1/a}, \tag{4.1}$$

where $x$ is the original $\hat{x}$ axis in pixel units and $a$, $b$ and $c$ are arbitrary constants. In order to find these three parameters, the distance between successive Rayleigh peaks was first measured. A least-squares fit of the curve observed in the graph was

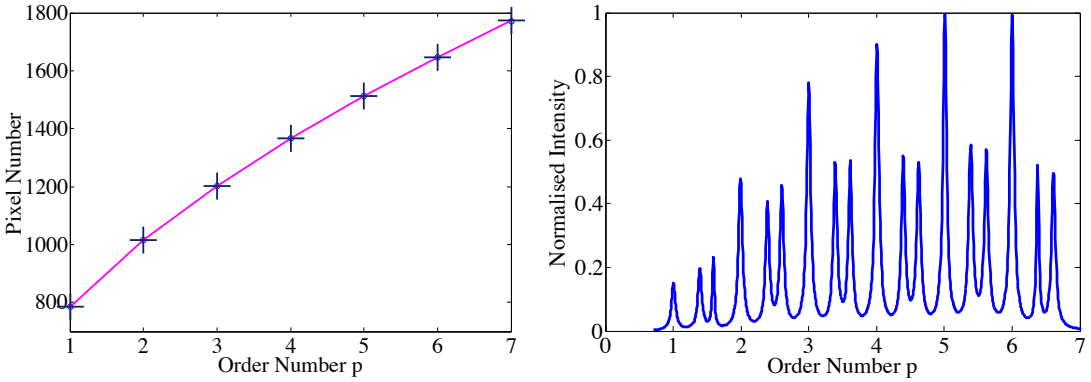



**Figure 4.4:** Measured Rayleigh peaks separation in pixel units on a linear scale (left). In order to perform an accurate fit (red line), seven successive interference orders were taken into account. Linearised spectrum for liquid benzene (right). The separation between successive orders is associated with the FSR in the spectral domain.

performed by using the inverse function of equation 4.1

$$x = c\,(f^a - b), \tag{4.2}$$

which gave values of $a = 0.594 \pm 0.023$, $b = 0.733 \pm 0.014$, $c = 453.1 \pm 4.3$. These were used to linearly scale the $\hat{x}$ axis by means of the function expressed in equation 4.1. Figure 4.4 shows the resulting linearised intensity profile of the scattering spectrum acquired with liquid benzene. The linearised axis can be finally expressed in the frequency domain by scaling it with the FSR of the VIPA.

Given the high stability of the single longitudinal mode laser, the Rayleigh peaks can be assumed to arise at a fixed location over time. The linearisation process of the spectral axis is therefore required to calibrate the system before taking measurements of the Brillouin spectra. Nevertheless, parameters defining the scale function expressed in equation 4.1 are fixed regardless of the samples being used. It is however good practice to repeat the linearisation process on a monthly basis due to random drifts of the optical components.

### 4.1.3 Brillouin Spectra of Liquids

In order to test the performance of the 90° scattering geometry system, the Brillouin spectra of a variety of liquid samples were acquired. Figure 4.5 shows the calibration

spectra acquired at low NA (i.e. NA = 0.1) for different liquid samples after data processing. Experimental data points for methanol are also plotted for comparison

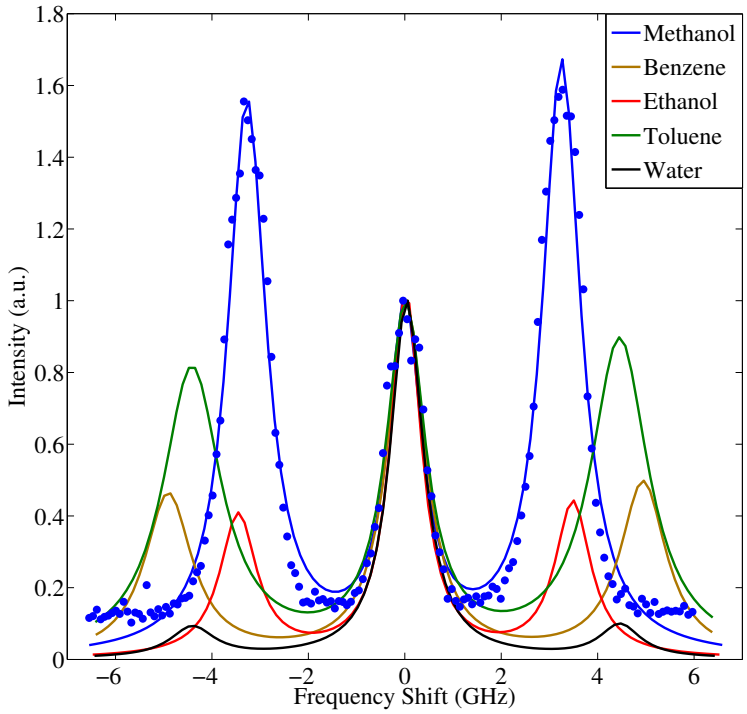



**Figure 4.5:** Fitted Brillouin spectra (solid lines) for different liquids obtained in 90° scattering geometry with NA = NA′ = 0.03. Individual spectra have been normalised to the central Rayleigh peak. Experimental data points for methanol (dots) are also shown for comparison. Each spectrum was acquired using a 2 second exposure time and a HeNe laser providing 10 mW at the sample plane.

with the resulting computational fit. All spectra are normalised with respect to the mean intensity of the central Rayleigh peak. Particular attention was taken during the sample preparation in order to avoid liquid contamination by parasite agents such as dust. For this purpose, a micropipette was used to transfer small quantities of liquid into the glass cuvette. Each sample was maintained at room temperature ($T \sim 24°C$). Spectra were acquired with an integration time of 2 seconds with a laser power of 10 mW at the sample plane. For this measurement only, a HeNe laser ($\lambda = 632.8$ nm) was used due to the unavailability of the Cobolt Jive laser. Appendix B illustrates the individual raw spectra of the liquids processed with the

least-squares Lorentzian fittings. Brillouin frequency shifts relative to the central Rayleigh peak are in good agreement with the theoretical values, as illustrated in Table 4.1. Theoretical values of the frequency shifts were calculated from equation

| | $\nu_B$ exp. (GHz) | $\nu_B$ theo. (GHz) | $V$ (m/s) |
|---|---|---|---|
| Methanol | $3.26 \pm 0.06$ | 3.39 | 973.8 |
| Benzene | $4.92 \pm 0.07$ | 4.38 | 1301.1 |
| Ethanol | $3.47 \pm 0.04$ | 3.48 | 1012.1 |
| Toluene | $4.43 \pm 0.08$ | 4.26 | 1174.7 |
| Water | $4.43 \pm 0.08$ | 4.41 | 1341.5 |

**Table 4.1:** Experimental and theoretical values of the Brillouin frequency shift for different liquids as found from spectra acquired in a 90° scattering geometry at room temperature with $\mathrm{NA} = \mathrm{NA}' = 0.03$.

2.10, in which the scattering angle was assumed to be $\psi = 90° \pm 2°$. The values for the refractive indexes $n$ were specified by the supplier ($VWR$), whilst values for the hypersound velocity were taken from previous studies [101, 128, 132, 133].

## 4.2 Spectral Broadening in Brillouin Imaging

To date, Brillouin imaging has only been used with low numerical aperture microscope objectives [47, 52]. Primarily, this restriction arises in an attempt to limit spectral broadening of the Brillouin peaks, and hence loss of spectral resolution, associated with collection of photons over a wide range of scattering angles [130, 134, 135, 136]. Both frequency shift and linewidth of the lorentzian distribution governing the Brillouin spectrum are uniquely determined by the medium and the angle relative to the incident and scattering k-vectors. Acquisition of photons of different frequencies over finite illumination and collection NA leads to spectral broadening and shape distortion of the Brillouin peaks. This phenomenon is responsible for a dramatic decrease in the spectral resolution and thus in the localisation accuracy of the inelastic spectral lines. Low NA lenses limit the achievable spatial resolution. Although a natural limit on the achievable spatial resolution is imposed by the acousto-optic interaction length (usually of the order of 1 $\mu$m) due to the finite lifetime of the acoustic phonons [71], significant advances towards this fundamental

limit can be made if higher NA optics can be employed.

Hitherto, correction formulae for the true linewidth and frequency shift have been suggested by Danielmeyer for different shapes of the collection aperture [137]. In another model, specific Voigt functions have been applied to correct for the instrumental broadening [130]. Furthermore, a method to reduce the effects of aperture broadening has been proposed by Gigault *et al.* through the placement of rectangular slits at the collection lens [138]. Nevertheless, these analyses have been carried out in two dimensions only, without approaching a more rigours treatment of the spectral broadening in three dimensions, i.e. in the case of real illumination and collection apertures.

In this section a description of the spatial resolution of an imaging system is given. The inherent trade-off between spatial and spectral resolution in Brillouin imaging setups employing high NA lenses is therefore investigated.

### 4.2.1 Numerical Aperture and Spatial Resolution

Before analysing the broadening mechanisms affecting the Brillouin spectrum, it is of interest to first understand how the numerical aperture of an imaging system determines its spatial resolution.

In order to derive a criterion characterising the spatial resolution of an imaging system, the field distribution of a circular aperture needs to be investigated. Diffraction theory states that the amplitude distribution of a plane wave focused by a circular thin lens of radius $a$ and focal length $f$ is given by the integral [65]

$$U_f(r,z) = -\frac{ik\exp(ikf)}{f}\exp\left(\frac{ik}{2f}r^2\right)\int_0^a \exp\left(-\frac{ikz}{2f^2}\rho^2\right)J_0\left(\frac{k\rho r}{f}\right)\rho\mathrm{d}\rho, \qquad (4.3)$$

where $J_0$ is the zero order *Bessel function* of the first kind. We shall investigate the intensity distributions that arise along the longitudinal and transverse directions, which will ultimately determine the natural spatial resolution of an imaging system. In the on-axis case, i.e. when $r = 0$, $J_0(0) = 1$ and $\exp(0) = 1$ so that, with an appropriate change of variables, equation 4.3 reduces to

$$U(0,z) = \left(\frac{k}{2f}\right)\left(\frac{2f^2}{kz}\right)\exp(ikf)\left[\exp\left(-i\frac{kz}{2f^2}a^2\right) - 1\right]. \qquad (4.4)$$

The intensity distribution along the propagation axis is thus given by

$$I(0,z) = |U(0,z)|^2 = \left(\frac{a^2 k}{2f}\right)^2 \operatorname{sinc}^2\left(\frac{u}{4}\right), \tag{4.5}$$

where

$$u = k(\mathrm{NA})^2 z \tag{4.6}$$

is known as the *axial normalised optical co-ordinate* and

$$\mathrm{NA} = n \sin\alpha \tag{4.7}$$

is the lens numerical aperture. Figure 4.6 shows a diagram of a circular thin lens of radius $a$ and focal length $f$ which focuses a plane wave represented by a collimated beam. The angle of convergence $\alpha = \tan^{-1}(a/f)$ observed in the graph determines

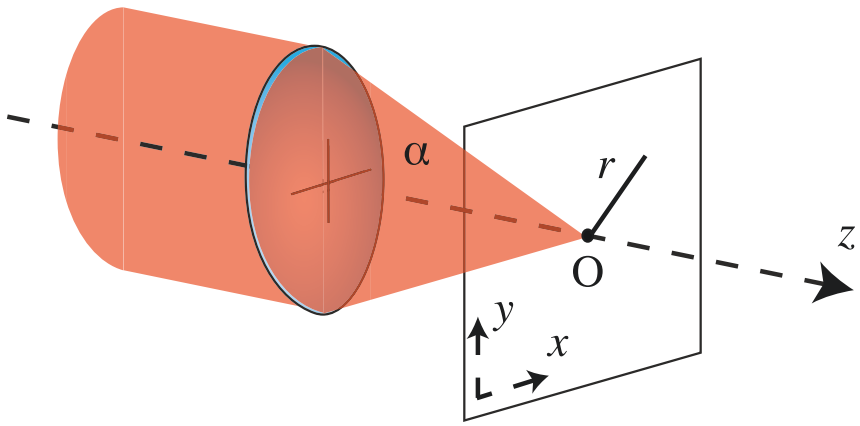



**Figure 4.6:** Collimated beam focused by a circular lens of radius $a$ and focal length $f$. The NA of the lens in air ($n = 1$) is defined by the angle $\alpha = \tan^{-1}(a/f)$.

the lens NA. The positive zeros of the distribution expressed in equation 4.5 occur at

$$u/4 = m\pi, \qquad |m| = 1, 2, \ldots, \tag{4.8}$$

which recalling equation 4.6 can be solved for $z$ to give

$$z = \frac{2m\lambda}{(\mathrm{NA})^2}, \qquad |m| = 1, 2, \ldots \tag{4.9}$$

The first positive and negative minima of the axial intensity distribution of equation 4.5 ultimately define the *depth of field* (DOF) of the imaging system, which is expressed as

$$z_{DOF} = \frac{4\lambda}{\mathrm{NA}^2}. \tag{4.10}$$

Equation 4.10 provides an estimate of the width of the central region within which the intensity does not fall to zero.

When $z = 0$, the amplitude distribution at the focal plane of the thin lens is given by

$$U(r,0) = -\frac{ik}{2f}\exp(ikf)\exp\left(ik\frac{r^2}{2f}\right)a^2\left(\frac{2J_1(v)}{v}\right), \tag{4.11}$$

where the first order Bessel function $J_1(v)$ and the *transverse normalised optical co-ordinate*

$$v = k\mathrm{NA}r \tag{4.12}$$

have been introduced. The transverse intensity distribution is now expressed as

$$I(r,0) = |U(r,0)|^2 = \left(\frac{ka^2}{2f}\right)^2\left(\frac{2J_1(v)}{v}\right)^2, \tag{4.13}$$

with the first positive minimum occurring at $\nu = 3.832$. The width $d$ of the central distribution is therefore defined as

$$d = 1.22\frac{\lambda}{\mathrm{NA}}. \tag{4.14}$$

Figure 4.7 illustrates the longitudinal and transverse intensity distribution as a function of the optical co-ordinates $u$ and $v$. The transverse distribution is typically known as the *Airy distribution*, which describes the intensity profile at the image plane of an object located at infinity. In two dimensions, the central spot defined by the first dark ring is known as the *Airy disk*. In a perfect imaging system, i.e. a system which is not affected by optical aberrations, approximately 84% of the total intensity is contained in the Airy disk.

The intensity distributions obtained in equations 4.5 and 4.13 set the basis of the formulation of a fundamental criterion defining the spatial resolution of an imaging system. This states that two point objects can be resolved if the intensity maximum

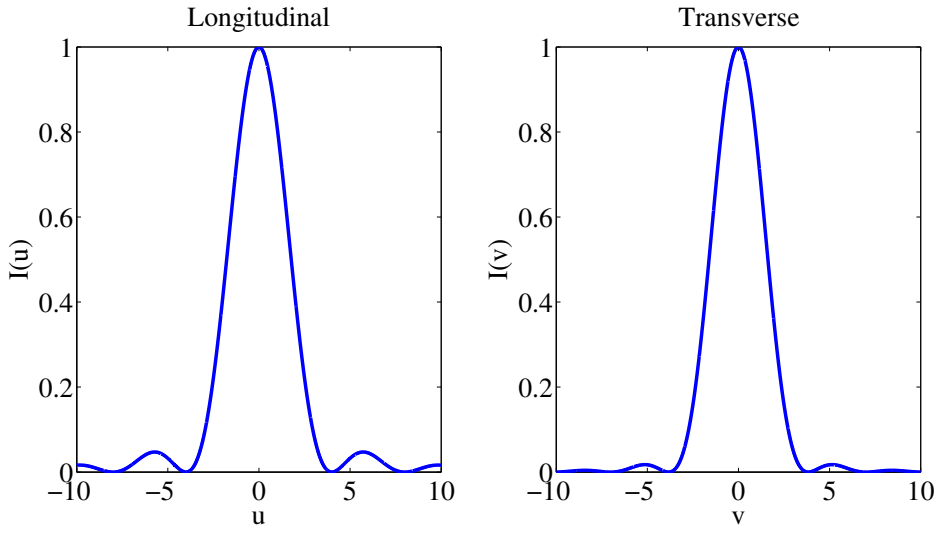



**Figure 4.7:** Longitudinal (left) and transverse (right) intensity distribution at the focal region of a perfect thin lens.

of one point coincides with the first intensity minimum of the distribution associated with the second point. In other words, two objects can be distinguished by an incoherent imaging system if they are separated by a minimum distance of

$$z = \frac{2n^2\lambda}{\mathrm{NA}^2}, \tag{4.15}$$

along the optical axis, and

$$r = 0.61\frac{\lambda}{\mathrm{NA}}, \tag{4.16}$$

in the transverse plane. This statement is known as the *Rayleigh criterion*. It follows that the higher the NA, the greater the spatial resolution of an imaging system.

Since the range of scattering angles defined by the system NAs determines the broadening of the Brillouin spectrum, a rigorous investigation of the optimal arrangement was necessary to obtain high spatial resolution Brillouin imaging.

### 4.2.2 Spectral Distribution for High NAs

In order to determine the optimal geometry to use in the design of a high resolution Brillouin imaging system, a rigorous treatment of spectral broadening arising from

the use of high NA optics is performed. In particular, the two limiting cases of both a $\Psi = 90°$ and a $180°$ scattering geometry are investigated.

With reference to Figure 4.8, we consider light propagating in direction

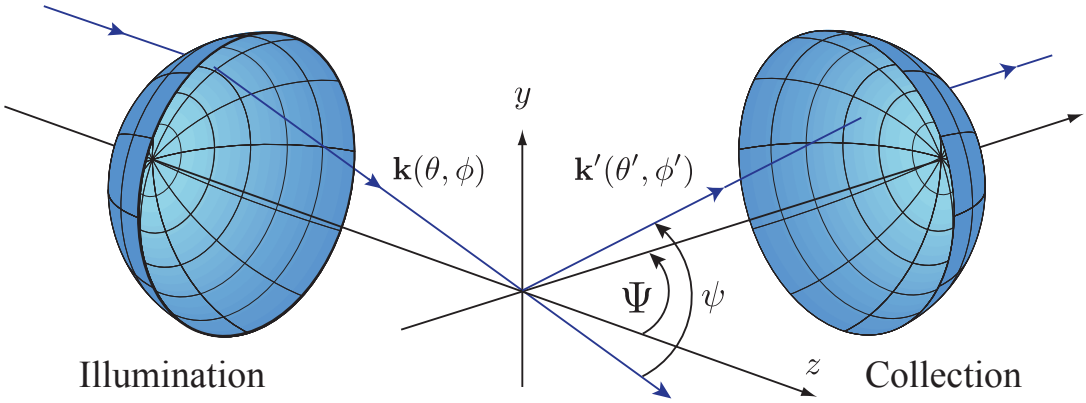



**Figure 4.8:** Schematic of scattering geometry showing the Gaussian reference spheres for illumination and collection lenses. The direction of incident and scattered photons are defined by the wave-vectors $\mathbf{k}(\theta, \phi)$ and $\mathbf{k}'(\theta', \phi')$ respectively.

$$\hat{\mathbf{k}} = \begin{pmatrix} \sin\theta\cos\phi \\ \sin\theta\sin\phi \\ \cos\theta \end{pmatrix} \tag{4.17}$$

incident upon a scattering medium. Upon inelastic scattering through an angle $\psi$, the scattering field propagates in direction

$$\hat{\mathbf{k}'} = \begin{pmatrix} \sin\theta'\cos\phi' \\ \sin\theta'\sin\phi' \\ \cos\theta' \end{pmatrix}. \tag{4.18}$$

As described in Section 2.4, conservation of energy and momentum dictates that the scattered field due to acoustic phonons is shifted in frequency by

$$\nu_B(\psi) = 2\nu_0(n/c)V\sin(\psi/2), \tag{4.19}$$

where $\nu_0$ is the frequency of the incident photon, $n$ is the refractive index of the medium, $c$ is the speed of light and $V$ is the acoustic velocity in the scattering

medium [71]. The finite lifetime of acoustic phonons implies a frequency broadening such that the associated Brillouin spectral peak has a linewidth of

$$\Delta\nu_B(\psi) = \frac{4\eta\nu_0^2 n^2}{\pi\rho c^2}\sin^2(\psi/2), \tag{4.20}$$

where $\eta$ and $\rho$ are the viscosity and density of the material [71]. The use of finite NA optics, however, implies the photons scattered over a range of

$$\psi = \cos^{-1}[\hat{\mathbf{k}}\cdot\hat{\mathbf{k}}'] \tag{4.21}$$

all contribute to the observed signal. Accordingly the Brillouin spectral line is formed from the incoherent superposition of many individual peaks with displaced maxima and differing widths. The total linewidth of the Brillouin peak is determined by the inherent Brillouin broadening $\Delta\nu_B$ and range of shifts $\nu_B$ present, however, typically $\Delta\nu_B \ll \nu_B$ such that we can neglect the former. Collection of photons scattered over a small range of scattering angles, $\delta\psi$, therefore gives rise to a range of Brillouin shifts, $\delta\nu_B$, which all contribute to the total observed peak, such that to first order the spectral broadening scales as [126]

$$\delta\nu_B \approx \frac{d\nu_B(\psi)}{d\psi}\Big|_{\psi=\Psi}\delta\psi \propto \cos(\psi/2)\,\delta\psi \tag{4.22}$$

where $\Psi$ is the average scattering angle. Noting that

$$\frac{d\nu_B(\psi)}{d\psi}\Big|_{\psi=\pi} = 0 \tag{4.23}$$

suggests that *the spectral broadening effects arising from use of finite NA optics are minimised in a back-scattering geometry.*

We note that the incident and scattered directions can be defined by positions on the surface of the Gaussian reference spheres associated with the illumination and collection lenses (Figure 4.8) [139]. Specifically, we must then integrate the spectral profiles, $s(\nu,\psi)$, obtained for all possible scattering angles over the associated solid

angles

$$S(\nu) = \int_{\Omega}\int_{\Omega'} s(\nu,\psi)\; d\Omega d\Omega', \tag{4.24}$$

where the inherent spectrum of acoustic waves propagating in liquids is known to be well described by a Lorentzian profile of the form

$$s(\nu,\psi) = \frac{(\Delta\nu_B(\psi)/2)^2}{(\nu-\nu_0 \pm \nu_B(\psi))^2 + (\Delta\nu_B(\psi)/2)^2}, \tag{4.25}$$

with the $\pm$ sign taken for the anti-Stokes and Stokes components respectively [137]. Equations 4.24 and 4.25 give the total Brillouin spectrum arising from the detection of acoustic phonons with finite NA. We shall now investigate the two limiting scattering geometries, $\Psi = 90°$ and $180°$, so to provide analytical expressions for numerical evaluation of equation 4.24.

In the case of a backscattering geometry, i.e. for $\Psi = 180°$, the k-vectors product defining the scattering angle $\psi$ gives

$$\hat{\mathbf{k}}\cdot\hat{\mathbf{k}}' = -\left[\sin\theta\sin\theta'\cos(\phi-\phi') + \cos\theta\cos\theta'\right], \tag{4.26}$$

where the minus sign is due to the opposite propagation direction of the scattered wave with respect to the incident plane wave travelling along the $\hat{z}$ direction. By substituting equation 4.25 in 4.24 and with an appropriate choice of the integral limits, we obtain

$$S(\nu)_{180} = \int_0^{\theta}\int_0^{2\pi}\int_0^{\theta'}\int_0^{2\pi} \frac{(\Delta\nu_B(\psi)/2)^2}{(\nu-\nu_0 \pm \nu_B(\psi))^2 + (\Delta\nu_B(\psi)/2)^2}\; d\theta d\phi d\theta' d\phi', \tag{4.27}$$

which gives the total spectral distribution arising in a backscattering geometry of finite NA. On the other hand, a change of variables is applied when $\Psi = 90°$ so that

$$\begin{aligned} x &\longmapsto y' \\ y &\longmapsto z' \\ z &\longmapsto x' \end{aligned} \tag{4.28}$$

and the scattering k-vector becomes

$$\hat{\mathbf{k}}'\left(\beta(\theta',\phi'),\ \gamma(\theta',\phi')\right) = \begin{pmatrix} \cos\beta \\ \sin\beta\cos\gamma \\ \sin\beta\sin\gamma \end{pmatrix}. \tag{4.29}$$

Following this substitution the k-vectors product in 90° scattering geometry now gives

$$\hat{\mathbf{k}}\cdot\hat{\mathbf{k}}' = \sin\theta\cos\phi\cos\beta + \sin\theta\sin\phi\sin\beta\sin\gamma + \cos\theta\sin\beta\sin\gamma, \tag{4.30}$$

whilst the spectrum of the Brillouin scattered light collected in such configuration can be evaluated by the integral

$$S(\nu)_{90} = \int_0^{\theta}\int_0^{2\pi}\int_0^{\beta}\int_0^{2\pi} \frac{(\Delta\nu_B(\psi)/2)^2}{(\nu-\nu_0\pm\nu_B(\psi))^2+(\Delta\nu_B(\psi)/2)^2}\, d\theta d\phi d\beta d\gamma. \tag{4.31}$$

Equations 4.27 and 4.31 are two analytical expressions describing the total Brillouin spectrum arising through finite illumination and collection NA in the limiting cases of both a 180° and 90° scattering geometry.

### 4.2.3 Computational and Experimental Results

The Brillouin spectrum of several liquids was numerically integrated for a full range of NA. Figure 4.9 shows an example calculation for Brillouin scattering (via an anti-Stokes process) from a liquid benzene sample. The spectral intensity (normalised to the Rayleigh peak) is shown on a logarithmic scale as a function of the illumination and collection NA (which were taken to be equal). It should be noted that the total collected power scales as the product of the illumination and collection solid angles, i.e. $\Omega$ and $\Omega'$, where $\Omega^{(\prime)} = 2\pi(1-\cos\alpha^{(\prime)})$, as depicted in the inset of Figure 4.9. Table 4.2 gives values for the viscosity $\eta$, density $\rho$, acoustic velocity $V$ and refractive index $n$ of benzene which were taken into account in the present analysis. For reference, the theoretical Brillouin shifts for a 90° and 180° scattering geometry with NA $\approx 0$ are $\nu_B^{90} = 4.48$ GHz and $\nu_B^{180} = 6.19$ GHz respectively.

For the 90° geometry, the Brillouin peak is subject to a dramatic broadening as

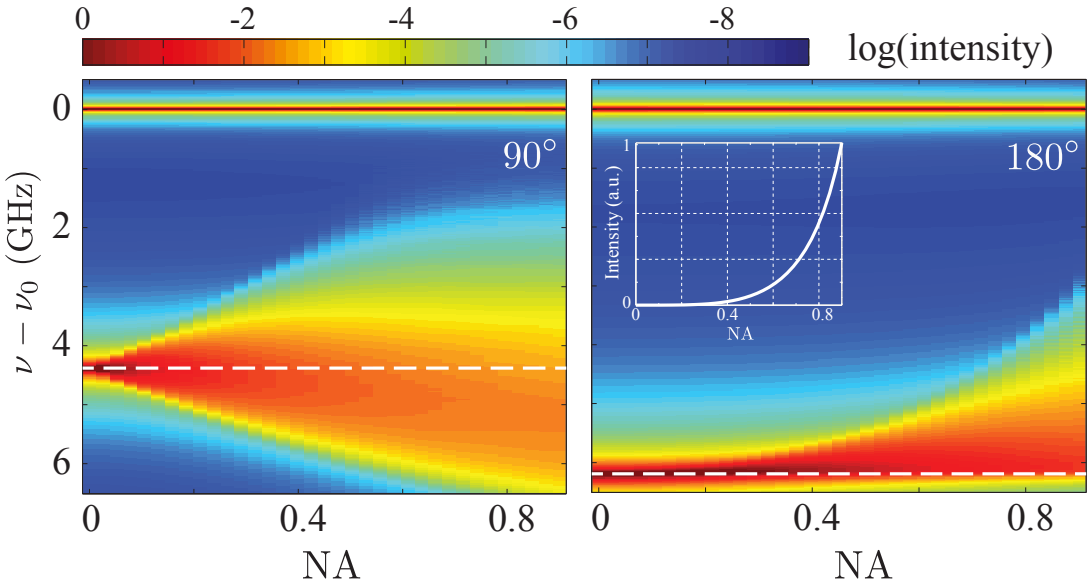



**Figure 4.9:** Logarithmic spectral intensity as a function of NA for scattering from liquid benzene in a 90° (left) and 180° (right) geometry. The spectrum is normalised to the peak Rayleigh intensity at each NA. White dashed lines show the theoretical position of the Brillouin peak for NA = 0. (Inset) Total integrated intensity as a function of NA.

| $\eta$ (g cm$^{-1}$ s$^{-1}$) | $\rho$ (g cm$^{-3}$) | $V$ (m s$^{-1}$) | $n$ |
|---|---|---|---|
| $0.652 \times 10^{-2}$ | 0.876 | 1276.4 | 1.5 |

**Table 4.2:** Liquid benzene thermodynamic parameters.

the NA is increased. Furthermore, the Brillouin peak noticeably changes in shape from its inherent Lorentzian profile leading to a substantial blueshift in the central frequency with respect to $\nu_B^{90}$. This is clearly seen in Figure 4.10 which shows an overall displacement of roughly 18% in the peak position in the frequency domain. Naive use of equation 4.19 would therefore lead to significant errors in determination of the acoustic velocity of phonons, and thus of the elasticity moduli of the material in any realistic experimental study. Figure 4.10 also illustrates the broadening of the FWHM of the Brillouin peak as a function of NA. An order of magnitude increase in $\Delta\nu_{\text{tot}}$ over a full aperture is observed, implying a significant degradation in the overall spectral resolution. The Rayleigh peak remains constant in width and centred at the incident frequency $\nu_0$ for all NA as expected. However, for the 180° backscattering geometry, a narrower Brillouin peak is obtained. Again the Rayleigh peak is subject to neither spectral broadening or shifts as the system NA is varied.

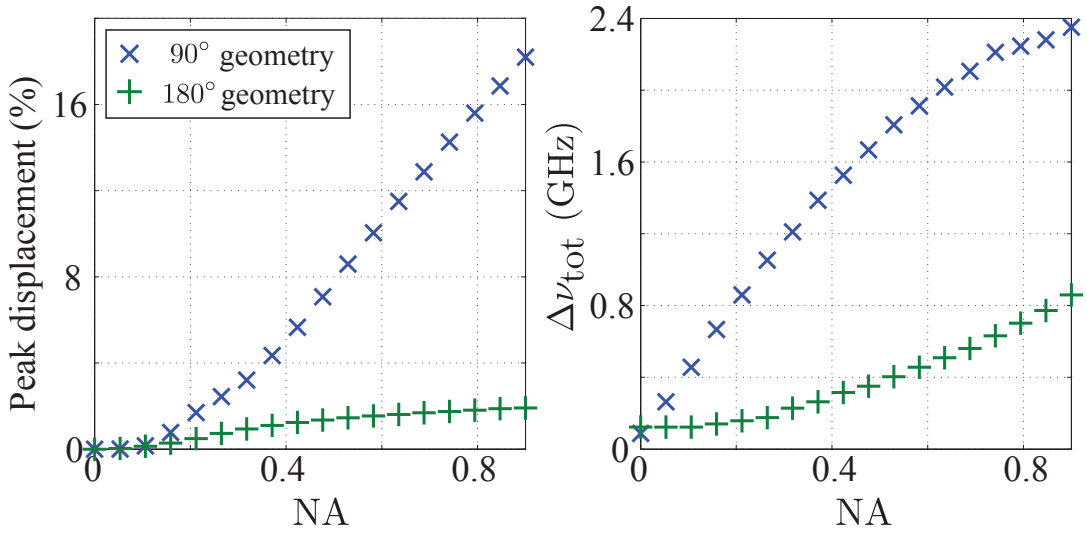



**Figure 4.10:** Relative shift of Brillouin peak from $\nu_B^{90,180}$ (left) and FWHM (right) as a function of the NA (left).

In Figure 4.10 the Brillouin peak FWHM $\Delta\nu_{\mathrm{tot}}$ is seen to remain below 1 GHz even for NAs close to unity. Shifts of the apparent Brillouin peak are also reduced by approximately an order of magnitude. Similar results are also found when assuming a liquid methanol sample.

Experimental data were first acquired for $\Psi = 90°$ with the optical arrangement described in Figure 4.1. Brillouin spectra of liquid benzene for a range of NAs were recorded by varying the radius $r_l$ of the expanded laser beam by means of a diaphragm $D'$ placed behind $L_{\mathrm{ill}}$. The NA of the collection arm was held constant at $\mathrm{NA}' = 0.13$. The same procedure was applied in a backscattering arrangement where the illumination and collection were performed by the same lens. In this case, a dark-field configuration was used to minimise detection of surface reflections. Specifically, an annular illumination was used whilst the scattered radiation was collected through the central region of the pupil. Figure 4.11 shows the variation of the measured anti-Stokes Brillouin peak linewidths $\Delta\nu_{\mathrm{inst}}$ for a range of NAs for both scattering geometries. Each spectrum was acquired with an integration time of 5 minutes. Theoretical values, depicted by the solid black lines, were determined by calculating the integrated spectrum of liquid benzene, obtained from equation 4.24, convolved with the instrumental function of the VIPA. Following Oliver [134] and

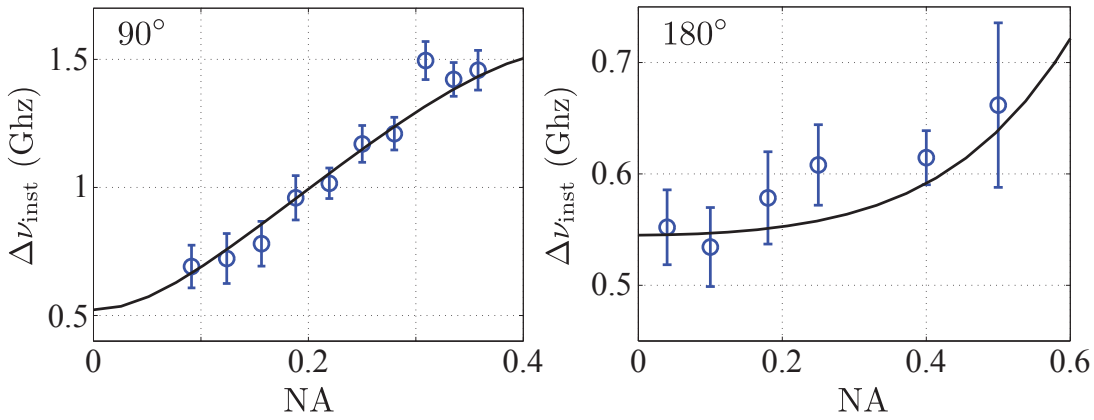



**Figure 4.11:** Brillouin peak linewidth measurements (blue circles, with accompanying error bars) as a function of the NA for $\Psi = 90°$ (left) and $\Psi = 180°$ (right). Black solid curves depict theoretical predictions.

La Macchia [130], the instrumental function was taken as a Lorentzian function with FWHM matching the elastic Rayleigh peak. This method requires the spectral bandwidth of the laser to be small, as is the case for a single longitudinal mode laser. From Figure 4.11 the resulting spectral linewidth is seen to increase by $\sim 1$ GHz for $\Psi = 90°$ whilst it does not vary significantly for $\Psi = 180°$. Experimental results show good agreement with theory. The superiority of the backscattering geometry is clearly seen, suggesting that Brillouin peaks can be localised and resolved for high NA systems utilising this geometry.

In summary, in this section we have analysed the effects of finite instrumental apertures on experimental Brillouin spectra, with a view to high NA Brillouin imaging. By integrating over finite pupil geometries we have shown that broadening effects could be minimised by use of a backscattering geometry. Furthermore, deformation of the Lorentzian line shape of the Brillouin peak was shown to arise from use of high NAs such that the peak maximum is shifted relative to the low NA case. These effects were again shown to be minimised in a backscattering geometry. Experimental verification of these predictions followed using a 90° and 180° Brillouin dark-field microscope setup. Our results show that whilst the common practice of use of low NA lenses in a 90° scattering geometry is necessary to minimise angular broadening and spectral distortion, these effects are far less apparent in a backscattering geometry. High NA (NA $> 0.5$) lenses can, therefore, be used with limited

consequences in such a geometry. Our analysis can further provide accurate evaluation of suitable fitting functions since spurious frequency shifts can be obtained due to fittings by symmetric lineshape [135]. Moreover, deconvolution of real data with our theoretical models may eventually give an estimate of the inherent spectral linewidths of the Brillouin peaks. This would allow the imaginary part of the longitudinal elastic modulus $M''$ to be measured. Ultimately, Brillouin imaging with both high spatial and spectral resolution, hitherto thought unfeasible, was hence a realistic proposition.

## 4.3 Dark-Field Brillouin Microscopy

Dark-field microscopy refers to a range of imaging techniques which aim to provide a significant contrast enhancement by suppressing specular reflections. In contrast with conventional bright field microscopes, typical dark-field systems employ specific geometries that enable collection of only the scattered light. Consequently, a significant increase in the imaging contrast is obtained when investigating unstained or transparent specimens. This concept was considered applicable to Brillouin imaging in an attempt to optically minimise collection of the elastic light, which would prevent the formation of parasitic crosstalk affecting the measurement of the Brillouin spectra.

A large number of dark-field techniques employ annular beams illuminating the objective lens, hence forming a cone of light when focused to the sample. Besides standard annular masks, annular beams are typically generated by either axicon lenses [140, 141] or helical phase masks [142, 143, 144]. Unlike conventional spherical lenses, axicons are characterised by a conical surface so that a point object is imaged into a line along the optical axis [145]. On the other hand, phase masks are designed to introduce a helical retardation to the wavefront of the beam which in turn results in an annular shape through a self-interference process [146]. The "donut" beam is focused to the sample by a condenser lens and a coaxial microscope objective is used to collect only the scattered light due to the divergence of the illumination beam from the optical axis [147]. Alternatively, a single microscope objective can be used for both illumination and collection. In this case, since a reciprocal annular beam is

formed after collection of surface reflections, a circular spatial mask can be centred along the optical axis so as to allow transmission of the scattered light [148]. Optical reflections are rejected by the circular spatial mask placed in the optical path before detection.

Other dark-field techniques based on dual-axis arrangements have been demonstrated to perform high-resolution *in vivo* imaging by means of different illumination and collection lenses separated by an angle $\theta$ [53, 149]. When the angle formed by the illumination beam direction and the optical axis exceeds the *critical angle*, light undergoes total internal reflection. The critical angle $\theta_c$ is defined as

$$\theta_c = \sin^{-1}(n_2/n_1), \tag{4.32}$$

where $n_2 < n_1$ are the refractive indexes at the interface of the sample plane, which is typically formed by a glass coverslip on one side and the sample substrate on the other. Although total internal reflection occurs, an electromagnetic field known as the *evanescent wave* is formed along the interface normal $\hat{z}$ direction [150]. This wave propagates a small distance along the interface plane and is governed by an exponentially decaying intensity along the $\hat{z}$ direction given by

$$I(z) = I_0 e^{-z/d}, \tag{4.33}$$

where $d$ is the depth of the evanescent field typically of the order of many tens of nm. The shallow depth of the intensity profile has encouraged the development of Total Internal Reflection Microscopy (TIRM), which benefits from the evanescent wave in achieving a substantial imaging contrast enhancement [151]. This has enabled significant progress in life science where the fluorescence signal is acquired for spectral imaging and analysis. The excitation process of the fluorophores labelling the sample is constrained by the depth of the evanescent field, hence leaving the deeper molecules in the ground energy state [152, 153]. For this reason, TIRM has seen extensive use in super-resolution imaging techniques such as Photoactivated Localization Microscopy (PALM) and Stochastic Optical Reconstruction Microscopy (STORM) where background fluorescence needs to be minimised. This allows a greater accuracy in the localisation process of single fluorescent molecules to be

achieved [154, 155].

Following the analysis on the spectral broadening due to instrumental apertures, a confocal backscattering dark-field microscope was designed. The following section describes the optimal arrangement when using an annular beam illumination, which was generated by a custom made prism. Preliminary results on Brillouin imaging of liquid interfaces obtained with the dark-field microscope are presented.

### 4.3.1 Dark-Field Arrangement

A confocal dark-field setup was adapted to an *Olympus IX71* inverted microscope. Figure 4.12 shows the optical arrangement. The linearly polarised laser beam

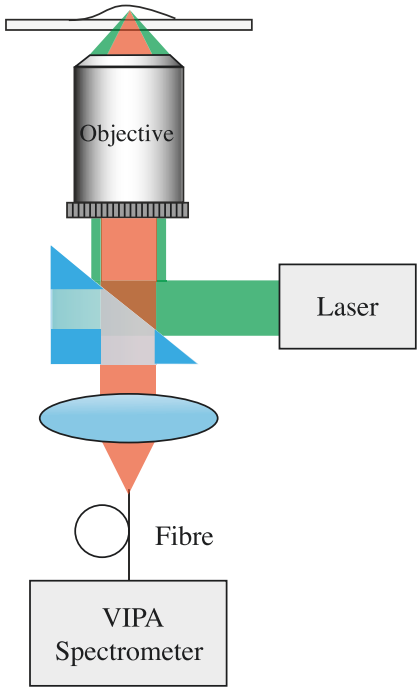



**Figure 4.12:** Dark-field microscope diagram. An annular beam was generated by means of a customised prism. Illumination and collection occurred with the same microscope objective. A SM fibre ensured strict confocality and flexible beam delivery to a single-stage VIPA spectrometer.

($\lambda = 561$ nm) was first expanded to fill the objective lens aperture. A shear plate interferometer was used to ensure high quality of the collimated beam after the expansion. An axicon lens was originally considered ideal to yield an annular-shaped

beam without significant loss of power. However, given the high manufacturing costs of such a lens, a different approach was taken where a customised prism was made to reflect the outer region of the expanded collimated beam at 45°. *SolidWorks* images of the prisms side views are illustrated in Figure 4.13. The prism was drilled on

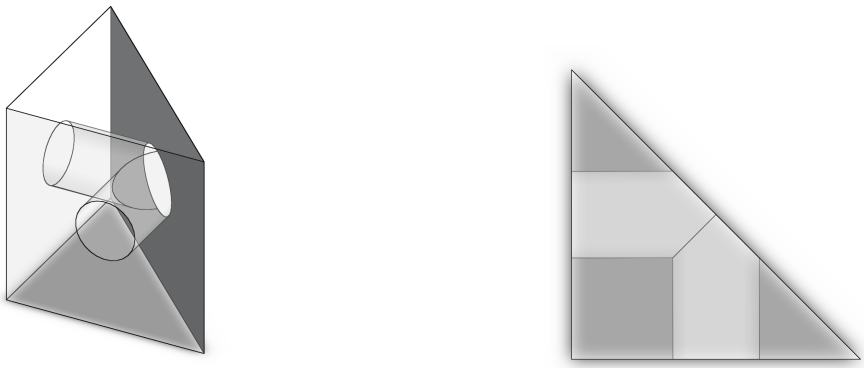


**Figure 4.13:** Three dimensional (left) and 2D top-down (right) representation of the 45° angled prism designed with the engineering software *SolidWorks*. The front surface was polished and coated with silver to maximise reflectivity.

two sides so as to yield two concentric holes on the opposite surface, which was first polished and then coated with silver in order to maximise reflectivity. The intensity distribution of the beam after reflection was a Gaussian distribution truncated at the central region. The resulting annular beam was focused to the sample plane by means of an infinity corrected Olympus microscope objective lens of NA=0.5. The light scattered from the sample was collected through the centre of the same lens along the optical axis. The prism allowed the scattered radiation to pass through one hole whilst reflecting back the specularly reflected light. Next, a lens of NA=0.25 was employed to couple the scattered light into a single mode fibre with a coupling efficiency of $\sim 60\%$. The fibre enabled confocality and a flexible beam delivery to the spectrometer. In the present setup, a single stage VIPA was used as described in Section 3.2.1. Finally, the Andor sCMOS camera was used to detect the spectral pattern.

### 4.3.2 Annular Beam Illumination Optimisation

As previously discussed, an axicon lens would allow all the incident light to be focused on a ring pattern, hence providing maximum power delivery to the sample. Conversely, only a fraction of the laser beam is reflected by the customised prism resulting in a weaker scattering signal. Furthermore, the use of a single microscope objective for both annular illumination and central collection gives a lower effective numerical aperture with respect to that associated to a uniform illumination and collection on a clear aperture.

In order to optimise the system performance, both transverse and longitudinal intensity distributions were analysed by assuming an incident plane wave as a first approximation. The optimal aspect ratio of the annular-shaped beam that maximises the throughput efficiency was investigated.

Since the intensity distribution of the laser beam is Gaussian, the resulting beam profile after the prism reflection could be associated to that of a Gaussian distribution truncated at the central region. Consequently, the beam size at the prism was investigated by assuming an Gaussian beam profile. The optimal beam size was associated with the beam radius giving the maximum fraction of incident power delivered to the sample.

#### 4.3.2.1 Transverse and Longitudinal PSF

Let $a$ be the inner and $b$ the outer radius of the annular beam, as shown in Figure 4.14. Assuming an objective lens of aperture radius equal to $b$, we want to estimate the aspect ratio, which is the ratio of the inner and outer radius ($a/b$) of the annular beam, that optimises the efficiency of the imaging system. In order to proceed with the analysis, the system point spread function (PSF) of the imaging system needs to be taken into account. The PSF describes the response of an imaging system to a point source. The total response is given by the product of the illumination and collection PSF [65], so that

$$\mathrm{PSF} = \mathrm{PSF}_{ill} \cdot \mathrm{PSF}_{coll}. \tag{4.34}$$

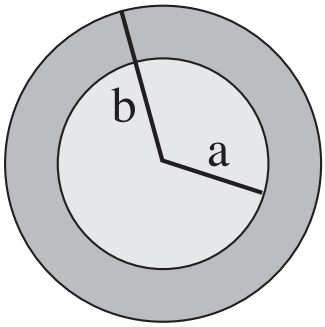



**Figure 4.14:** Annular illumination diagram. The outer radius $b$ coincides with aperture radius of the microscope objective. Collection occurs through the central region of the same lens defined by the radius $a$.

In the case of a perfectly coherent optical system of circular apertures, the PSF is expressed by the field distributions described in Section 4.2.1. Under such circumstances, the amplitude distribution of the annular illumination can be evaluated by subtracting the relative amplitudes given by two circular apertures of radius $b$ and $a$ respectively [156]. Recalling equation 4.11, the illumination field distribution at the focal plane is thus given by

$$U_{ill}(r,0) = U_b(r,0) - U_a(r,0) \simeq b^2 \left( \frac{2J_1(krb/f)}{krb/f} \right) - a^2 \left( \frac{2J_1(kra/f)}{kra/f} \right), \quad (4.35)$$

where the complex phase terms are neglected under the assumption that the two regions are in phase. Since the scattered light is collected through the central region of the pupil defined by the inner radius $a$ of the illumination, the collection field distribution can be expressed as

$$U_{coll}(r,0) = U_a(r,0) \simeq a^2 \left( \frac{2J_1(kra/f)}{kra/f} \right). \quad (4.36)$$

In a similar approach, starting from equation 4.4, the illumination distribution for the on-axis case ($r = 0$) can be derived as

$$U_{ill}(0,z) = U_b(0,z) - U_a(0,z) \simeq \exp\left( -i \frac{kz}{2f^2} b^2 \right) - \exp\left( -i \frac{kz}{2f^2} a^2 \right), \quad (4.37)$$

whilst the distribution at collection is

$$U_{coll}(0,z) = U_a(0,z) \simeq \left[\exp\left(-i\frac{kz}{2f^2}a^2\right) - 1\right]. \tag{4.38}$$

The total intensity distribution of the annular dark-field imaging system is given by

$$I_{tot}(r,0) = |U_{ill}(r,z) \cdot U_{coll}(r,z)|^2_{z=0} \tag{4.39}$$

for the in-focus case, whilst along the optical axis this yields

$$I_{tot}(0,z) = |U_{ill}(r,z) \cdot U_{coll}(r,z)|^2_{r=0} \tag{4.40}$$

Figure 4.15 shows the normalised intensity distributions for a dark-field imaging system in both transverse and longitudinal directions. The obtained graphs correspond

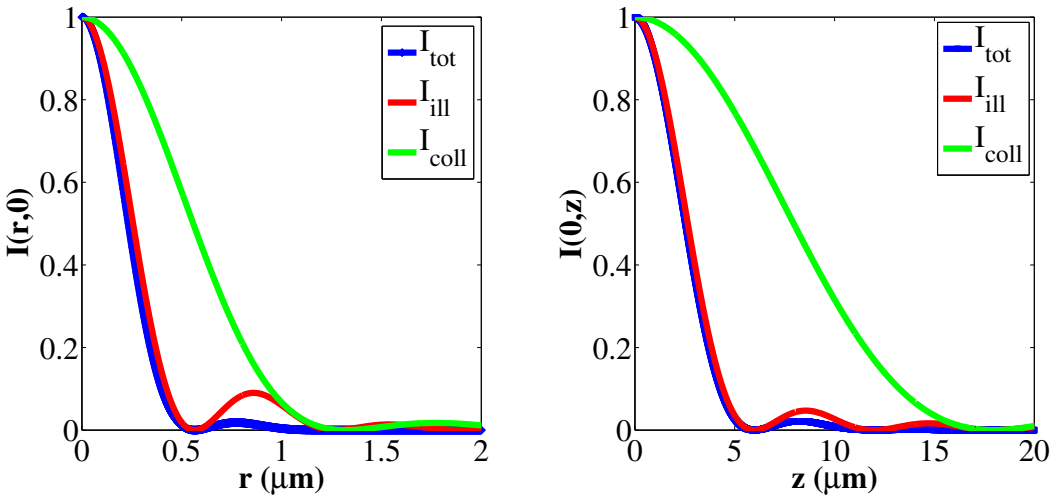



**Figure 4.15:** Normalised intensity distributions along the transverse (left) and longitudinal (right) directions for a lens of NA=0.5. The total intensity is compared with the illumination and collection distributions. First minimum of the longitudinal distribution appears an order of magnitude larger than in the transverse case.

to a microscope objective of NA = 0.5 and aperture radius $b = 4$ mm. In order to perform a qualitative analysis, the inner radius of the illumination ring was assumed to be half of the outer ($a = b/2$). The left hand side plot compares the total transverse intensity distribution to that given by the annular illumination ($I_{ill} = |U_{ill}|^2$)

and the collection ($I_{coll} = |U_{coll}|^2$). As it can be seen, a narrower central distribution of the total intensity with respect to both collection and illumination distributions is obtained. The intensity at the second maximum of the illumination profile is higher than that of the total intensity. Furthermore, the plots show roughly an order of magnitude increase in the width of the central longitudinal intensity distribution defined by the first positive and negative minima with respect to that associated with the transverse distribution. As can be observed in the right hand side plot, the second maxima of the illumination and total intensity distributions are now closer. Collection intensity profiles are broader due to the lower effective NA defined by the radius $a = b/2$.

A transverse resolution of $r \simeq 0.5$ $\mu$m and a longitudinal resolution of $z \simeq 6.2$ $\mu$m were evaluated. It must be noted that whilst the transverse resolution of the dark-field system is higher than that defined by the Rayleigh criterion for a full aperture, longitudinal resolution is significantly lower. This is not surprising as in the case of an infinitely narrow annulus beam focused by a lens, a Bessel beam characterised by an infinite depth of field would be generated [157].

#### 4.3.2.2 Annular Beam Aspect Ratio

In order to investigate the throughput efficiency of the optical arrangement, the total power collected by the system was considered as the integral of the intensity distribution in two dimensions, which in the in-focus case was expressed as

$$P_{tot}(r, 0) = \int_0^{2\pi} \int_0^{\infty} I_{tot}(r, 0)\, r \mathrm{d}r\, \mathrm{d}\theta. \tag{4.41}$$

Numerical evaluation of the integral expressed by equation 4.41 was performed for a full range of values of the annular aspect ratio ($0 \leq a/b \geq 1$). Figure 4.16 shows a plot of the total power collected by the system as a function of $a/b$. The graph shows that the efficiency of the dark-field imaging system is maximised for $a/b \simeq 0.66$. Consequently, a microscope objective of aperture radius $b = 4$ mm imposed the inner radius of the illumination ring to be $a \simeq 2.6$ mm. This value was used as the hole radius of the 45° customised prism to generate the donut beam and simultaneously allowing the scattered light to be collected.

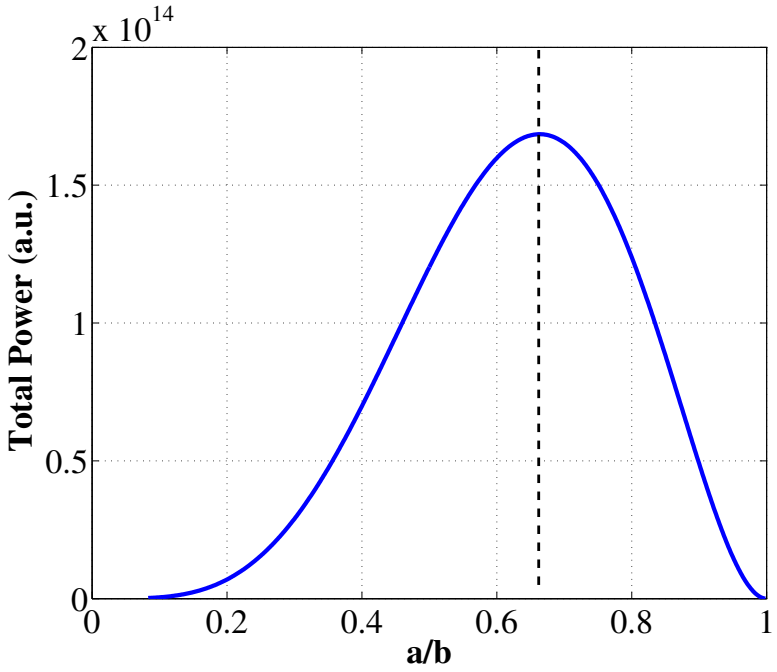



**Figure 4.16:** Total power collected by the dark-field system for different ratios of the inner and the outer radius of the annular illumination beam. The curve shows that the optimal performance is given by $a/b \simeq 0.66$.

#### 4.3.2.3 Power Assessment

The intensity profile of the laser beam can be approximated to a Gaussian distribution. Consequently, the reflection off the prism yields a Gaussian beam distribution truncated at the central region. Given the optimal aspect ratio of the annular illumination, the fraction of the incident light reflected is determined by the beam size at the prism. This was investigated to estimate the maximum power delivered to the sample.

Assuming an incident Gaussian beam, the normalised intensity profile at the prism can be described by a Gaussian distribution of the form

$$I(r) = \exp\left(-\frac{2r^2}{w^2}\right), \tag{4.42}$$

where $w$ is the beam radius at which the intensity drops to $1/e^2$. After reflection,

only a fraction of power $P_{ab}$ remains in the annulus, which is given by

$$P_{ab} = \frac{P_b - P_a}{P_{tot}}, \tag{4.43}$$

where

$$P_{a(b)} = \int_0^{2\pi} \int_0^{a(b)} I(r)\, r\mathrm{d}r\, \mathrm{d}\theta \tag{4.44}$$

and

$$P_{tot} = \int_0^{2\pi} \int_0^{\infty} I(r)\, r\mathrm{d}r\, \mathrm{d}\theta. \tag{4.45}$$

In order to find the optimal beam size that maximises the amount of light reflected by the prism and transmitted through the exit pupil of radius $b = 4$ mm, equation 4.43 was evaluated for a range of values of the beam radius $w$. The results are shown in Figure 4.17, where the percentage of power delivered to the sample is plotted as a function of the ratio $w/b$. The graph shows that a maximum fraction

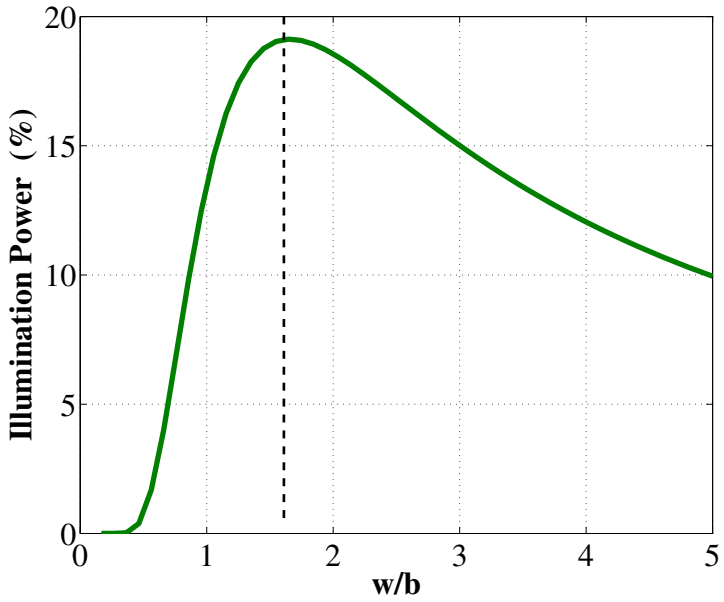



**Figure 4.17:** Percentage of power delivered to the sample as a function of the ratio $w/b$. The power is shown to be maximised for a laser radius of $w \simeq 1.6b$.

of power of $\sim$ 19% is obtained for $w/b \simeq 1.6$, which in our case gives a beam radius of $w = \simeq 6.6$ mm. Assuming an output laser beam of radius $w_0 \sim 0.35$ mm, a magnification of $M = 18.5$ was therefore imposed. It must be noted that the

percentage estimated in the analysis did not take into account the reflectivity of the prism surface, which for a silver coating is approximately 92% at $\lambda = 561$ nm.

### 4.3.3 Data Acquisition and Image Processing

In order to acquire data and generate an image based on the Brillouin spectral information obtained from a sample, several computational codes were written. A *LabView* program was developed to synchronise electronic instrumentations employed in the system. This involved communication with a *Prior Scan III* motorised stage, the Andor sCMOS camera and the Cobolt laser, which were all connected to the same PC. The motorised stage mounted on the microscope had a minimum step size of 0.04 $\mu$m in the $\hat{x}$ and $\hat{y}$ directions. The step size defines the minimum distance travelled by the stage between two adjacent points across the sample. An incorporated mechanical device allowed the same displacement along the $\hat{z}$ direction by adjusting the distance between the microscope objective and the sample. A three dimensional image could be generated by scanning over the sample with high repetition accuracy.

A code was created to move the stage along the three directions with adjustable step size, speed and acceleration. An appropriate choice of both speed and acceleration of the motorised stage was required to avoid mechanical damage when setting short steps (e.g. $< 1\,\mu$m) and to ensure minimal shaking of the sample mounted on the platform. Furthermore, the LabView software enabled recognition of the absolute values indicating the stage location for additional position feedbacks. A frame acquisition after each step movement was taken with the sCMOS camera. The camera integration time, area of interest (AOI) and dynamic range (12 to 16 bits) could be set before proceeding with the acquisition process. Once the camera was initialised, a cooling sensor brought the detector to the desired temperature down to -40°C. Once the desired temperature was reached, the data acquisition could start. In order to ensure that the camera did not acquire any data whilst the stage was moving, the software was instructed to return a release command as soon as the stage stopped moving at each iteration. Each frame was automatically saved on the PC server and labeled with the corresponding iteration number for processing. Moreover, in order to minimise the amount of memory required for the entire im-

age acquisition, the camera AOI was minimised to the spectral region of maximum signal intensity set by the Gaussian envelope of the illumination, as described in Section 3.2.1. This area centred on a single Brillouin doublet involved $200 \times 200$ pixels on the camera. A display allowed the option for real-time monitoring of the frames acquired. In order to accelerate the acquisition process, both the motorised stage and camera were initialised as a first step and then closed at the end of the entire data acquisition rather than recalling them at each iteration. The camera buffer was filled and emptied after each frame acquisition. Frames were saved as Portable Network Graphics (.png) files.

Image reconstruction was performed by a homebuilt Matlab code. This recognised the frame label number to identify the corresponding index of the image array. Each frame followed the fitting process described in Section 4.1.1 in order to retrieve values for the frequency shift and linewidth of the Brillouin spectrum. Finally, an image showing the spatial stiffness distribution could be obtained by converting values of the frequency shift into Brillouin modulus using equation 2.22. Once the image was reconstructed in false RGB colours, final adjustments involved contrast and illumination visual optimisation.

## 4.4 Dark-Field Imaging

Preliminary images were acquired in order to test the performance of the dark-field microscope and to verify that collection of surface reflections was minimised. A *USAF Test Resolution* target was used as the object, which was scanned by means of the motorised microscope stage and a frame was acquired at each scan position, as previously described. Each frame contained a single spectrum of the scattered light collected from the probe volume. Figure 4.18 shows the dark-field images of an arbitrary symbol taken across the USAF test target. The image was acquired by scanning across the USAF plate with a discrete step size of 5 $\mu$m and a frame rate of 100 Hz for a total acquisition period of roughly 40 minutes. Each spectrum was fitted and the resulting intensity of the Rayleigh peaks was measured. An image of the intensity of the elastically scattered light was thus generated after processing. The object appears to be dark apart from the bright edges. In fact,

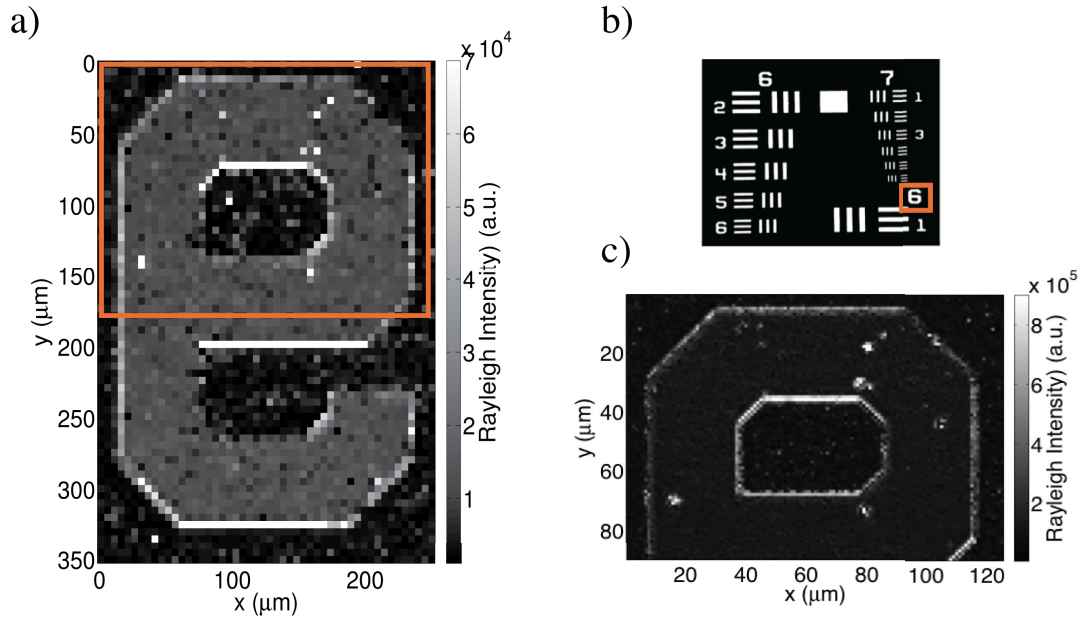



**Figure 4.18:** Dark-field image of an object taken with stage steps of 5 $\mu$m (a). USAF test resolution target used as a sample across the number 6 (b). Image of a small region of the same object taken with stage steps of 2 $\mu$m (c). Only the edges of the images (a) and (c) are bright because of the absence of surface reflections at detection.

a greater amount of elastic scattering was expected at the edges as opposed to the polished, smooth regions of the sample. As a consequence, the contrast was given by the almost complete absence of surface reflections detected by the camera. Conversely, this contrast would be lost in conventional bright field arrangements where the scattered light is overwhelmed by the specularly reflected light. Another acquisition (Figure 4.18 c) across a smaller region of the same specimen was taken to assess the repetition accuracy of the microscope. This time, a scan step of 2 $\mu$m was applied. Similar small features of the sample were identified in both images, hence giving good confidence on the robustness and repeatability of the imaging system, including the software being developed.

It must be noted that the acquisitions were performed with step size greater than the diffraction limit. The reason why the object was under-sampled was the need to reduce the total data acquisition time, which otherwise would have been substantially longer.

### 4.4.1 Preliminary Brillouin Imaging

Having assessed the performance of the dark-field system, the microscope was addressed to acquire Brillouin spectral images.

Transparent materials, such as polystyrene and liquids, were considered appropriate to perform a first test on Brillouin imaging due to the low amount of elastic scattering. Figure 4.19 compares the Brillouin image of a two-liquid interface to the associated dark-field image. In a similar procedure used by Koski and Yarger [47],

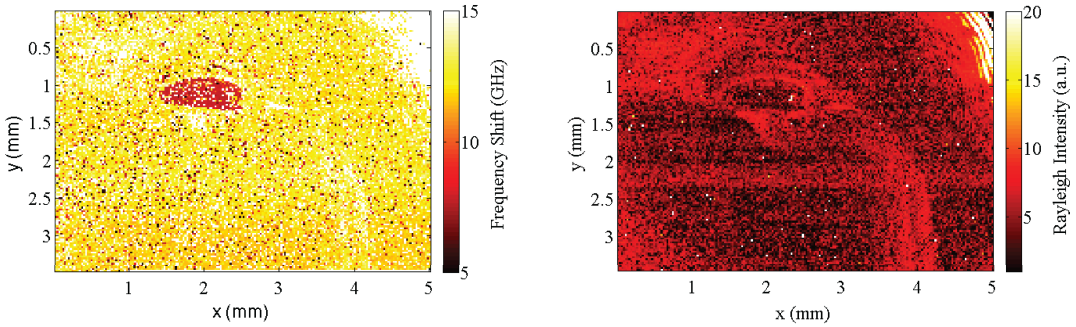



**Figure 4.19:** Brillouin image of two-liquid interface (left) and associated dark-field image (right). The water drop (red spot) can be distinguished from the oil in the Brillouin image only.

oil and water were used as the liquid samples due to their immiscibility. The two liquids were put together at room temperature ($\sim$ 24°C) in a transparent dish by means of a micropipette. The silica dish was sealed to avoid dust contamination and placed on the microscope stage to focus the laser beam at the two-liquid interface and perform the scan. The camera integration time for a single frame was set to 1.6 seconds with 10 mW laser power at the sample plane and 25 $\mu$m step size. Consequently, the data acquisition time required about 14 hours to yield a Brillouin image of $\sim$ 15 mm$^2$ sample area.

The left hand side image of Figure 4.19 is the Brillouin image in false colour of the liquid interface. A high imaging contrast was given by the difference in the measured frequency shift of the Brillouin scattered light of the two liquids, which could be clearly distinguished. Conversely, in the associated dark-field image (right hand side image of Figure 4.19) showing the intensity of the central Rayleigh peak,

the contrast between the two liquids was lost due to the equal amount of elastic light scattered.

Figure 4.20 shows a linescan of both the Brillouin frequency shift and the spectral linewidth measured along the interface between oil and water. The measured Bril-

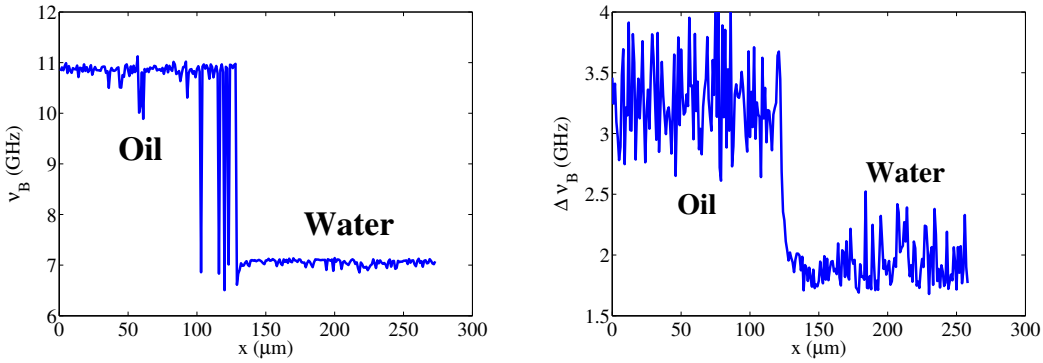



**Figure 4.20:** 1D spatial distribution of the frequency shift (left) and the linewidth (right) of the Brillouin peaks along the two-liquid interface.

louin frequency shift was $\nu_B = (7.09 \pm 0.11)$ GHz for water and $\nu_B = (10.85 \pm 0.13)$ GHz for oil, which gave an acoustic velocity of $V_{water} = 1495.3 \pm 8.4$ m/s and $V_{oil} = 2008.9 \pm 9.6$ m/s respectively. These values showed good agreement with previous reports [47]. Experimental values for the spectral linewidth were $\Delta\nu_B = (1.88 \pm 0.23)$ GHz for water and $\Delta\nu_B = (3.29 \pm 0.32)$ GHz for oil, which showed an order-of-magnitude broadening with respect with previous analyses [47]. This is mainly caused by the instrumental broadening which affects the peak linewidth even at low NA, as illustrated in Section 4.2.

To summarise, a dark-field optical arrangement was employed as a suitable method to minimise undesired specular reflections. An annular beam was generated by means of a customised prism to illuminate the sample. The next step was to investigate the aspect ratio of the annulus that optimised the system performance. The beam size at the prism giving the highest throughput efficiency was estimated. The imaging system was first tested with an arbitrary sample to ensure minimal collection of surface reflections. Next, preliminary Brillouin images were acquired mainly using liquid interfaces.

Overall, the microscope showed a good performance even though the data acqui-

sition time was relatively long. This represented the major instrumental limitation since a shorter integration period was required for the microscope to address real biological applications.

## 4.5 Confocal Brillouin Microscopy

The annular illumination used in the Brillouin dark-field microscope was an efficient method to optically minimise collection of surface reflections allowing the isolated scattered radiation to be detected. This was particularly important when employing a single-stage VIPA spectrometer limited by an extinction ratio of roughly 30 dB. Although the intensity of the system PSF was maximised through an appropriate choice of the annular beam size with respect to the aperture radius, the integration time required to acquire a single Brillouin spectrum of liquids was longer than one second. Since most unfixed biological samples have a limited lifetime before a change in their mechanical properties occurs, a decrease of at least one order of magnitude in the acquisition times was necessary. Besides the weak scattering signal at detection, the dark-field arrangement also suffered from an elongated longitudinal intensity distribution, as shown in Figure 4.15. In order to overcome these limits, a full scanning confocal system was built on the microscope.

The following section describes the principles of a scanning confocal imaging system and the final optical arrangement used for fast high spatial resolution Brillouin microscopy.

### 4.5.1 Principles of Confocal Imaging

A confocal microscope, first proposed by Nipkow and then designed by Minsky in 1957 to image high density neuronal tissues [158], is an optical microscope that uses a spatial filter to suppress the out-of-focus light collected from the sample [159, 160]. Light emitted by a point source is detected by a point detector, as shown in Figure 4.21. An intermediate plane conjugate to the sample plane is used to spatially filter the light emitted from any other point objects in space. A spatial filter consists of a pinhole whose diameter is typically set to be equal to the width size of the central intensity distribution formed at the intermediate plane. For a

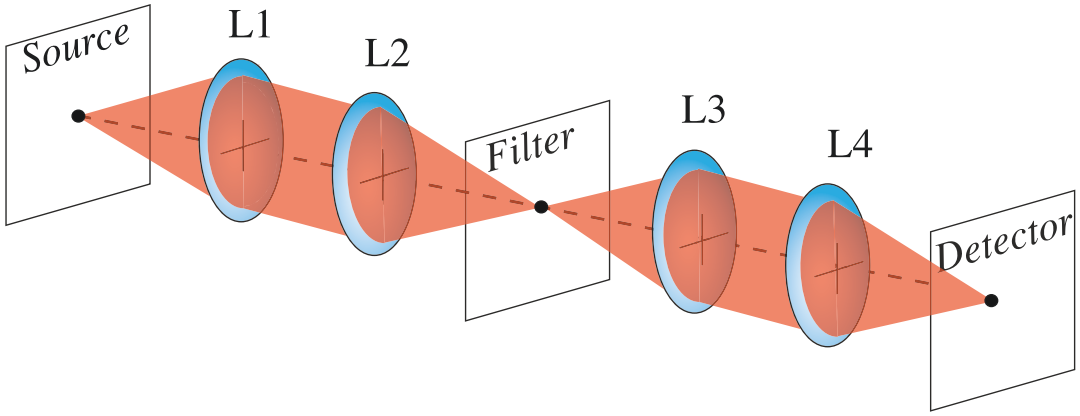



**Figure 4.21:** Diagram of a confocal system. A point source emits light which passes through a spatial filter placed at an intermediate conjugate plane so to remove the out-of-focus radiation. This allows a greater axial resolution to be achieved compared to that given by conventional bright field microscopes. After [161].

perfect imaging system, the width of the PSF at the conjugate plane is given by the product of the diffraction limited spot diameter at the object plane and the relay system magnification defined as

$$M = \frac{f_2}{f_1}, \tag{4.46}$$

where $f_1$ and $f_2$ are the effective focal lengths of the lens L1 and L2 respectively. Although a pinhole is typically employed in confocal microscopy, single-mode optical fibres can also perform as spatial filters providing a coherent detection and more flexibility to the beam delivery. Nevertheless, whilst a pinhole returns the same polarisation of the incoming light, optical fibres generally suffer from temperature and stress fluctuations which lead to significant variations of the polarisation state of the output field [161].

The spatial filter allows an optical imaging system to achieve a significant improvement in the axial resolution with respect to that given by conventional bright field microscopes, where the sample is entirely illuminated. A single objective lens can act as a condenser and simultaneously collects light from the sample. Figure 4.22 illustrates the intensity distributions given by a confocal imaging system with and without annular illumination. The intensity distributions correspond to a microscope objective of NA $= 0.5$ together with the optimised aspect ratio of the annular illumination ($a/b \simeq 0.66$). The width of transverse distribution obtained with the

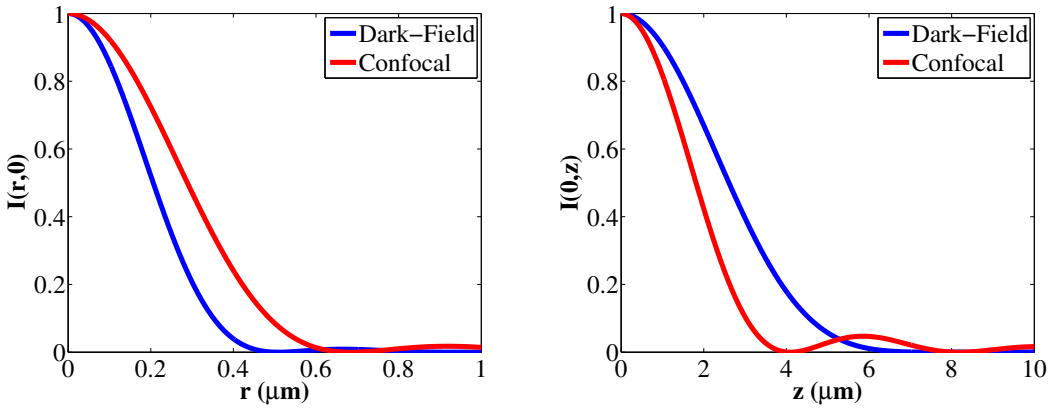



**Figure 4.22:** Transverse (left) and longitudinal (right) intensity distributions of a confocal imaging system characterised by a plane wave (red) and an annular dark-field (blue) illumination.

dark-field arrangement is $\sim 25\%$ narrower than that of the confocal system. On the other hand, the longitudinal intensity profile results to be $\sim 50\%$ broader than that given by a confocal system uniformly illuminated, as shown in the right hand side of Figure 4.22.

The higher the NA at illumination of a confocal imaging system, the smaller the scattering volume. In highly heterogeneous samples, such as biological specimens, a small probe volume results in weak elastic signals due to smoother refractive index variations experienced by the beam in that sample volume [162, 163].

### 4.5.2 Confocal Optical Setup

Figure 4.23 shows the final confocal arrangement used to perform fast high spatial resolution Brillouin imaging. The objective lens is illuminated by a collimated Gaussian beam emitted by the single longitudinal mode laser ($\lambda = 561$ nm). A half wave plate ($\lambda/2$) placed at the laser output allowed rotation of the linear polarisation state of the input field. The beam was first expanded by a factor of 10 to fill the aperture of the microscope objective. Half of the input optical power was delivered to the objective lens by means of a 50/50 beam splitter (BS), which resulted in a higher throughput efficiency with respect to the dark-field setup. In order to minimise surface reflections at the sample plane and simultaneously increase the spatial

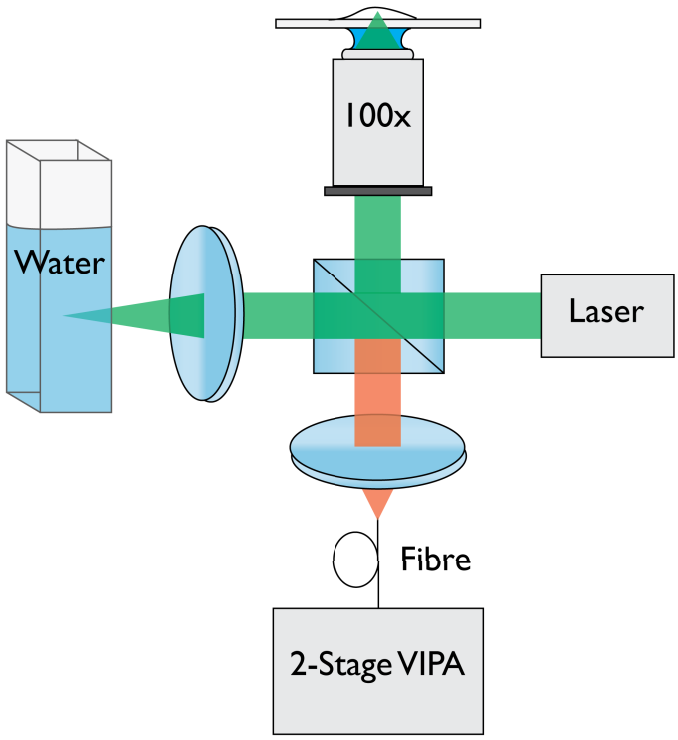



**Figure 4.23:** Final confocal arrangement for fast high resolution Brillouin imaging. A two-stage VIPA spectrometer was employed to ensure high spectral contrast. A reference signal from water is taken to measure the frequency shift of the Brillouin spectra during the processing.

resolution of the imaging system, an oil immersion *Olympus UPlanFLN* microscope objective of NA = 1.3 and 100x magnification was employed. The oil inserted in between the lens and the coverslip ensured a smoother transition in the refractive index than that provided by an air-glass interface. Using equations 4.15 and 4.16 the longitudinal and transverse resolution of the confocal system were estimated $z = 1.51\,\mu$m and $r = 0.26\,\mu$m respectively. The scattered light is coupled back to the SM fibre by a second objective lens (NA = 0.25). The two-stage VIPA spectrometer described in Section 3.3 was employed in the microscope to spectrally resolve the Brillouin signal. An extinction of 60 dB was considered sufficient to separate the weak Brillouin peaks from the crosstalk arising from semitransparent biological samples.

As described in the previous chapter, the spatial masks located at the intermediate planes of the spectrometer were used to suppress most of the elastic light so

as to enhance the visibility of the Brillouin peaks detected by the sCMOS camera. Consequently, since the location of the elastic peaks could not be taken as a reference for the measurement of the frequency shift, another approach was taken. Specifically, the laser beam transmitted through the BS was focused into the glass cuvette filled with distilled water, which was used as a new reference signal. Before proceeding with the scanning of the sample, the system was calibrated with one frame acquisition of the Brillouin spectrum of water. This was taken by blocking the illumination arm of the inverted microscope in order to avoid detection of light coming from the sample. Water has a well known bulk modulus of $B = 2.2$ GPa [25, 83, 164] which made it suitable to use as a spectral reference. In the backscattering geometry this gives a Brillouin frequency shift of $\nu_B = 7.04$ GHz. This value was taken as a reference to measure the frequency shift of the Brillouin spectra acquired at each sampling point across the samples.

The confocal arrangement described was ultimately employed to acquire mechanical images of several biological samples such as tissues and cells.

# Chapter 5

# High Resolution Brillouin Imaging

---

The confocal Brillouin microscope was used to investigate two different biological problems: on the one hand the stiffness variations in specific endothelium cells of the eye, aiming at a better understanding of the mechanisms responsible for *glaucoma*, and on the other the characterisation of the mechanical structures of blood vessels, which could provide fundamental information regarding the formation of atherosclerotic plaques.

In this chapter, these results are presented. The Brillouin modulus of both PDMS gels and silicon rubber sheets of different stiffnesses was measured. Correlation plots suggest the existence of a linear relationship between the Brillouin modulus and the standard Young's modulus, thus validating the technique as a reliable method for measuring stiffness. To the best of our knowledge this thesis presents, for the first time, sub-cellular Brillouin microscope images. Specifically, stiffness images of single Human Umbilical Vein Endothelial Cells (HUVEC) cells and blood vessel cross sections were acquired. These results may establish confocal Brillouin microscopy as the tool of choice for artery wall measurements, in particular when atherosclerotic plaques are formed.

## 5.1 Young's Modulus Correlation

Before proceeding with the investigation of the mechanical properties that regulate biological systems, a validation of the technique as a reliable method to measure stiffness was necessary.

As mentioned in Section 2.5, previous studies have found the Brillouin modulus to be linearly related with the standard Young's modulus [54]. In order to provide an independent proof of this dependency and thus demonstrate that the Brillouin modulus is related to the material stiffness, several measurements were taken with the confocal system described in Section 4.5. In particular, both PDMS gels and semitransparent silicon rubber sheets were tested. PDMS gels were in-house made by Dr Sietse Braakman with stiffness varying from 5 kPa to 60 kPa. A standard uniaxial rheometer was used to measure the Young's modulus of the gels. This device measures the shear force using a load cell applied to the sample under test. Silicone rubber sheets were provided by *Silex Ltd* with a known Young's modulus ranging $E = (1 - 6)$ MPa.

Figure 5.1 shows the correlation plots between Brillouin modulus and Young's modulus. The Brillouin modulus was measured 10 times for each sample with an

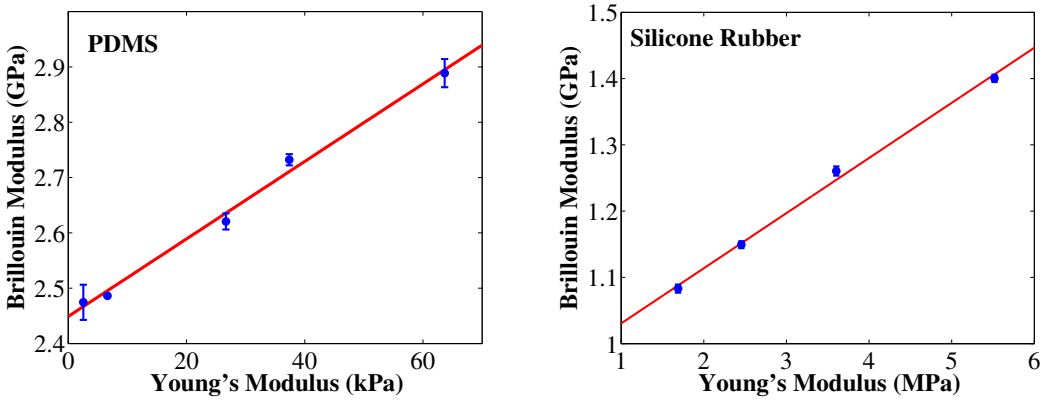



**Figure 5.1:** Measured Brillouin modulus as a function of the Young's modulus for PDMS gels (left) and silicon rubber sheets (right). The fits suggest that the two moduli are linearly correlated. However, the results show that the linear relationship varies depending on the material.

exposure time of 1 second. The least-squares fits suggest the existence of a lin-

ear relationship between Brillouin modulus and Young's modulus, which endorses Brillouin spectroscopy as a reliable method to measure stiffness. Although a linear correlation holds for both PDMS gels and silicone rubber sheets, the results show that this varies depending on the material properties, and ultimately represents a fundamental aspect that needs further investigation.

## 5.2 Cell Mechanics in Glaucoma

Glaucoma is an asymptomatic eye disease affecting about 60 million people worldwide. A late diagnosis of the disease can bring irreversible damages such as low vision and blindness. Glaucoma is typically associated with elevated *intraocular pressure* (IOP), which refers to the fluid pressure inside the eye. Currently, there is little understanding of why IOP becomes elevated in glaucoma or how to best reduce it to preserve vision. Recent studies have focused on the endothelial cells lining Schlemm's canal (SC), which serves as a collection vessel for aqueous humour drainage from the eye. The resistance of this drainage is increased in glaucoma and determines IOP [165]. Consequently, understanding the mechanism of this resistance generation lies at the heart of understanding and treating the disease. The key data are:

- SC cells are mechanosensitive, and form micron-sized pores (openings through the endothelial monolayer) in response to mechanical load. This is important because these pores provide a pathway for flow to enter the SC, where the mechanical loads *in vivo* are regulated by the pressure gradient arising from aqueous humour drainage. The SC endothelium therefore acts as a biomechanically regulated filtration barrier.

- glaucomatous SC cells form fewer pores than normal SC cells. This was directly observed in glaucomatous eyes by means of a novel cell culture model that mimics the SC barrier dysfunction in glaucoma [11].

- recent AFM measurements have shown that glaucomatous Schlemm's canal cells are stiffer than normal cells by approximately $\sim 50\%$. Nevertheless, AFM is primarily sensitive to cortical stiffness rather than to cytoplasmic stiffness,

which appears elevated in glaucoma [166]. The cytoplasmic stiffness can only be measured indirectly by comparing the AFM data to multi-phase FE models of the cell. Confirming these findings using an independent and non-invasive method would be of great interest.

In the following section, high resolution Brillouin images of single HUVEC cells are presented. Preliminary analyses have demonstrated that Brillouin microscopy has the potential to support the AFM data by directly measuring differences in the cytoplasmic stiffness between normal and glaucomatous SC cells. Hitherto we have proved that when *Latrunculin-A* drug is applied directly to the endothelial cells, the stiffness decreases as suggested by previous AFM analyses [166, 167]. The results encourage further investigations on cell mechanics for a better understanding of the mechanisms that lead to glaucoma.

### 5.2.1 Cell Culture

HUVEC cells stem from the endothelium of veins in the umbilical cord and are commonly used in pathological practises to investigate the origin of diseases derived from the endothelial layer. These were considered suitable for preliminary *in vitro* mechanical imaging. The cells were cultured by Dr Sietse Braakman in a dish filled with *phosphate buffered saline* (PBS) solution, which is a water-based salt solution that is isotonic and non-toxic to cells and has the ability to maintain their osmolarity. The Brillouin modulus of PBS was measured to be $M' = 2.91 \pm 0.14$ GPa, which is comparable to that of water ($M' \simeq 2.2$ GPa).

The HUVEC cells were deposited on a thin gelatin film (9% w/v) placed on top of the glass coverslip, as illustrated in Figure 5.2. A gelatin film of $n \simeq 1.38$ was used to yield a smoother variation in the refractive index across the interface that divides the glass coverslip ($n \simeq 1.5$) and the cells, which were assumed to have the same refractive index as water ($n \simeq 1.33$) [168, 169]. The larger the difference in the refractive indexes at the sample interface, the higher the amount of optical reflections arising at that plane. Since the thickness of the human cells is typically a few microns [170, 171, 172], which is of the order of magnitude of the microscope depth of field, the gelatin film was necessary to prevent formation of strong crosstalk at the sample plane.

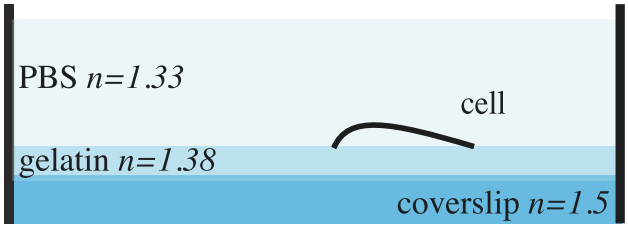



**Figure 5.2:** Sample dish diagram. Cells were cultured in a PBS buffer solution. A gelatin film of $< 50\,\mu$m thickness was spin coated on top of the coverslip so as to reduce the refractive index mismatch at the sample interface.

The deeper the penetration of the probe beam inside the gelatin film along the optical axis, the greater the amount of spherical aberrations affecting the system [173]. In order to minimise the film thickness and simultaneously ensure a high degree of surface flatness, the gel was spin coated on top of the coverslip. The resulting thickness of the gelatin film was estimated to be below $50\,\mu$m, which was sufficient to avoid significant signal attenuation due to spherical aberrations. This was confirmed by Zemax simulations that measured a Strehl ratio of $0.93 \pm 0.05$.

### 5.2.2 *In vitro* Single Cell Mechanical Imaging

Although standard AFM indentation methods can estimate the stiffness of the cell cortex by tip compression, these cannot measure the elasticity of the cytoplasm or the nucleus. Moreover, the spatial resolution is determined by the tip size, which in most biological applications is limited to a few microns. On the other hand, the confocal Brillouin microscope is capable of retrieving mechanical properties optically, therefore providing 3D mechanical mapping in a non-invasive manner.

Figure 5.3 shows the Brillouin image of a single HUVEC cell in false RGB colour. To the best of our knowledge, this represents the first sub-cellular elasticity image acquired to date. Data acquisition required an integration period of 0.7 sec/frame with a laser power of approximately 10 mW at the sample plane. Frames were acquired with $0.5\,\mu$m step size. The sample was further sectioned along the $\hat{z}$ direction with a scan step of $1\,\mu$m. Since the thickness of the HUVEC cells is within the range of $3 - 5\,\mu$m, a three dimensional scan was performed to allow the laser beam to gradually approach the inside of the cell cortex. Consequently, the cytoplasmic

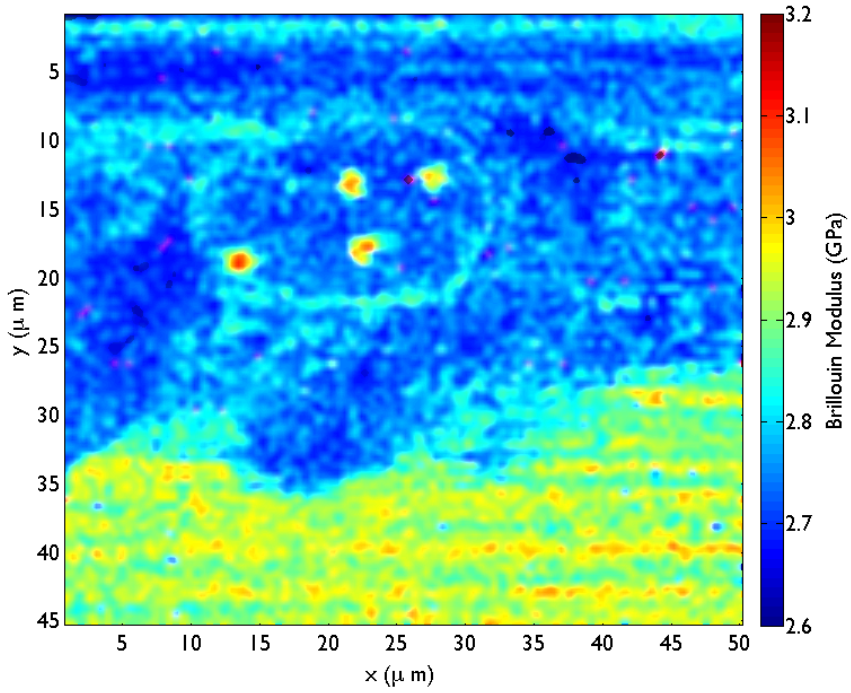



**Figure 5.3:** Brillouin image of a single HUVEC cell. Both the nucleus membrane and the four nucleoli can be identified and appear to have a higher stiffness than the surrounding cytoplasm.

content was ensured to be optically probed and spatially mapped. A water density of $\rho = 1000$ Kg/m$^3$ was used when measuring the Brillouin modulus through equation 2.22.

Figure 5.4 shows the associated phase contrast image acquired with the same specimen. Phase contrast imaging is a dark-field modality that benefits from the retardation of light due to the spatial variations of the refractive index in the sample and is used to enhance the contrast of transparent specimens [174]. The image was acquired in a single frame using the Pulnix CCD camera mounted on a side port of the inverted Olympus microscope, which was set in the standard phase contrast mode.

The Brillouin image showed great contrast between the cell and the surrounding PBS buffer solution. This contrast was lost in the associated phase contrast image due to a uniform spatial distribution of the refractive index. The elliptical shape of the cell nucleus could be clearly identified suggesting a higher stiffness for the nucleus membrane. Interestingly, the four nucleoli inside the cell nucleus appear

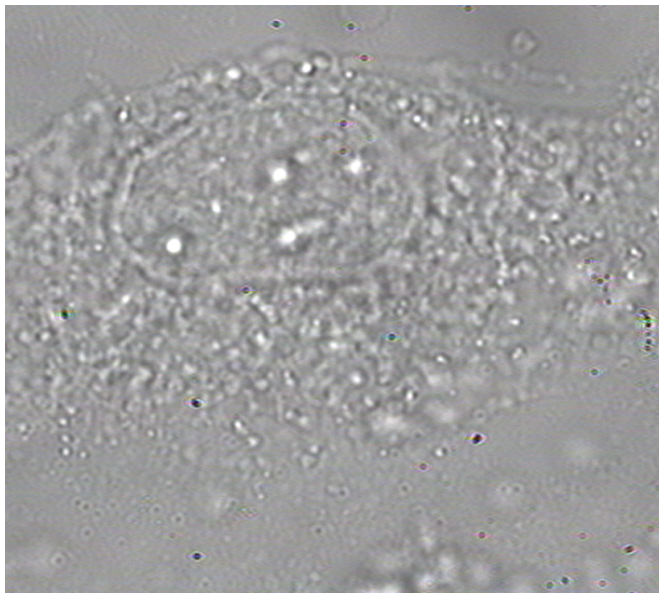


**Figure 5.4:** Phase contrast image of the HUVEC cell. The sample was entirely illuminated by the microscope phase contrast mode and acquired by a Pulnix CCD camera.

to be significantly stiffer compared to the surrounding cytoplasm, which might be due to their high RNA content [175]. The Brillouin modulus was measured to be $M' = 3.03 \pm 0.12$ GPa for the nucleoli and $M' = 2.73 \pm 0.24$ GPa for the cytoplasm. Values of the Brillouin modulus were estimated by averaging over several regions of interest across the image.

### 5.2.3 *Latrunculin-A* for Stiffness Assessment

A set of measurements was taken to investigate the effect of the *Latrunculin-A* drug on the cell stiffness. Previous AFM measurements have reported a decrease in the Young's modulus in both HUVEC and SC cells when the drug was applied [166]. Specifically, the analyses showed that Latrunculin-A led to a decrease in the Young's modulus from $E = 1.40 \pm 0.33$ kPa to $E = 0.78 \pm 0.26$ kPa. The measurement was repeated using Brillouin microscopy.

Figure 5.5 shows Brillouin images of the same HUVEC cell before and after the application of the drug. Cells were cultured in an equal process to that described in Section 5.2.1. The sample dishes were filled with a diluted PBS solution, which was sealed by a thin oil film so as to ensure thermal isolation. In order to decrease the

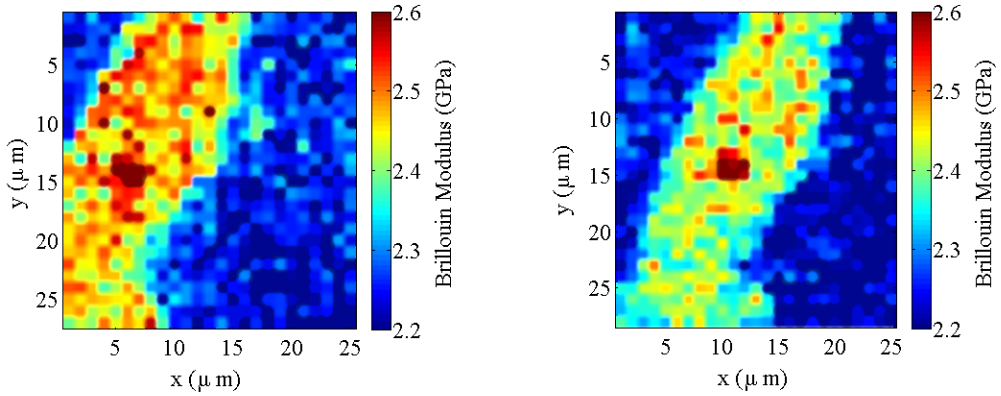



**Figure 5.5:** Brillouin images of a HUVEC cell before (left) and after (right) the addition of Latrunculin-A. The stiffness images were normalised to the modulus of PBS solution. A 4% decrease in stiffness was found after the drug addition.

data acquisition times to avoid dramatic changes in the thermodynamical properties of the cells during acquisition, samples were scanned with 1 $\mu$m step size across the $xy$ plane. The exposure time was set to 0.5 sec/frame yielding a total acquisition period of 10 minutes for a single Brillouin image. In order to test whether temperature fluctuations or other environmental factors were affecting the mechanical properties of the cells, two sets of measurements were taken with a time interval of approximately 30 minutes between each other. The acquisitions confirmed a constant level of stiffness over time with an average Brillouin modulus across the cytoplasm of $M' = 2.57 \pm 0.54$ GPa. Subsequently, the Latrunculin-A at 1 $\mu$M was applied to the HUVEC cells and a third acquisition was taken with equal exposure time and step size. The two images shown in Figure 5.5 were normalised to the Brillouin modulus of the diluted PBS solution, which was measured to be $M' = 2.226 \pm 0.034$ GPa. The average over the cytoplasmic region of the cell gave a Brillouin modulus of $M' = 2.36 \pm 0.51$ GPa, which represents approximately an 8% decrease in stiffness with respect to the original state. This result confirmed the outcome reported by the AFM measurements. As previously described, the Brillouin modulus was found to have a linear relationship with the Young's modulus and small changes in the Brillouin modulus reflect variations in the Young's modulus on a larger scale, which may justify the greater variation in stiffness reported in the previous AFM analysis.

Overall, the investigation provided another important proof of the Brillouin microscope's ability to measure stiffness in biological systems. Future analyses will focus on the investigation of the mechanical properties of both normal and glaucomatous SC cells as a fundamental step in the understanding of the origin of glaucoma.

## 5.3 Arteries Mechanics in Atherosclerosis

Atherosclerosis is a form of arteriosclerosis, which is a cardiovascular disease caused by hardening of the arteries associated with the accumulation of degenerative material such as lipids (cholesterol and fatty acids), proteins and fibrous tissues along the inner layer. Figure 5.6 shows diagrams which compare the case of a healthy and a diseased artery. Atherosclerosis occurs due to the formation of *atheromatous plaques*, which lead to irreversible damages of the endothelial layers [177]. The presence of plaques in arteries is often clinically silent until the sudden rupture of the membrane due to muscular stiffening. When atherosclerosis affects functional arteries of the heart muscle, the disease is known as coronary artery disease (CAD). Recent studies have revealed that CAD is the major cause of death in the US, affecting more than 16 million people yearly, half of which had a myocardial infarction (MI). Moreover, statistics showed that about 30% of all deaths in the UK are due to

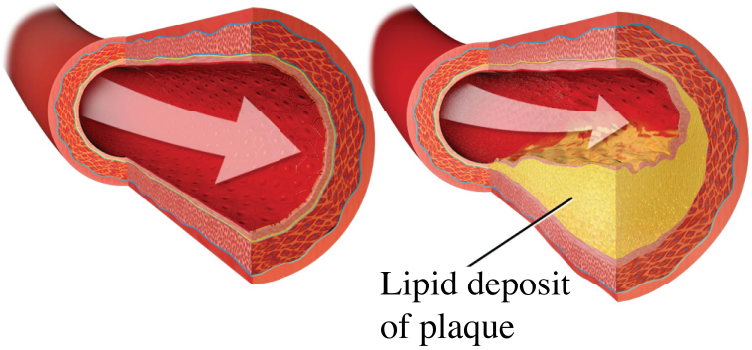



**Figure 5.6:** Diagram of a normal (left) and a diseased (right) coronary artery. The artery becomes narrower and stiffer due to the formation of atherosclerotic plaques. From [176].

cardiovascular diseases. MI stems from disruption in blood flow to the heart muscle caused by plaque ruptures. In fact, expulsion of plaque content activates a cascade of events that eventually lead to thrombosis and death.

Currently the only available strategy to reduce mortality in CAD is prevention, which is accomplished by monitoring the grade of stiffness of the artery walls. Clinical practices for diagnosis of atherosclerosis are primarily based on radio frequency screenings and ultrasound echocardiograms [178, 179, 180], which are intrinsically limited by a poor spatial resolution. Pulse wave velocity (PWV) is another common method that measures arterial pulse wave velocity to investigate elasticity *in vivo* [181, 182]. PWV increases with stiffness and is governed by the Moens-Korteweg equation, which is expressed as [182]

$$\mathrm{PWV} = \sqrt{\frac{Eh}{2\rho R}}, \tag{5.1}$$

where $E$ is the Young's modulus of the arterial wall, $h$ is the wall thickness, $R$ is the artery diameter at the end of the diastole, which is the blood refilling process of the heart, and $\rho$ is the blood density. The distance and the time travelled by the pulse is estimated along the aorta and PWV is measured by means of either a pressure-sensitive transducer or Doppler ultrasound. PMW can also be measured in a non-invasive manner by means of MRI [183]. Besides the high costs, non-invasive PWV requires strong magnetic fields, which makes this technique difficult to apply in clinical studies.

Other methods, such as blood tests, chest X rays and tomographic scans, can only help pathologists to estimate the extent of the disease. For instance, OCT is an established imaging technique which provides structural information of biological systems. OCT relies on the low-coherence interference between the scattered light and a broadband illumination source [184]. OCT has seen extensive use in imaging of coronary arteries and, over the last few years, has achieved a spatial resolution of a few microns [185]. Despite structural information of biological systems, this technique cannot retrieve their stiffness properties.

We have established that confocal Brillouin microscopy can be used to successfully image the stiffness variations in the walls of blood vessels to sub-cellular reso-

lution, hence is a potential candidate as the tool of choice for earlier stage diagnoses. In the following sections, we review the use of confocal Brillouin microscopy in artery wall stiffness measurement and present examples of Brillouin microscope images.

### 5.3.1 Sample Preparation

Optical clearing refers to a range of chemical protocols that provide a significant enhancement of the transparency of biological tissues [186]. The high scattering of turbid biological tissues limits the penetration depth of the probe beam, therefore affecting the reconstruction of three dimensional images from different focal depths. Optical transparency can be achieved by embedding the tissue with an appropriate buffer solution in the attempt to match the refractive index of the specimen. Over the last decade, several protocols have been developed to reduce scattering from biological samples [187, 188]. These enabled a deeper penetration and an improved imaging contrast of the inner structures of the tissues.

Besides an increase in the beam penetration depth, optical clearing can be of great advantage in confocal Brillouin microscopy where a high amount of elastic scattered light arising at the sample surface may impede the detection of the Brillouin spectra. Particular attention was paid in selecting a suitable buffer solution that did not affect the mechanical properties of the tissues. For instance, *VECTASHIELD Hard Set* mounting medium was first tested as a standard clearing agent. However, its use led to a gradual stiffening of the tissue over a period of time of about 24 hours, hence it was discarded for our purposes. The final solution employed consisted of pure glycerol of refractive index $n = 1.47$ close to that of biological tissues, which has been estimated to be approximately $n = 1.46$ in the visible [189]. The Brillouin frequency shift of glycerol in the backscattering geometry was measured $\nu_b = 15.51 \pm 0.12$ GHz, and assuming a density of 1.26 g/cm$^3$ [190] the Brillouin modulus was estimated to be $M' = 11.03 \pm 0.21$ GPa.

Cross sections of mice arteries were cut with a thickness of approximately 10 $\mu$m. Frozen sections were embedded in glycerol solution and sandwiched between a microscope slide and a standard glass coverslip of thickness 170 $\mu$m. It must be noted that the glycerol solution did not penetrate the tissues but it was used as an immersion buffer to reduce the elastic scattering at the sample surface. Nail polish

was used to seal the glass coverslip to avoid sample displacement and dehydration during acquisitions.

### 5.3.2 Artery Mechanical Imaging

Before investigating the mechanical properties of the atherosclerotic plaques, several acquisitions were performed with normal mouse blood vessels. Figures 5.7 and 5.8 show the Brillouin image and the associated phase contrast image of an entire mouse artery cross section. The Brillouin image was taken with an exposure time of 0.35

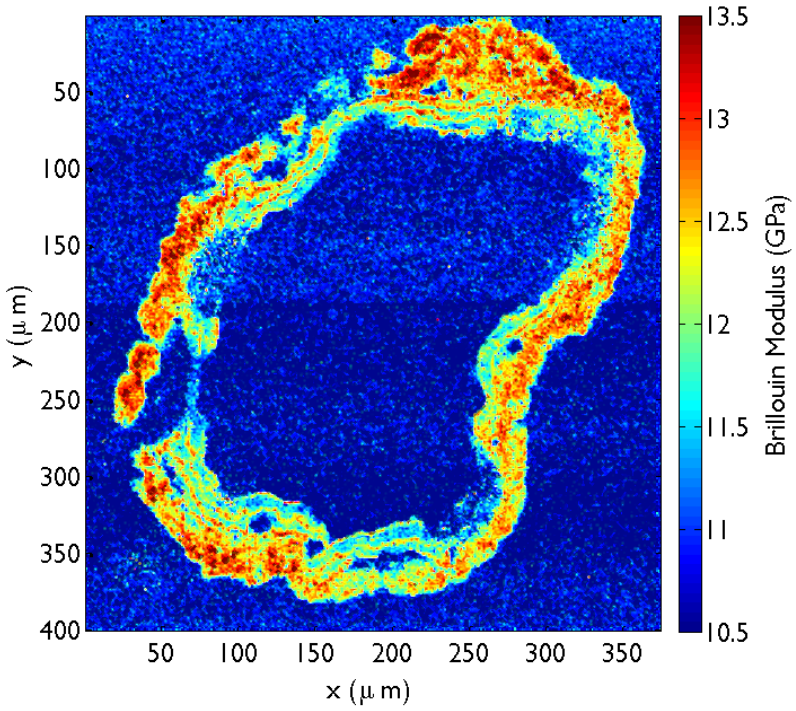



**Figure 5.7:** Brillouin image of a cross section of a normal mouse blood vessel. The adventia appears to be stiffer compared to the inner substrate, as suggested by morphological studies.

sec/frame and a scan step of 1.2 $\mu$m. Data acquisition started approximately 30 minutes after sample preparation in order to allow the frozen tissue to stabilise at the room temperature ($\sim$ 24°C). Total acquisition time required approximately 14 hours. As previously discussed, the reason why the scanning step size was greater than the optical resolution was purely due to time restrictions. The longer the data

acquisition time, the higher the risk of mechanical changes in the embedded tissue.

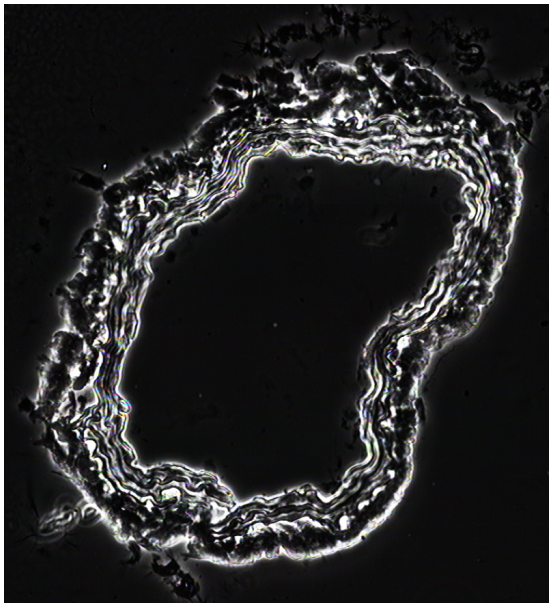


**Figure 5.8:** Associated phase contrast image of the artery cross section.

The blood vessel walls exhibited a significant spatial variation in stiffness, which could be directly observed in the Brillouin image. A significant difference in the elastic modulus was found between the outer wall of the artery and the inner layers close to the *lumen*, which is the inside space of the tubular structure. The outer layer known as the *adventia* appears to be stiffer than the inner structure. The Brillouin modulus was estimated by averaging over different regions of interest across the image, yielding $M' = 13.24 \pm 0.27$ GPa for the outside tissue and $M' = 11.72 \pm 0.31$ GPa for the inside layer. These results confirm the current understanding of a higher stiffness corresponding to the outside of blood vessels than that of the inside. In fact, morphological studies have assessed the adventia formed by a strong fibrous tissue which maintains the vessel shape in a robust shell [191, 192]. On the other hand, the inner structure is divided by the *tunica media* and the *tunica intima*. These are composed of smooth muscles, elastic lamina and connective tissues containing high amounts of lipids. The assumption of a softer arterial inner substrate stems from the high concentration of lips, which are mostly composed of fat molecules [193]. Nevertheless, no direct evidence of this property has been found in arteries. To the best of our knowledge, the results obtained with the confocal Brillouin microscope

represent the first quantitative proof of this hypothesis. As previously discussed, other conventional elastography techniques are limited by a lower spatial resolution, which impedes distinguishing the outer from the inner regions.

Figure 5.9 shows the stiffness image corresponding to a small region of a mouse artery cross section. In order to obtain a more detailed structure of the wall stiffness,

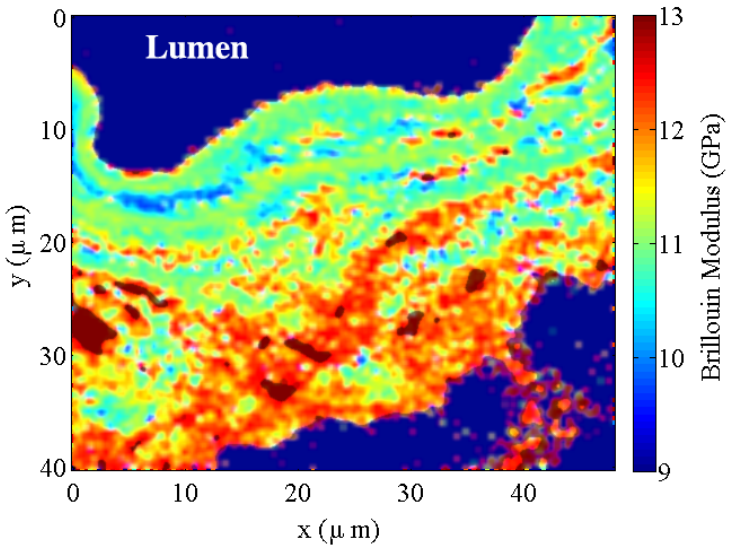



**Figure 5.9:** High resolution Brillouin image of a small region of a normal artery cross section. The image confirms a higher stiffness for the adventia. Interestingly, layers of different elasticities can be identified within the tunica wall.

the scan step was decreased to 0.4 $\mu$m, which was close to the full transverse resolution of the microscope ($r = 0.26\,\mu$m). Integration time was set to 0.3 sec/frame for a total acquisition period of approximately 1 hour.

The image confirmed a higher Brillouin modulus for the adventia. Interestingly, thin layers of different stiffnesses can be identified along both the tunica media and the tunica intima of the artery. This suggests that normal arteries might be formed by more complex structures than that evinced from morphological studies. The endothelium substrate next to the lumen appears to be stiffer than the tunica intima. Overall, the Brillouin modulus of the artery can be observed to lie within the range $M' = 10 - 14$ GPa, which is significantly higher with respect to that of the HUVEC cells previously investigated ($M' = 2.5 - 3.5$ GPa).

### 5.3.3 Mechanical Imaging of Atherosclerotic Plaques

The results obtained with normal blood vessels encouraged the application of the Brillouin microscope to the investigation of the mechanical properties of atherosclerotic plaques.

Measurements were taken for both healthy and diseased mouse blood vessels. Female ApoE-/- mice (20-23 grams in weight) were used for all biological experiments, which were conducted by Dr Ryan Pedrigi. The artificial growth of atherosclerotic plaques in the animals was driven using a similar procedure to that applied by Cheng *et al.* [194, 195]. In particular, the mice were placed on a high-fat Western-type diet (*Lillico Biotech*, UK) at the age of 11 weeks. Two weeks later, the mice went through the surgical procedure of placing a flow-modifying cuff on the left carotid arteries. The cuff was composed of two thermoplastic polyetherketone cylindrical halves with a conical lumen that tapers from 500 $\mu$m at the base to 250 $\mu$m at the throat of the cuff. The placement of the cuff creates a gradual stenosis in the artery, leading to shear stress-related plaque initiation. Atherosclerotic lesions developed in the vicinity of the chuff base where shear stress was lower. Successively, 30 cross sections were exported from both a diseased and a healthy (test) artery of the same mouse. Each section addressed to Brillouin imaging was accompanied by an adjacent slice, which underwent to an *Oil-red-O staining* process [196] to highlight the region of the artery with high lipid concentration.

Brillouin images of 15 cross sections of both healthy and diseased arteries were acquired for stiffness measurement. Figure 5.10 shows the stiffness image of one cross section of the diseased artery. The image was taken with an exposure time of 0.3 sec/frame and a scan step of 1.8 $\mu$m for a total acquisition period of approximately 14 hours. The associated phase contrast and stained images are shown in Figure 5.11. The region of high lipid content of the tissue was marked in red colour following the Oil-red-O staining (0.5% Oil-red-O solution in Propylene glycol) with Mayers Hemotoxylin counterstain. Since the atherosclerotic lesion is associated with a high lipid accumulation, this plaque region could be identified in the stained image.

The outer annular wall of the artery was found to be stiffer than the atheromatous plaque, as shown in Figure 5.10. In this case, however, the adventia and the inner

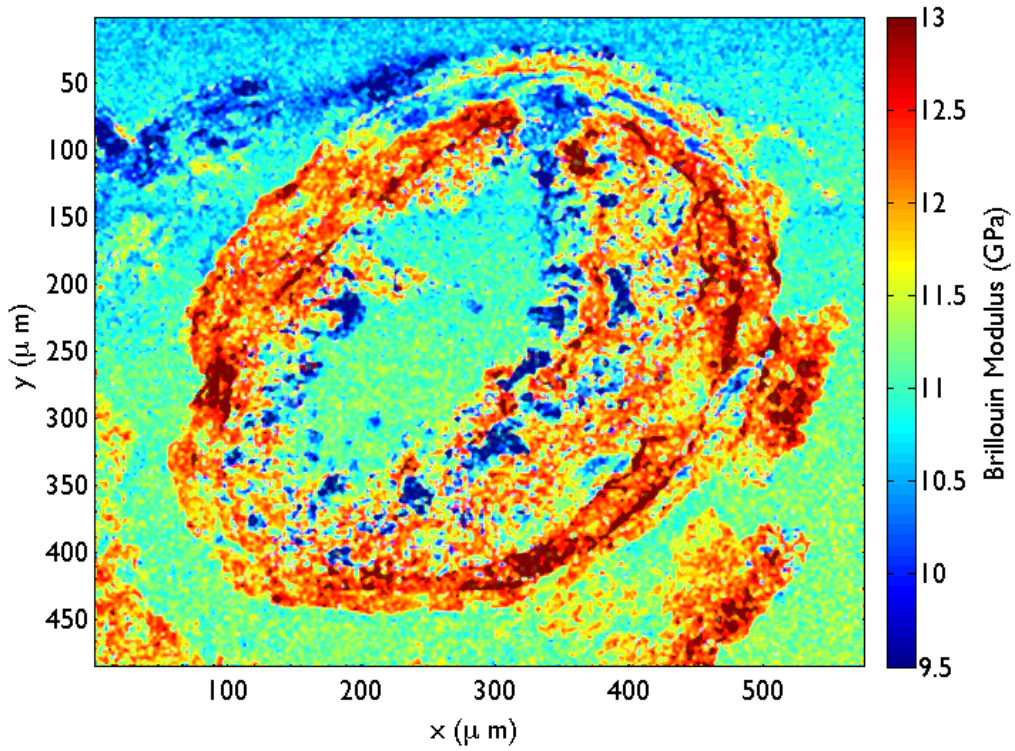



**Figure 5.10:** Cross sectional Brillouin image of a mouse blood vessel affected by atherosclerosis. The outer tissue appear to be stiffer with respect to the plaque. The image suggests that the plaque is formed of a variety of organic materials of different stiffnesses.

tunica of the artery wall appeared more uniform in stiffness with respect to the healthy vessels shown in Figure 5.7 and 5.9. The Brillouin modulus in the diseased wall region was estimated to be $M' = 12.64 \pm 0.33$ GPa. On the other hand, it was observed that the atherosclerotic plaque was composed of a complex mixture of organic compounds with different elasticity. Unlike the stained sections, Brillouin images suggest an accumulation of softer materials in the narrow region surrounding the lumen. The Brillouin modulus of the atheromatous plaque was found to be $M' = 9.72 \pm 0.36$ GPa in the vicinity of the lumen and $M' = 11.36 \pm 0.45$ GPa in the central region of the plaque.

In order to obtain a more quantitative figure, Brillouin images of diseased and

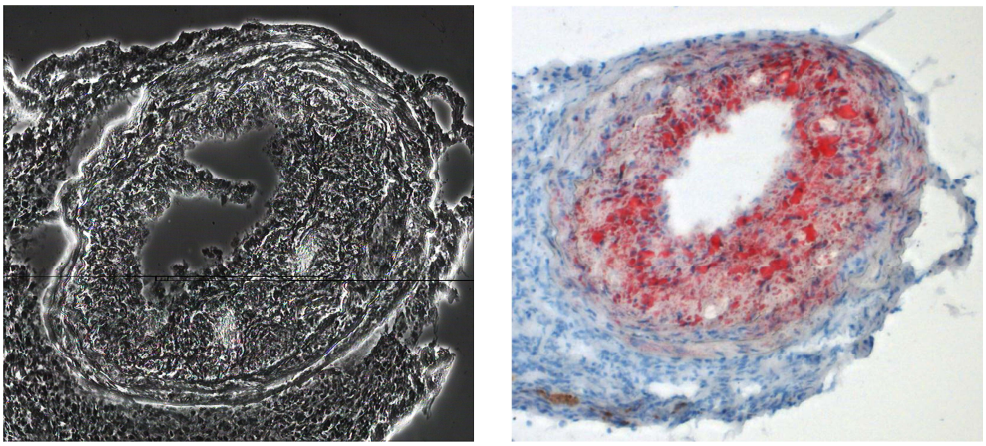


**Figure 5.11:** Associated phase contrast (left) and stained (right) images of the same diseased artery cross section. The red colour outlines the plaque region due to the high lipid concentration.

control mouse carotid artery sections were further analysed by Dr Ryan Pedrigi by averaging the stiffness of the diseased vessel intima (i.e. the plaque area), diseased

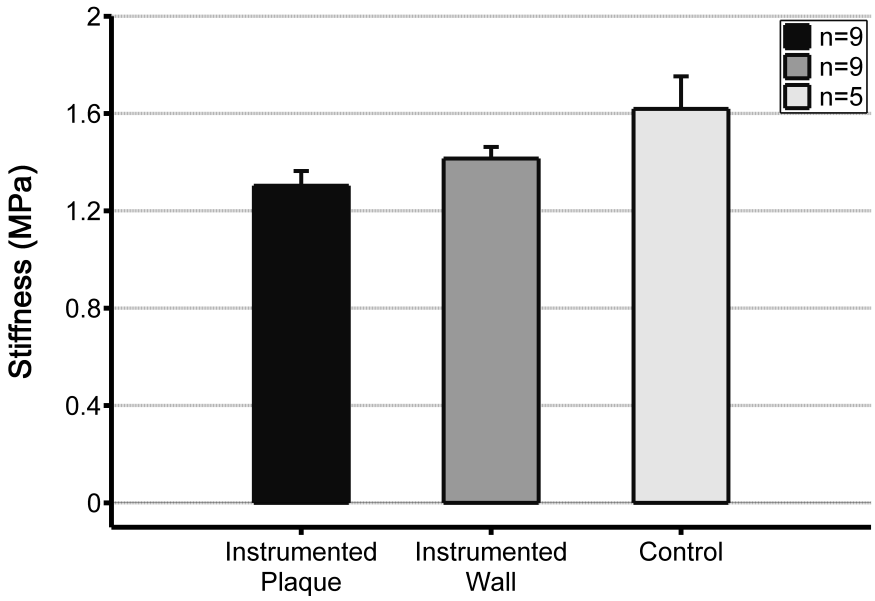



**Figure 5.12:** Average stiffness of the diseased vessel intima and both diseased and control walls. $n$ is the number of sections analysed. The data shows that the atherosclerotic plaque has a lower stiffness than the diseased and normal wall.

vessel wall, and control wall after segmenting them from each image. The PDMS correlation plot illustrated in Figure 5.1 was used to convert the Brillouin modulus into the standard Young's modulus metric. Results are illustrated in Figure 5.12 and show that the intima of the diseased vessel had a lower stiffness than the diseased wall or control, which was statistically significant ($p < 0.01$). In particular, the data shows that the Young's modulus of the plaque was lower than that of both the diseased and control artery walls by approximately 8% and 19% respectively. Furthermore, the control was stiffer than the diseased wall by $\sim 12\%$, which suggests that the vessel wall was directly affected by the formation of the atherosclerothic plaques.

Despite the requirement of further validations, these results encourage the application of confocal Brillouin microscopy as the tool of choice for artery wall measurements, in particular when atherosclerotic plaques are formed.

# Chapter 6

# Conclusions

The main focus of this research was to develop a Brillouin light scattering microscope with high spatial resolution. Brillouin scattering is a weak inelastic scattering process arising from the interaction of light with thermal acoustic waves of materials. The frequency shift of the scattered photons due to the energy transfer results in a spectrum which provides fundamental information about the material mechanical properties. The study of the Brillouin scattered light has progressed in 2005 from single point spectroscopy to a new imaging modality with a transverse resolution of $\sim 20\,\mu$m [47]. During the last decade, important steps forward have been achieved in this field. An important contribution was achieved by Scarcelli and Yun who first applied the novel imaging technique to the study of the elasticity properties of the eye lens and cornea [52]. A significant enhancement of the integration times of the Brillouin spectrum was obtained by the application of the VIPA etalon and the technological advances in high sensitivity CCD cameras.

This research began with the characterisation of a VIPA spectrometer. This is a customised Fabry-Pérot etalon that incorporates an AR coated entrance window used to minimise optical losses. The longitudinal modes of a He-Ne laser were observed and a VIPA of spectral resolution $\delta\nu = (438 \pm 5)$ MHz, free spectral range of $\Delta\nu = (39.5 \pm 0.5)$ GHz and finesse of $\mathcal{F} = 90.2 \pm 0.5$ was employed to disperse the weak Brillouin signal. Since biological systems are highly scattering, a high spectral contrast was required to avoid formation of the elastic crosstalk. A two-

stage VIPA spectrometer was built to rotate the dispersion axis from the elastic spectral lines. Consequently, the inelastic peaks were displaced from the crosstalk and a greater spectral contrast was obtained. The addition of two spatial masks at the intermediate Fourier planes of the spectrometer enabled a significant suppression of the elastic contribution. A lower amount of light entering the VIPA led to a higher extinction ratio. Furthermore, a continuous varying neutral density filter was aligned next to the first VIPA so as to obtain a more Gaussian-shaped beam profile at the output. The introduction of the apodization filter gave an additional 10 dB improvement. The total extinction of the spectrometer was measured to be $\sim 60$ dB, which was sufficient to enable Brillouin imaging of biological systems. A two-stage VIPA spectrometer with etalons of different dispersion powers was also investigated in an attempt to separate the Stokes from the Anti-Stokes dispersion lines, therefore paving the way to combine Brillouin microscopy with alternative spectroscopic techniques, such as fluorescence imaging.

Investigations into Brillouin scattering were made before any imaging was attempted. A 90° scattering geometry system was built and the Brillouin spectrum of several liquids was acquired as a first calibration.

The spectral broadening of the Brillouin spectrum due to finite instrumental apertures was the main reason for the poor spatial resolution in Brillouin imaging and was therefore a fundamental aspect to analyse. In fact, collection of photons at different scattering angles leads to broadening and distortion of the Brillouin spectrum, therefore affecting the localisation accuracy of the inelastic peaks. Computational and experimental results confirmed that this effect is minimised in a backscattering geometry, hence paving the way to high spatial resolution Brillouin microscopy.

A dark-field Brillouin microscope was built in an attempt to reduce the amount of specular reflections collected by the system. This involved the employment of an annular illumination generated by a customised prism. The optimal aspect ratio of the annular beam was derived in order to optimise the system efficiency. Preliminary Brillouin images were taken with liquid interfaces, showing great contrast with respect to the associated dark-field images.

Despite suppression of specular reflections, the dark-field arrangement was lim-

ited by a long data acquisition time and a poor axial resolution. These limitations led to the design of a confocal Brillouin microscope. An oil-immersion microscope objective (NA = 1.3, 100x) was employed and its aperture was uniformly illuminated by an expanded single longitudinal mode laser beam to obtain sub-wavelength spatial resolution. The spectrum of the scattered light was resolved by the two-stage VIPA spectrometer and collected by an sCMOS camera with an integration period of approximately 0.2 seconds. Data processing was performed by bespoke codes. A reference of water was taken before data acquisition to measure the Brillouin frequency shift across the sample. Both spatial resolution and data acquisition time were improved by two orders of magnitude with respect to the first Brillouin imaging system prototype proposed by Koski and Yarger in 2005.

Several measurements with samples of known elasticity were performed in an attempt to find a correlation between the Brillouin modulus and the standard Young's modulus. The calibration curves suggested the existence of a linear relationship between the two elasticity moduli, validating Brillouin spectroscopy as a reliable method to measure stiffness. Nevertheless, the results showed that the linear relationship varies depending on the material properties, and ultimately represents a fundamental aspect that needs further investigation.

The confocal Brillouin microscope addressed the investigation of both the mechanical properties of cells responsible for glaucoma and the stiffness variation in atherosclerotic plaques. To the best of our knowledge this thesis presented, for the first time, *in vitro* Brillouin images of single cells. In particular, Brillouin images of HUVEC cells were acquired. Cell nucleoli were spatially resolved and appeared to have a higher stiffness than the surrounding cytoplasm, which might be due to their high RNA content. Furthermore, we proved that when Latrunculin-A is applied directly to endothelial cells, the cell stiffness decreases as suggested by previous AFM indentation measurements.

Both healthy and diseased mouse blood vessel walls were analysed. Cross sections of arteries were embedded in glycerol in an attempt to decrease elastic scattering at the sample surfaces. Brillouin images of healthy arteries confirmed the morphological hypothesis of a stiffer adventia wall with respect to the inner layers. High resolution stiffness images of small regions of the cross sections suggested the exis-

tence of a more complex structure forming the inside tunica of the blood vessels. In order to compare these results with the case of diseased vessels, mice went through the surgical procedure of placing a flow-modifying cuff on the left carotid arteries. Placement of the cuff created a gradual stenosis in the artery, leading to the formation of plaques. Several Brillouin images of both diseased and normal vessels were acquired and analysed by averaging the stiffness after segmentation. Atherosclerotic plaques had a lower stiffness than the diseased wall or control wall, in agreement with predictions based on the high concentration of lipids. Nevertheless, results suggested that the plaques might be formed by the accumulation of organic materials of different stiffness rather then being uniform as shown in the associated Oil-red-O stained images.

The results presented in this thesis might encourage the application of confocal Brillouin microscopy as the tool of choice for the understanding and the early diagnosis of critical asymptomatic diseases, such as glaucoma and atherosclerosis. Even though the spatial resolution was increased to the natural optical diffraction limit, the acquisition time of the Brillouin spectrum still represents the main limitation of the microscope designed. Future progress in the field might see the employment of faster detectors and the enhancement of the Brillouin signal through resonant mechanisms. A faster data acquisition time may allow in vivo three dimensional mechanical imaging, therefore paving the way to new fundamental biological applications.

# Appendix A

# Beam Convergence

A condition for the angle of convergence of the beam focused to the VIPA is obtained to maximise the intensity of the spectral pattern along two consecutive fringes, i.e. over a single FSR. Figure A.1 shows a diagram of the angular separation between two consecutive interference orders at the output of a FP. The angle $\theta$

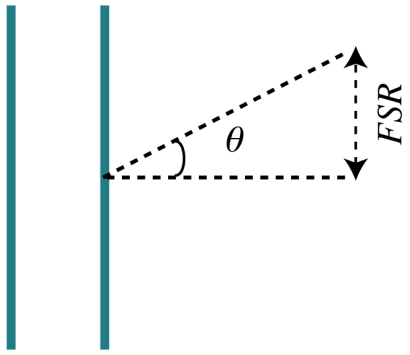



**Figure A.1:** Angular separation between two interference orders at the FP output.

is associated with the angle of convergence of the beam focused to the FP. The expression defining the order of interference $m$ of the FP as a function of the angle $\theta$ is given by

$$m = \frac{2nd\cos\theta}{\lambda}, \tag{A.1}$$

where the cosine function can be expressed as a first order of its Taylor's expansion

so that

$$\cos\theta \approx 1 - \frac{\theta^2}{2}. \tag{A.2}$$

By subtracting two consecutive interference orders

$$\frac{2nd}{\lambda} - \frac{2nd(1-\theta^2/2)}{\lambda} = 1, \tag{A.3}$$

where the first term represents the highest order ($\theta = 0$), we obtain

$$\theta = \sqrt{\frac{\lambda}{nd}}. \tag{A.4}$$

Equation A.4 gives the angular separation for two subsequent interference orders of a FP, as illustrated in Figure A.1. Consequently, in order to maximises the intensity of two Brillouin peaks contained in a single FSR, the beam convergence $\alpha$ of the Gaussian beam focused to the VIPA has to satisfy the condition

$$\alpha \geq \frac{1}{2}\sqrt{\frac{\lambda}{nd}}. \tag{A.5}$$

# Appendix B

# Brillouin Spectra of Liquids

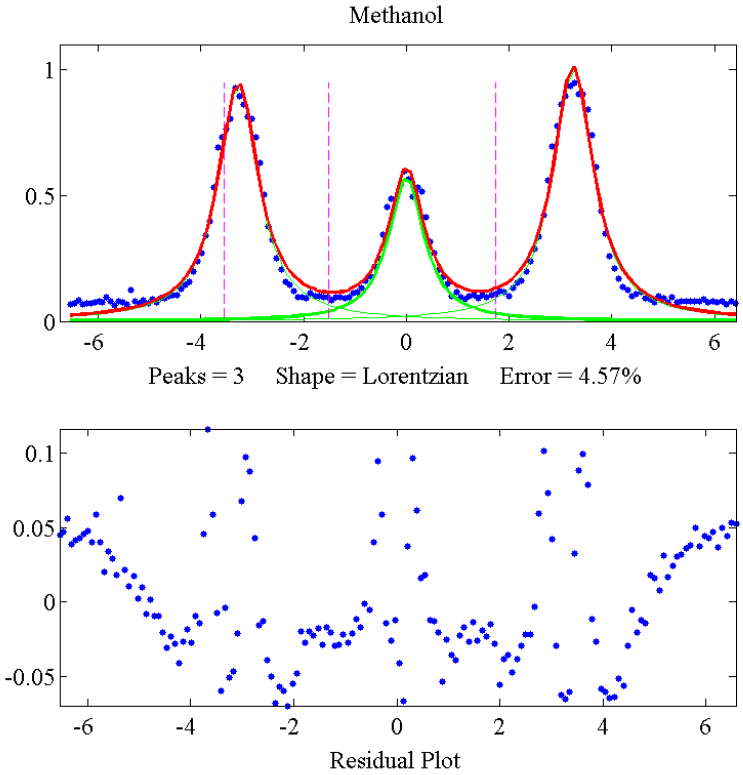



**Figure B.1:** Experimental data and least-squares fitting (top) with residual data points (bottom) for methanol.

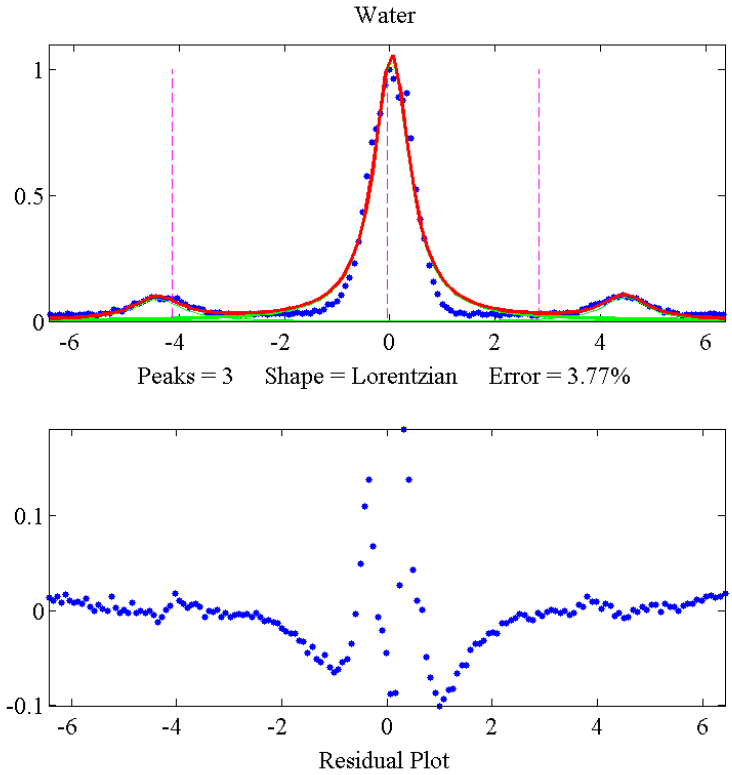



**Figure B.2:** Experimental data and least-squares fitting (top) with residual data points (bottom) for water.

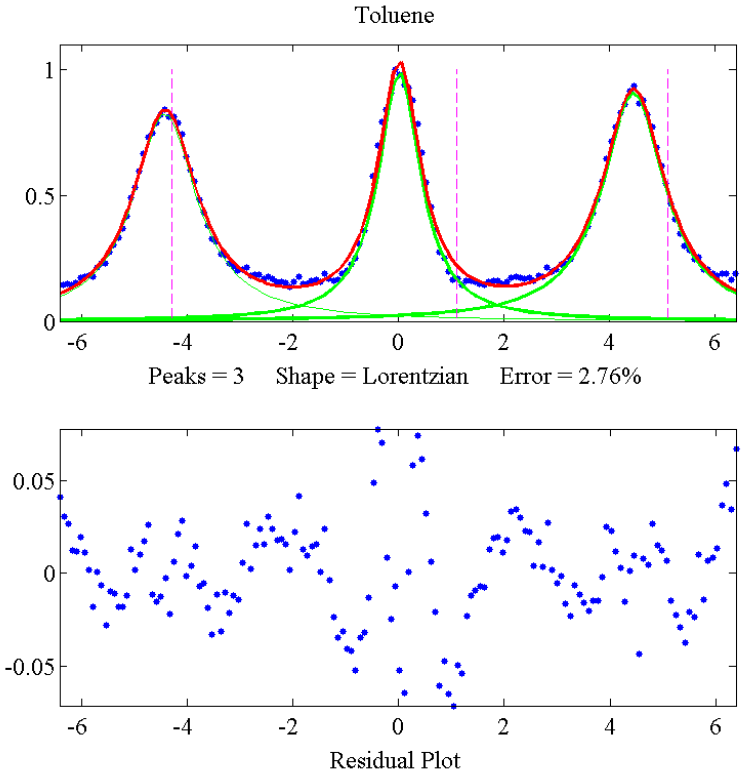



**Figure B.3:** Experimental data and least-squares fitting (top) with residual data points (bottom) for toluene.

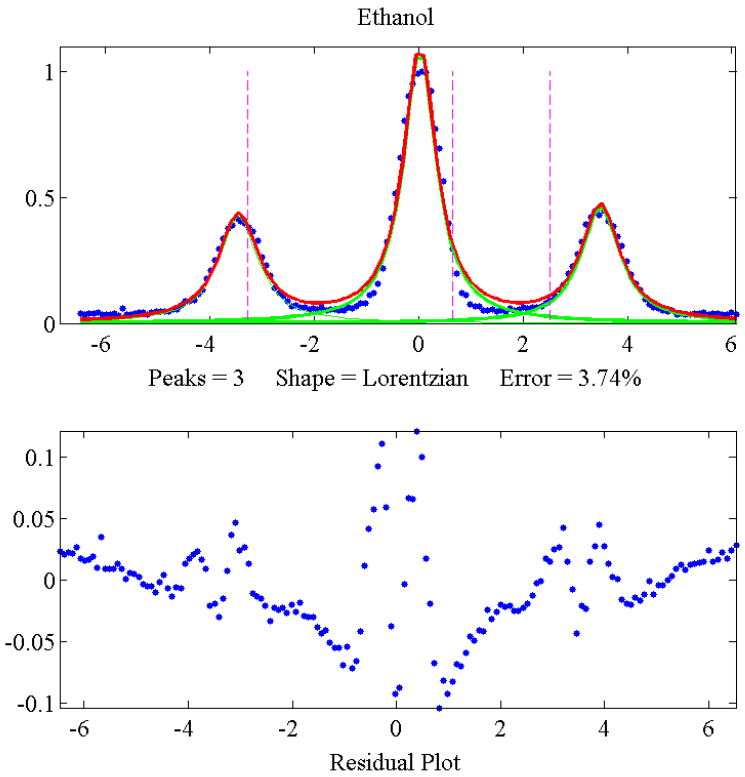



**Figure B.4:** Experimental data and least-squares fitting (top) with residual data points (bottom) for ethanol.

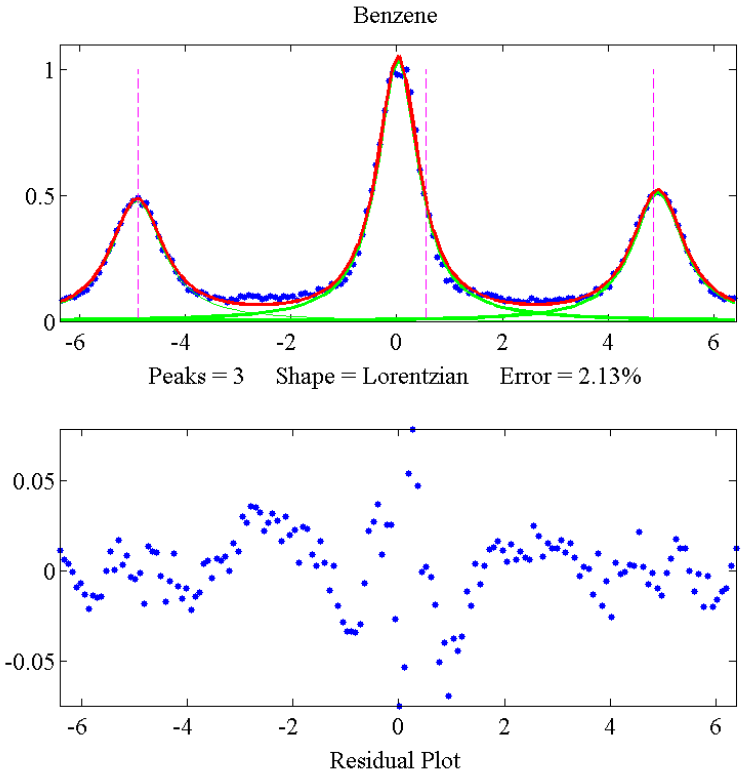



**Figure B.5:** Experimental data and least-squares fitting (top) with residual data points (bottom) for benzene.

# Bibliography

[1] J. Ophir, I. Cespedes, B. Garra, H. Ponnekanti, Y. Huang, and N. Maklad, "Elastography: Ultrasonic imaging of tissue strain and elastic modulus in vivo," *European Journal of Ultrasound*, vol. 3, no. 1, pp. 49 – 70, 1996.

[2] S. H. Cho, J. Y. Lee, J. K. Han, and B. I. Choi, "Acoustic radiation force impulse elastography for the evaluation of focal solid hepatic lesions: Preliminary findings," *Ultrasound in Medicine and Biology*, vol. 36, no. 2, pp. 202 – 208, 2010.

[3] R. Sinkus, M. Tanter, S. Catheline, J. Lorenzen, C. Kuhl, E. Sondermann, and M. Fink, "Imaging anisotropic and viscous properties of breast tissue by magnetic resonance-elastography," *Magnetic Resonance in Medicine*, vol. 53, no. 2, pp. 372–387, 2005.

[4] A. Di Ieva, F. Grizzi, E. Rognone, Z. Tse, T. Parittotokkaporn, F. Rodriguez y Baena, M. Tschabitscher, C. Matula, S. Trattnig, and R. Rodriguez y Baena, "Magnetic resonance elastography: a general overview of its current and future applications in brain imaging," *Neurosurgical Review*, vol. 33, no. 2, pp. 137–145, 2010.

[5] C. Sun, B. Standish, and V. X. D. Yang, "Optical coherence elastography: current status and future applications," *Journal of Biomedical Optics*, vol. 16, no. 4, pp. 043001–12, 2011.

[6] A. Khalil, R. Chan, A. Chau, B. Bouma, and M. Mofrad, "Tissue elasticity estimation with optical coherence elastography: Toward mechanical characterization of in vivo soft tissue," *Annals of Biomedical Engineering*, vol. 33, no. 11, pp. 1631–1639, 2005.

[7] R. K. Wang, Z. Ma, and S. J. Kirkpatrick, "Tissue Doppler optical coherence elastography for real time strain rate and strain mapping of soft tissue," *Applied Physics Letters*, vol. 89, no. 14, 2006.

[8] B. F. Kennedy, T. R. Hillman, R. A. McLaughlin, B. C. Quirk, and D. D. Sampson, "In vivo dynamic optical coherence elastography using a ring actuator," *Opt. Express*, vol. 17, pp. 21762–21772, Nov 2009.

[9] B. Poon, D. Rittel, and G. Ravichandran, "An analysis of nanoindentation in linearly elastic solids," *International Journal of Solids and Structures*, vol. 45, no. 24, pp. 6018 – 6033, 2008.

[10] Q. Li, G. Lee, C. Ong, and C. Lim, "AFM indentation study of breast cancer cells," *Biochemical and Biophysical Research Communications*, vol. 374, no. 4, pp. 609 – 613, 2008.

[11] R. M. Pedrigi, D. Simon, A. Reed, W. D. Stamer, and D. R. Overby, "A model of giant vacuole dynamics in human Schlemm's canal endothelial cells," *Experimental Eye Research*, vol. 92, no. 1, pp. 57 – 66, 2011.

[12] K. D. Costa, "Single-cell elastography: Probing for disease with the atomic force microscope," *Disease markers*, vol. 19, no. 2, pp. 139–154.

[13] B. Bhushan and V. N. Koinkar, "Nanoindentation hardness measurements using atomic force microscopy," *Applied Physics Letters*, vol. 64, no. 1653, 1994.

[14] G. Antonacci, M. R. Foreman, C. Paterson, and P. Török, "Spectral broadening in Brillouin imaging," *Applied Physics Letters*, vol. 103, no. 22, p. 221105, 2013.

[15] J. Strutt, "On the transmission of light through an atmosphere containing small particles in suspension, and on the origin of the blue of the sky," *Philosophical Magazine*, vol. 47, no. 5, pp. 375–394, 1899.

[16] I. L. Fabelinki, *Molecular scattering of light*. Plenum Press, 1968.

[17] K. Maslov, G. Stoica, and L. V. Wang, "In vivo dark-field reflection-mode photoacoustic microscopy," *Opt. Lett.*, vol. 30, pp. 625–627, Mar 2005.

[18] C. V. Raman and K. S. Krishnan, "A new type of secondary radiation," *Nature*, vol. 121, no. 3048, pp. 501–502, 1928.

[19] R. G. A. Zumbusch and S. Xie, "Three-Dimensional Vibrational Imaging by Coherent Anti-Stokes Raman Scattering," *Phys. Rev. Lett.*, vol. 82, no. 20, pp. 4142–4145, 1999.

[20] L. E. Kamemoto, "Near-infrared micro-Raman spectroscopy for in vitro detection of cervical cancer," *Applied Spectroscopy*, vol. 64, no. 3, pp. 225–261, 2010.

[21] L. Brillouin, "Diffusion de la lumiere et des rayonnes x par un corps transparent homogene: influence del'agitation thermique," *Ann. Phys.*, vol. 17, pp. 88–122, 1922.

[22] R. Y. Chiao and B. P. Stoicheff, "Brillouin scattering in liquids excited by the He-Ne maser," *J. Opt. Soc. Am.*, vol. 54, pp. 1286–1287, Oct 1964.

[23] R. Vacher and L. Boyer, "Brillouin scattering: A tool for the measurement of elastic and photoelastic constants," *Phys. Rev. B*, vol. 6, no. 2, pp. 639–673, 1972.

[24] J. Smith *et al.*, "Simultaneous distributed strain and temperature measurement," *Appl. Opt.*, vol. 38, no. 25, pp. 5372–5377, 1999.

[25] G. B. Benedek, J. B. Lastovska, K. Fritsch, and T. Greytak, "Brillouin scattering in liquids and solids using low-power lasers," *J. Opt. Soc. Am.*, vol. 54, pp. 1284–1285, Oct 1964.

[26] S. A. Lee *et al.*, "Elastic and photoelastic anisotropy of solid hf at high pressure," *Phys. Rev. B*, vol. 34, no. 4, pp. 2799–2806, 1986.

[27] S. K. Satija and C. Wang, "Brillouin scattering study of elastic anomaly in (KCN) x (KBr) 1-x system," *Solid State Communications*, vol. 28, no. 8, pp. 617 – 619, 1978.

[28] S. Itoh, T. Yamana, and S. Kojima, "Quick measurement of Brillouin spectra of glass-forming material trimethylene glycol by angular dispersion-type Fabry-Pérot interferometer system," *Jpn. J. Appl. Phys.*, vol. 35, no. 5b, pp. 2879–2881, 1996.

[29] H. D. Hochheimer, "High-pressure Brillouin scattering study of the order-disorder transition in KCN," *Phys. Rev. Lett.*, vol. 38, no. 15, pp. 832–835, 1977.

[30] L. Letamendia, M. Belkadi, O. Eloutassi, J. Rouch, D. Risso, P. Cordero, and A. Z. Patashinski, "Temperature anomalies of hypersound velocity and specific heat ratio in liquid quinoline," *Physica A: Statistical Mechanics and its Applications*, vol. 354, pp. 34 – 48, 2005.

[31] K. J. Koski, P. Akhenblit, K. McKiernan, and J. L. Yarger, "Non-invasive determination of the complete elastic moduli of spider silks," *Nat Mater*, vol. 12, 2013.

[32] E. F. Gramsbergen, "Interfacial hydrodynamic modes at a solid-liquid interface by light scattering," *Phys. Rev. A*, vol. 40, no. 9, pp. 5437–5439, 1989.

[33] T. Kitazawa, K. Yamashita, and S. Kinoshita, "Near-field Brillouin scattering spectroscopy under coexistence of acoustic and central mode," *Chemical Physics Letters*, vol. 448, no. 4–6, pp. 189 – 193, 2007.

[34] T. Kitazawa and S. Kinoshita, "Near-field Brillouin scattering as a probe of low-frequency dynamics at an interface," *Chemical Physics Letters*, vol. 386, no. 1–3, pp. 179 – 183, 2004.

[35] J. K. Kruger, "A new Brillouin scattering technique for the investigation of acoustic and opto-acoustic properties: application to polymers," *J. Phys.*, vol. 31, pp. 1913–1917, 1998.

[36] J. K. Kruger, "Hypersonic properties of nematic and smectic polymer liquid crystals," *Phys. Rev. A*, vol. 37, no. 7, pp. 2637–2643, 1988.

[37] R. Vacher, M. Delsanti, J. Pelous, L. Cecchi, A. Winter, and J. Zarzycki, "A Brillouin scattering study of glasses of various fictive temperatures," *Journal of Materials Science*, vol. 9, pp. 829–834, 1974.

[38] R. Vialla *et al.*, "Eliminating the broadening by finite aperture in Brillouin spectroscopy," *Rev. of Sc. Instr.*, vol. 82, pp. 113110–1, 2011.

[39] J. M. Vaughan, *The Fabry-Pérot interferometer: history, theory, practice, and applications*. Taylor and Francis, 1989.

[40] J. R. Sandercock, "Simple stabilization scheme for maintenance of mirror alignment in a scanning Fabry-Pérot interferometer," *Journal of Physics E: Scientific Instruments*, vol. 9, no. 7, p. 566, 1976.

[41] J. R. Sandercock, "Some recent developments in Brillouin-Scattering," *RCA Rev.*, vol. 36, no. 1, pp. 89–107, 1975.

[42] D. Waltson *et al.*, "The use of area detectors in Brillouin spectroscopy," *Rev. Sci. Instrum.*, vol. 67, no. 8, 1996.

[43] K. J. Koski, "High pressure angle-dispersive Brillouin spectroscopy: A technique for determining acoustic velocities and attenuations in liquids and solids," *Rev. Sci. Instrum.*, vol. 73, 2002.

[44] S. T. Y. Ike and S. Kojima, "High-resolution Brillouin spectroscopy with angular dispersion-type Fabry-Pérot interferometer and its application to a quartz crystal," *Rev. Sci. Instrum.*, vol. 78, no. 7, 2007.

[45] S. Itoh, "Very rapid nonscanning Brillouin spectroscopy using fixed etalons and multichannel detectors," *Jpn. J. Appl. Phys.*, vol. 37, pp. 3134–3135, 1998.

[46] S. Itoh *et al.*, "Brillouin scattering study of glass-forming liquid with simple structure using angular dispersion Fabry-Pérot interferometer," *Progress of theoretical physics*, vol. 126, pp. 253–256, 1997.

[47] K. J. Konski and J. L. Yarger, "Brillouin imaging," *Applied Physics Letter*, vol. 87, 2005.

[48] M. Shirasaki, "Virtually imaged phased array," *Fujitsu Scientific and Technical Journal*, vol. 35, no. 1, p. 113, 1999.

[49] A. M. W. A. Vega and C. Lin, "Generalized grating equation for virtually-imaged phased-array spectral dispersers," *Applied Optics*, 2003.

[50] S. Xiao, "A dispersion law for virtually imaged phased-array spectral dispersers based on paraxial wave theory," *IEEE J. of Quant. Electr.*, vol. 40, no. 4, pp. 420–426, 2004.

[51] G. Scarcelli and S. H. Yun, "Multistage VIPA etalons for high-extinction parallel Brillouin spectroscopy," *Opt. Express*, vol. 19, pp. 10913–10922, May 2011.

[52] G. Scarcelli and S. H. Yun, "Confocal Brillouin microscopy for three-dimensional mechanical imaging," *Nat Photon*, vol. 2, pp. 39–43, 2008.

[53] T. D. Wang, "Dual-axis confocal microscope for high-resolution in vivo imaging," *Optics Letters*, vol. 28, no. 6, pp. 414–416, 2003.

[54] G. Scarcelli, P. Kim, and S. H. Yun, "In vivo measurement of age-related stiffening in the crystalline lens by Brillouin optical microscopy," *Biophysical Journal*, vol. 101, no. 6, pp. 1539 – 1545, 2011.

[55] G. Scarcelli *et al.*, "Brillouin optical microscopy for corneal biomechanics," *IOVS*, vol. 53, pp. 185–190, 2012.

[56] S. C. Mahar, *Spontaneous Brillouin Scattering Quech Diagnostics for Large Superconductiong Magnets*. PhD thesis, Massachusetts Institute of Technology, 2008.

[57] L. D. Landau, *Electrodynamics of continuous media*. Pergamon Press, 1984.

[58] C. Doppler, "Ueber das farbige licht der doppelsterne und einiger anderer gestirne des himmels," *Abh Kgl Böhm Ges Wissensch*, pp. 465–482, 1842.

[59] R. Y. Chiao *et al.*, "Stimulated Brillouin scattering and coherent generation of intense hypersonic waves," *Phys. Rev. Lett.*, vol. 12, no. 21, pp. 592–595, 1964.

[60] W. Kaiser and M. Maier, *Stimulated Rayleigh, Brillouin and Raman spectroscopy*. Laser Hanbook, 1972.

[61] R. G. Smith, "Optical power handling capacity of low loss optical fibers as determined by stimulated Raman and Brillouin scattering," *Appl. Opt.*, vol. 11, pp. 2489–2494, Nov 1972.

[62] A. Yeniay, J.-M. Delavaux, and J. Toulouse, "Spontaneous and stimulated Brillouin scattering gain spectra in optical fibers," *J. Lightwave Technol.*, vol. 20, p. 1425, Aug 2002.

[63] J. D. Marconi, "Double-pumped parametric amplifier with strained fibre to suppress sbs," *Electr. Lett.*, vol. 40, no. 24, 2004.

[64] E. M. Purcell, *Electricity and Magnetism*. New York: McGraw-Hill, 1985.

[65] M. Born and E. Wolf, *Principles of Optics: Electromagnetic Theory of Propagation, Interference and Diffraction of Light*. Oxford: Pergamon Press, 1980.

[66] J. Stratton, *Electromagnetic theory*. IEEE Press series on electromagnetic wave theory, John Wiley & Sons, Inc., 2007.

[67] B. Chu, *Laser Light Scattering*. Academic Press, 1991.

[68] http://www.antenna-theory.com/basics/radPattern.html.

[69] C. Raman, "A new radiation," *Indian Journal of Physics*, vol. 2, pp. 387–398, 1928.

[70] R. McCreery, *Raman Spectroscopy for Chemical Analysis*. John Wiley and Sons, 2005.

[71] M. Damzen, *Stimulated Brillouin scattering: fundamentals and applications*. Series in optics and optoelectronics, Great Britain: Institute of Physics Pub., 2003.

[72] R. Shuker and R. W. Gammon, "Raman-scattering selection-rule breaking and the density of states in amorphous materials," *Phys. Rev. Lett.*, vol. 25, pp. 222–225, Jul 1970.

[73] Z. Huang, A. McWilliams, H. Lui, D. I. McLean, S. Lam, and H. Zeng, "Near-infrared Raman spectroscopy for optical diagnosis of lung cancer," *International Journal of Cancer*, vol. 107, no. 6, pp. 1047–1052, 2003.

[74] G. B. Benedek and K. Fritsch, "Brillouin scattering in cubic crystals," *Phys. Rev.*, vol. 149, no. 2, pp. 647–662, 1966.

[75] R. H. Dicke, "The effect of collisions upon the doppler width of spectral lines," *Phys. Rev.*, vol. 89, no. 2, pp. 472–473, 1953.

[76] D. C. Liptak, J. C. Reber, J. F. Maguire, and M. S. Amer, "On the development of a confocal Rayleigh-Brillouin microscope," *Review of Scientific Instruments*, vol. 78, no. 1, 2007.

[77] S. Caponi *et al.*, "Electro-optic modulator for high resolution Brillouin scattering measurements," *Rev. Sci. Instrum.*, vol. 72, no. 198, 2001.

[78] R. D. Mountain, "Thermal relaxation and Brillouin scattering in liquids," *J. Chem. Phys.*, vol. 44, no. 2785, 1966.

[79] C. J. Montrose, V. A. Solovyev, and T. A. Litovitz, "Brillouin scattering and relaxation in liquids," *J. Acoust. Soc. Am.*, vol. 43, no. 117, 1968.

[80] S. M. Rytov, "Diffraction of light by ultrasonic waves," *Izv. Akad. Nauk SSSR*, vol. 223, 1937.

[81] A. Einstein *Ann. Physik*, vol. 33, p. 1275, 1910.

[82] Smoluchowski *Ann. Physik*, vol. 25, p. 205, 1908.

[83] C. L. O'Connor and J. P. Schlupf, "Brillouin scattering in water: The Landau—Placzek ratio," *J. Chem. Phys.*, vol. 47, p. 31, 1967.

[84] H. Z. Cummins and R. W. Gammon, "Rayleigh and Brillouin scattering in liquids: The Landau—Placzek ratio," *J. Chem. Phys.*, vol. 44, no. 2785, 1966.

[85] R. Wehner and R. Klein, "Scattering of light by entropy fluctuations in dielectric crystals," *Physica*, vol. 62, no. 2, pp. 161 – 197, 1972.

[86] M. D. Ricard, *Biomechanics of human movement.* University of Texas at Arlington, 2012.

[87] D. R. Askeland and P. Phule, *The Science and Engeneering of materials.* Bill Stenquist, 2003.

[88] J. M. Vaughan and J. T. Randall, "Brillouin scattering, density and elastic properties of the lens and cornea of the eye," *Nature*, vol. 284, no. 5755, pp. 489–491, 1980.

[89] C. Kittel, *Introduction to Solid State Physics.* John Wiley & Sons, 2005.

[90] S. Alexander, P. M. Chaikin, P. Grant, G. J. Morales, P. Pincus, and D. Hone, "Charge renormalization, osmotic pressure, and bulk modulus of colloidal crystals: Theory," *The Journal of Chemical Physics*, vol. 80, no. 11, pp. 5776–5781, 1984.

[91] R. C. Hibbeler, *Statics and mechanics of materials.* Prentice Hall, 2004.

[92] P. Benassi, R. Eramo, A. Giugni, M. Nardone, and M. Sampoli, "A spectrometer for high-resolution and high-contrast Brillouin spectroscopy in the ultraviolet," *Review of Scientific Instruments*, vol. 76, no. 1, 2005.

[93] V. Mazzacurati, P. Benassi, and G. Ruocco, "A new class of multiple dispersion grating spectrometers," *Journal of Physics E: Scientific Instruments*, vol. 21, no. 8, p. 798, 1988.

[94] V. Mazzacurati and G. Ruocco, "The super-gratings: How to improve the limiting resolution of grating spectrometers," *Optics Communications*, vol. 76, no. 3–4, pp. 185 – 190, 1990.

[95] H. Tanaka and T. Sonehara, "New method of superheterodyne light beating spectroscopy for Brillouin scattering using frequency-tunable lasers," *Phys. Rev. Lett.*, vol. 74, pp. 1609–1612, Feb 1995.

[96] G. Simonsohn and F. Wagner, "High-resolution Rayleigh–Brillouin correlation spectroscopy," *Opt. Lett.*, vol. 14, pp. 110–112, Jan 1989.

[97] K. Shimizu, T. Horiguchi, Y. Koyamada, and T. Kurashima, "Coherent self-heterodyne detection of spontaneously Brillouin-scattered light waves in a single-mode fiber," *Opt. Lett.*, vol. 18, pp. 185–187, Feb 1993.

[98] G. Hernandez, *Fabry-Pérot Interferometers*. Cambridge University Press, 1986.

[99] O. Svelto, *Principles of Lasers*. Springer Science, 2010.

[100] W. G. Fastie, "A small plane grating monochromator," *J. Opt. Soc. Am.*, vol. 42, pp. 641–647, Sep 1952.

[101] J.-H. Ko and S. Kojima, "Angular dispersion-type nonscanning Fabry-Pérot interferometer applied to ethanol-water mixture," *J. Opt. Soc. Korea*, vol. 13, pp. 261–266, Jun 2009.

[102] J. Ko and S. Kojima, "Nonscanning Brillouin spectroscopy applied to solid materials," *Review of Scientific Instruments*, vol. 73, no. 12, pp. 4390–4392, 2002.

[103] G. Lepert, *Integrated optics for coupled-cavity quantum electrodynamics*. PhD thesis, Imperial College London, 2013.

[104] A. E. Siegman, *Lasers*. University Science Books, 1990.

[105] S. Hooker and C. Webb, *Laser Physics*. Oxford, 2010.

[106] S. A. Diddams, L. Hollberg, and V. Mbele, "Molecular fingerprinting with the resolved modes of a femtosecond laser frequency comb," *Nature*, vol. 445, no. 7128, pp. 627–630, 2007.

[107] S. Itoh, Y. Yamazaki, K. Katoh, and J. Chen, "High precision testing method for Fabry-Pérot etalon," *Optical Review*, vol. 8, pp. 179–183, 2001.

[108] B. E. Saleh, *Fundamental of Photonics*. New York: Wiley-Interscience, 1991.

[109] G. Scarcelli, P. Kim, and S. H. Yun, "Cross-axis cascading of spectral dispersion," *Opt. Lett.*, vol. 33, pp. 2979–2981, Dec 2008.

[110] M. Monici, "Cell and tissue autofluorescence research and diagnostic applications," vol. 11 of *Biotechnology Annual Review*, pp. 227 – 256, Elsevier, 2005.

[111] E. G. Codding and G. Horlick, "Apodization and phase information in fourier transform spectroscopy," *Appl. Spectrosc.*, vol. 27, pp. 85–92, Mar 1973.

[112] S. Yun and G. Scarcelli, "Methods, arrangements and systems for obtaining information associated with a sample using optical microscopy," Feb. 14 2012. US Patent 8,115,919.

[113] S. H. Yun and G. Scarcelli, *Method and arrangement for obtaining information and providing analysis for biological tissues.* US Patent Application Publication, April 2012.

[114] K. Schorstein, A. Popescu, G. Scheich, T. Walther, and E. S. Fry, *Towards a Brillouin-LIDAR for remote sensing of the temperature profile in the ocean.* OCEANS 2006, Sept 2006.

[115] A. Popescu, K. Schorstein, and T. Walther, "A novel approach to a Brillouin–LIDAR for remote sensing of the ocean temperature," *Applied Physics B*, vol. 79, no. 8, pp. 955–961, 2004.

[116] M. G. K. Schorstein, A.Popescu and T. Walther, "Remote water temperature measurements based on Brillouin scattering with a frequency doubled pulsed Yb:doped fiber amplifier," *Sensors*, vol. 8, no. 9, 2008.

[117] A. Rudolf and T. Walther, "Laboratory demonstration of a Brillouin lidar to remotely measure temperature profiles of the ocean," *Optical Engineering*, vol. 53, no. 5, p. 051407, 2014.

[118] Z. Meng, A. J. Traverso, and V. V. Yakovlev, "Background clean-up in Brillouin microspectroscopy of scattering medium," *Opt. Express*, vol. 22, pp. 5410–5415, Mar 2014.

[119] L. C. G. E. Devlin, J. L. Davis and S. Geschwind, "Absorption of unshifted scattered light by a molecular I2 filter in Brillouin and Raman scattering," *Applied Physics Letter*, vol. 19, no. 138, 1971.

[120] M. Nikles, L. Thevenaz, and P. Robert, "Brillouin gain spectrum characterization in single-mode optical fibers," *Journal of Lightwave Technology*, vol. 15, no. 10, 1997.

[121] C. W. Hoyt, M. Sheik-Bahae, R. I. Epstein, B. C. Edwards, and J. E. Anderson, "Observation of anti-Stokes fluorescence cooling in thulium-doped glass," *Phys. Rev. Lett.*, vol. 85, pp. 3600–3603, Oct 2000.

[122] A. Jaboski, "Efficiency of Anti-Stokes fluorescence in dyes," *Nature*, vol. 131, pp. 839–840, 1933.

[123] G. Indebetouw, "Nondiffracting optical fields: some remarks on their analysis and synthesis," *J. Opt. Soc. Am. A*, vol. 6, pp. 150–152, Jan 1989.

[124] J. Durnin, J. J. Miceli, and J. H. Eberly, "Diffraction-free beams," *Phys. Rev. Lett.*, vol. 58, no. 15, pp. 1499–1501, 1987.

[125] J. F. Maguire, J. C. F. Michielsen, and G. Rakhorst, "Brillouin light scattering from binary liquid mixtures," *The Journal of Physical Chemistry*, vol. 85, no. 20, pp. 2971–2975, 1981.

[126] E. Rat, M. Foret, G. Massiera, R. Vialla, M. Arai, R. Vacher, and E. Courtens, "Anharmonic versus relaxational sound damping in glasses. Brillouin scattering from densified silica," *Phys. Rev. B*, vol. 72, no. 21, p. 214204, 2005.

[127] D. Heiman, D. S. Hamilton, and R. W. Hellwarth, "Brillouin scattering measurements on optical glasses," *Phys. Rev. B*, vol. 19, pp. 6583–6592, Jun 1979.

[128] I. Kilicaslan and C. Esen, "An experimental study of the angle and temperature dependences of the spontaneous Brillouin shift in ethanol," *Journal of Modern Optics*, vol. 52, no. 8, pp. 1189–1196, 2005.

[129] S. I. J. Ko, Z. Chao and S. Kojima, "Brillouin measurement of glass-forming ethanol using an angular dispersion-type Fabry-Pérot interferometer," *Jpn. J. Appl. Phys.*, vol. 40, pp. 3575–3578, 2001.

[130] J. H. W. Leidecker and J. T. LaMacchia, "Instrumental effects on Brillouin line shapes," *The Journal of the Acoustical Society of America*, vol. 43, no. 1, pp. 143–151, 1968.

[131] R. Lang and K. Kobayashi, "External optical feedback effects on semiconductor injection laser properties," *Quantum Electronics, IEEE Journal of*, vol. 16, no. 3, pp. 347–355, 1980.

[132] E. R. S. D. H. Rank and D. W. E. Axford, "Hypersonic velocity in acetone at low temperatures," *Nature*, vol. 164, pp. 67–68, 1949.

[133] M. S. Amer, M. Bennett, and J. F. Maguire, "A Brillouin scattering study of C 60/toluene mixtures," *Chemical Physics Letters*, vol. 457, no. 4–6, pp. 329 – 331, 2008.

[134] W. F. Oliver, C. A. Herbst, S. M. Lindsay, and G. H. Wolf, "A general method for determination of Brillouin linewidths by correction for instrumental effects and aperture broadening: Application to high-pressure diamond anvil cell experiments," *Review of Scientific Instruments*, vol. 63, no. 3, pp. 1884–1895, 1992.

[135] M. G. Beghi, F. Di Fonzo, S. Pietralunga, C. Ubaldi, and C. E. Bottani, "Precision and accuracy in film stiffness measurement by Brillouin spectroscopy," *Review of Scientific Instruments*, vol. 82, no. 5, 2011.

[136] A. G. E. M. G. Beghi and P. V. Zinin, *Ultrasonic nondestructive evaluation: engineering and biological material characterization*. CRC Press, Boca Raton, 2004.

[137] H. G. Danielmeyer, "Aperture corrections for sound-absorption measurements with light scattering," *The Journal of the Acoustical Society of America*, vol. 47, no. 1B, pp. 151–154, 1970.

[138] C. Gigault and J. R. Dutcher, "Analysis of a simple method for the reduction of phonon peak broadening in surface Brillouin light scattering," *Appl. Opt.*, vol. 37, pp. 3318–3323, May 1998.

[139] M. R. Foreman and P. Török, "Computational methods in vectorial imaging," *Journal of Modern Optics*, vol. 58, no. 5-6, pp. 339–364, 2011.

[140] Z. Ding, H. Ren, Y. Zhao, J. S. Nelson, and Z. Chen, "High-resolution optical coherence tomography over a large depth range with an axicon lens," *Opt. Lett.*, vol. 27, pp. 243–245, Feb 2002.

[141] M. Lei and B. Yao, "Multifunctional darkfield microscopy using an axicon," *Journal of Biomedical Optics*, vol. 13, no. 4, 2008.

[142] S. Fürhapter, A. Jesacher, S. Bernet, and M. Ritsch-Marte, "Spiral phase contrast imaging in microscopy," *Opt. Express*, vol. 13, pp. 689–694, Feb 2005.

[143] A. Jesacher, S. Fürhapter, S. Bernet, and M. Ritsch-Marte, "Shadow effects in spiral phase contrast microscopy," *Phys. Rev. Lett.*, vol. 94, p. 233902, Jun 2005.

[144] D. Mawet, P. Riaud, O. Absil, and J. Surdej, "Annular groove phase mask coronagraph," *The Astrophysical Journal*, vol. 633, no. 2, p. 1191, 2005.

[145] J. H. Mcleod, "The axicon: A new type of optical element," *J. Opt. Soc. Am.*, vol. 44, pp. 592–592, Aug 1954.

[146] M. A. Lauterbach, M. Guillon, A. Soltani, and V. Emiliani, "STED microscope with spiral phase contrast," *Sci. Rep.*, vol. 3, 06 2013.

[147] P. Nellist and S. Pennycook, "The principles and interpretation of annular dark-field z-contrast imaging," *Advances in Imaging and Electron Physics*, vol. 113, no. 147-203, 2000.

[148] I. Braslavsky, R. Amit, B. M. J. Ali, O. Gileadi, A. Oppenheim, and J. Stavans, "Objective-type dark-field illumination for scattering from microbeads," *Appl. Opt.*, vol. 40, pp. 5650–5657, Nov 2001.

[149] E. H. Stelzer and S. Lindek, "Fundamental reduction of the observation volume in far-field light microscopy by detection orthogonal to the illumination axis: confocal theta microscopy," *Optics Communications*, vol. 111, no. 5–6, pp. 536 – 547, 1994.

[150] D. Axelrod, T. Burghardt, and N. Thompson, "Total internal reflection fluorescence," *Ann. Rev. Biophys. Bioeng*, vol. 13, no. 247-68, 1984.

[151] T. Ruckstuhl and S. Seeger, "Confocal total-internal-reflection fluorescence microscopy with a high-aperture parabolic mirror lens," *Appl. Opt.*, vol. 42, pp. 3277–3283, Jun 2003.

[152] D. Axelrod, "Cell-substrate contacts illuminated by total internal reflection fluorescence," *Journal of Cell Biology*, vol. 89, no. 1, pp. 141–145, 1981.

[153] D. Axelrod, "Total internal reflection fluorescence microscopy in cell biology," *Traffic*, vol. 2, no. 11, pp. 764–774, 2001.

[154] H. Shroff, C. G. Galbraith, J. A. Galbraith, and E. Betzig, "Live-cell photoactivated localization microscopy of nanoscale adhesion dynamics," *Nat Meth*, vol. 5, pp. 417–423, 05 2008.

[155] M. J. Rust, M. Bates, and X. Zhuang, "Sub-diffraction-limit imaging by stochastic optical reconstruction microscopy (STORM)," *Nat Meth*, vol. 3, pp. 793–796, 10 2006.

[156] W. T. Welford, "Use of annular apertures to increase focal depth," *J. Opt. Soc. Am.*, vol. 50, pp. 749–752, Aug 1960.

[157] C. J. R. Sheppard, "High-aperture beams," *J. Opt. Soc. Am. A*, vol. 18, pp. 1579–1587, Jul 2001.

[158] M. Minsky, *Confocal scanning microscope*. Rapport technique, 1955.

[159] T. Wilson and C. Sheppard, "Theory and practice of scanning optical microscopy," *Academic Press*, 1984.

[160] P. Török, *An imaging theory for advanced, high numerical aperture optical microscope*. Hungary: DSc thesis, 2004.

[161] C. Romero, *High numerical aperture Mueller matrix polarimetry and applications to multiplexed optical data storage*. PhD thesis, Imperial College London, 2011.

[162] J. Beuthan, O. Minet, J. Helfmann, M. Herrig, and G. Muller, "The spatial variation of the refractive index in biological cells," *Physics in medicine and biology*, vol. 41, no. 3, p. 369, 1996.

[163] J. M. Schmitt and G. Kumar, "Turbulent nature of refractive-index variations in biological tissue," *Opt. Lett.*, vol. 21, pp. 1310–1312, Aug 1996.

[164] T. G. G. Benedek, "Brillouin scattering in liquids," *Proceeding in the IEEE*, vol. 53, no. 10, pp. 1623–1629, 1965.

[165] S. A. Battista, Z. Lu, S. Hofmann, T. Freddo, D. R. Overby, and H. Gong, "Reduction of the available area for aqueous humor outflow and increase in meshwork herniations into collector channels following acute iop elevation in bovine eyes," *Investigative Ophthalmology and Visual Science*, vol. 49, no. 12, pp. 5346–5352, 2008.

[166] R. Vargas-Pinto, H. Gong, A. Vahabikashi, and M. Johnson, "The effect of the endothelial cell cortex on atomic force microscopy measurements," *Biophysical Journal*, vol. 105, no. 2, pp. 300–309, 2014.

[167] G. Bao and S. Suresh, "Cell and molecular mechanics of biological materials," *Nat Mater*, vol. 2, pp. 715–725, 11 2003.

[168] X. J. Liang, A. Q. Liu, C. S. Lim, T. C. Ayi, and P. H. Yap, "Determining refractive index of single living cell using an integrated microchip," *Sensors and Actuators A: Physical*, vol. 133, pp. 349–354, 2 2007.

[169] N. Lue, G. Popescu, T. Ikeda, R. R. Dasari, K. Badizadegan, and M. S. Feld, "Live cell refractometry using microfluidic devices," *Opt. Lett.*, vol. 31, pp. 2759–2761, Sep 2006.

[170] Y. Zhou, Z. He, and S. Sato, "A novel method for determining the cell thickness and twist angle of a twisted nematic cell by Stokes parameter measurement," *Japanese Journal of Applied Physics*, vol. 36, no. 5R, p. 2760, 1997.

[171] D. Bettega P. Calzolari S. M. Doglia B. Dulio L. Tallone A. M. Villa, "Technical report: Cell thickness measurements by confocal fluorescence microscopy

on c3h10t1/2 and v79 cells," *International Journal of Radiation Biology*, vol. 74, no. 3, pp. 397–403, 1998.

[172] M. Durante, G. Gialanella, G. Grossi, and M. Pugliese, "Thickness measurements on living cell monolayers by nuclear methods," *Nuclear Instruments and Methods in Physics Research Section B: Beam Interactions with Materials and Atoms*, vol. 73, no. 4, pp. 543 – 549, 1993.

[173] P. Török, S. J. Hewlett, and P. Varga, "The role of specimen-induced spherical aberration in confocal microscopy," *Journal of Microscopy*, vol. 188, no. 2, pp. 158–172, 1997.

[174] C. R. Burch and J. P. P. Stock, "Phase-contrast microscopy," *Journal of Scientific Instruments*, vol. 19, no. 5, p. 71, 1942.

[175] Y. M. Lam, L. Trinckle-Mulcahy, and A. I. Lamond, "The nucleolus," *Journal of Cell Science*, vol. 118, no. 7, pp. 1335–1339, 2005.

[176] Staff, *Blausen gallery 2014*. Wikiversity Journal of Medicine.

[177] A. J. Lusis, "Atherosclerosis," *Nature*, vol. 407, pp. 233–241, 09 2000.

[178] X. Castellon and V. Bogdanova, "Screening for subclinical atherosclerosis by noninvasive methods in asymptomatic patients with risk factors," *Clinical Interventions in Aging*, vol. 8, pp. 573–580, 2013.

[179] K. Tanaka and A. Katouzian, "Atherosclerotic plaque characterization from radio frequency ultrasound signal processing," *US Cardiology*, vol. 4, no. 1, pp. 54–56, 2007.

[180] C. L. de Korte, A. F. W. van der Steen, E. I. Céspedes, G. Pasterkamp, S. G. Carlier, F. Mastik, A. H. Schoneveld, P. W. Serruys, and N. Bom, "Characterization of plaque components and vulnerability with intravascular ultrasound elastography," *Physics in Medicine and Biology*, vol. 45, no. 6, p. 1465, 2000.

[181] I. Wilkinson, J. Cockcroft, and D. Webb, "Pulse wave analysis and arterial stiffness," *Journal of cardiovascular pharmacology*, vol. 32, pp. S33—7, 1998.

[182] J. J. Oliver and D. J. Webb, "Noninvasive assessment of arterial stiffness and risk of atherosclerotic events," *Arteriosclerosis, Thrombosis, and Vascular Biology*, vol. 23, no. 4, pp. 554–566, 2003.

[183] I. S. Mackenzie, I. B. Wilkinson, and J. R. Cockcroft, "Assessment of arterial stiffness in clinical practice," *QJM*, vol. 95, pp. 67–74, 02 2002.

[184] D. Huang, E. Swanson, C. Lin, J. Schuman, W. Stinson, W. Chang, M. Hee, T. Flotte, K. Gregory, and C. Puliafito, "Optical coherence tomography," *Science*, vol. 254, no. 5035, pp. 1178–1181, 1991.

[185] L. Liu, J. A. Gardecki, S. K. Nadkarni, J. D. Toussaint, Y. Yagi, B. E. Bouma, and G. J. Tearney, "Imaging the subcellular structure of human coronary atherosclerosis using micro-optical coherence tomography," *Nat Med*, vol. 17, pp. 1010–1014, 08 2011.

[186] D. Zhu, K. V. Larin, Q. Luo, and V. V. Tuchin, "Recent progress in tissue optical clearing," *Laser and Photonics Reviews*, vol. 7, no. 5, pp. 732–757, 2013.

[187] V. V. Tuchin, "Optical clearing of tissues and blood using the immersion method," *Journal of Physics D: Applied Physics*, vol. 38, no. 15, p. 2497, 2005.

[188] V. Tuchin, "Tissue optics," *Light Scattering Methods and Instrumentation for Medical Diagnosis, SPIE Tutorial Texts in Optical Engineering, TT38*, 2000.

[189] A. N. Bashkatov, E. A. Genina, V. I. Kochubey, and V. V. Tuchin, "Optical properties of human skin, subcutaneous and mucous tissues in the wavelength range from 400 to 2000 nm," *Journal of Physics D: Applied Physics*, vol. 38, no. 15, p. 2543, 2005.

[190] J. B. Segur and H. E. Oberstar, "Viscosity of glycerol and its aqueous solutions," *Industrial & Engineering Chemistry*, vol. 43, no. 9, pp. 2117–2120, 1951.

[191] R. Ross, "Atherosclerosis - an inflammatory disease," *New England Journal of Medicine*, vol. 340, pp. 115–126, 2014/10/28 1999.

[192] M. J. Mulvany and C. Aalkjaer, "Structure and function of small arteries," *Physiological Reviews*, vol. 70, pp. 921–961, 10 1990.

[193] B. Corden, N. G. Keenan, A. S. M. de Marvao, T. J. W. Dawes, A. DeCesare, T. Diamond, G. Durighel, A. D. Hughes, S. A. Cook, and D. P. O'Regan, "Body fat is associated with reduced aortic stiffness until middle age," *Hypertension*, vol. 61, pp. 1322–1327, 06 2013.

[194] C. Cheng, D. Tempel, R. van Haperen, A. van der Baan, F. Grosveld, M. J. A. P. Daemen, R. Krams, and R. de Crom, "Atherosclerotic lesion size and vulnerability are determined by patterns of fluid shear stress," *Circulation*, vol. 113, pp. 2744–2753, 06 2006.

[195] R. Krams, C. Cheng, F. Helderman, S. Verheye, L. C. A. van Damme, B. Mousavi Gourabi, D. Tempel, D. Segers, P. de Feyter, G. Pasterkamp, D. De Klein, R. de Crom, A. F. W. van der Steen, and P. Serruys, "Shear stress is associated with markers of plaque vulnerability and mmp-9 activity," *EuroIntervention : journal of EuroPCR in collaboration with the Working Group on Interventional Cardiology of the European Society of Cardiology*, vol. 2, pp. 250—256, August 2006.

[196] A. Mehlem, C. E. Hagberg, L. Muhl, U. Eriksson, and A. Falkevall, "Imaging of neutral lipids by oil red o for analyzing the metabolic status in health and disease," *Nat. Protocols*, vol. 8, pp. 1149–1154, 06 2013.